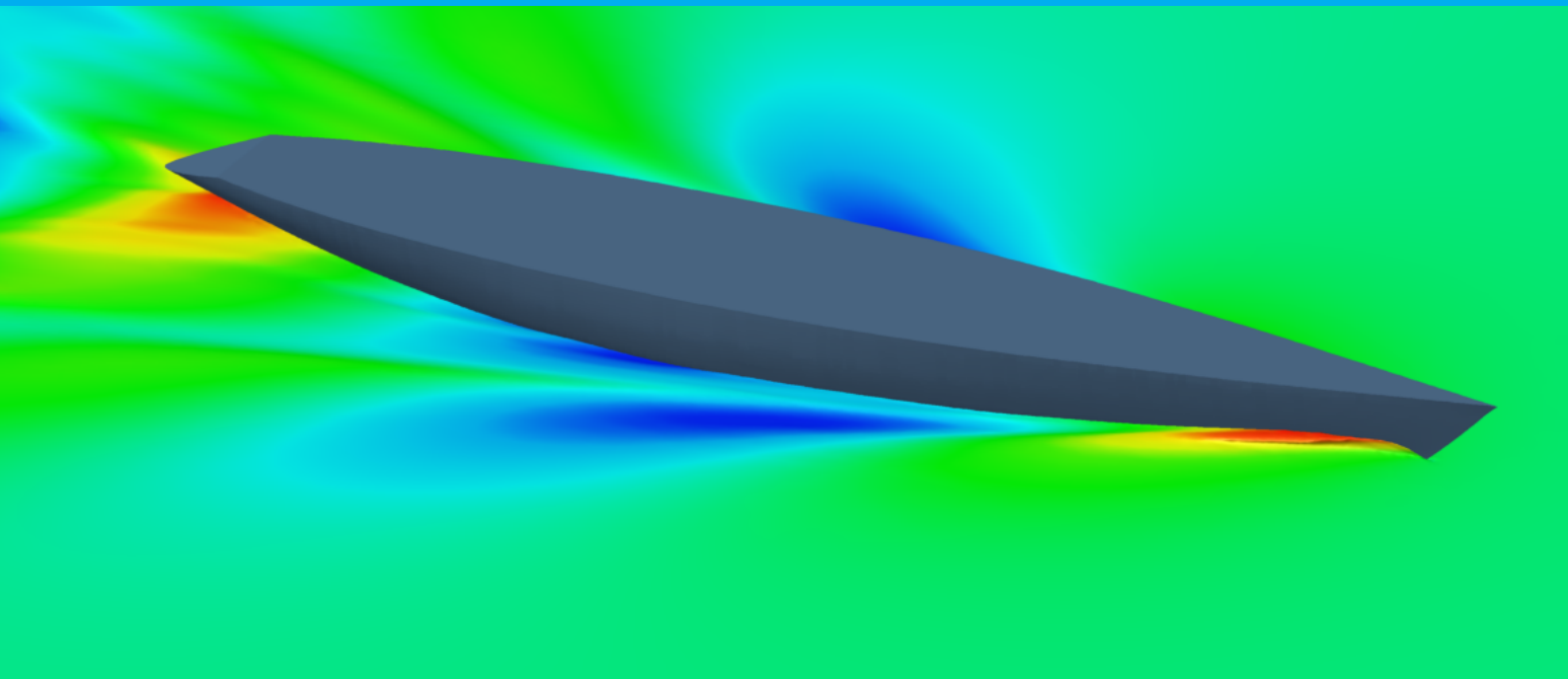


Keel-Rudder Interaction

A look into the wake of a sailing yacht

R.J. Boonstra



Keel-Rudder Interaction

by

R.J. Boonstra

to obtain the degree of Master of Science
at the Delft University of Technology,
to be defended publicly on Monday January 28, 2019 at 14:00.

Student number:	4245903
Project duration:	November 2017 – January 2019
Thesis committee:	Prof. dr. ir. A. van 't Veer, TU Delft, supervisor
	Dr. Ir. J. A. Keuning, TU Delft, supervisor
	Dr. Ir. I. Akkerman, TU Delft, Committee member
	Dr. A. A. Kana, TU Delft, Committee member

An electronic version of this thesis is available at <http://repository.tudelft.nl/>.

Preface

Being able to perform a research project on a sailing yacht is seeing a dream come true. Fortunately Dr. Keuning had a couple of interesting subjects to graduate on. From which keel-rudder interaction seemed the most interesting to me, because it combines towing tank tests with a state of the art research method (CFD simulations) to research the wake of a sailing yacht.

For the reader who is interested in the background on the project I refer to chapter 2: Background. For more information on the CFD simulations see chapter 3: Numerical experiments. The towing tank experiments are discussed and presented in chapter 4: Towing tank experiments. As an addition to the comparison and the analysis of the experiments in chapter 6: Analysis of the results; describes chapter 5: Uncertainty assessment, the uncertainty assessment of both experiments, for the CFD simulations this is a grid convergence study. The conclusions are presented in chapter 7: Conclusions and recommendations.

I would like to thank Dr. Keuning and Prof. Van 't Veer for making this project possible. Also I would like to thank the employees of the towing tank, in special: Wick, Nico, Jennifer, Jasper and Raghu, and NUMECA for all their support, without them it would not have been possible. Finally, I would like to thank the support of my family and friends.

*R.J. Boonstra
Delft, January 2019*

Abstract

In the early '00 of this century Keuning et al. [32] looked into the hydrodynamic forces on the rudder and the influence of the hull and keel on these forces. Among others, they have assessed the lift and drag forces on the rudder. One of the outcomes of this study was an asymmetric lift curve; for negative rudder angles the rudder seems to stall at angles more than five degrees smaller than for the positive rudder angles.

The goal for this research is to find and clarify the physical phenomenon which induces the rudder to stall at smaller rudder angles when subjected to a negative rudder angle (during bearing away). The main question to be answered in this report is: What physical phenomenon is at the basis of the asymmetric stalling behaviour on the rudder of a sailing yacht? Expected is that this phenomenon is caused by a flow interaction of the keel tip vortex on the low pressure side of the rudder.

Towing tank tests are used to validate the data from Keuning et al. [32]. After which CFD simulations are conducted to compare the towing tank tests to and to visualise the wake of the yacht in attempt to clarify the phenomena found.

The model used in these experiments consists of a hull and appendages. The hull is a parametric variation from a model based on the International America's Cup Rule made in 1992. The keel is the parent model of the Delft Systematic Keel Series and the rudder was designed for previous tests.

In the settings of the CFD simulations care is taken to ensure a good representation of the wake, where the vorticity is preserved, with the used of the 3rd order discretisation method ALVSMART. To ensure isotropy in the flow and a decent coupling between the boundary layer and the outer flow, the turbulence model EASM is used. A wall resolved boundary condition is used to capture the moment of flow separation on the rudder. Because of time considerations, the hull and keel have a wall-function boundary condition. The mesh is adapted according to the boundary conditions, with special attention for the region between the appendages. The other settings for the simulations are based on recommendations from NUMECA [46].

In the experiments the model is supported by a hexapod and the standard TU Delft 6-DOF measurement frame. The hexapod ensures a fixed desired position of the model during the tests. The sensors on the keel and rudder measure, respectively, in two and three directions. The forces of interest for these tests are: the lift and drag forces and the moment around x -axis for the rudder, the resistance and side force and the moment around z -axis for the model. The forces on the keel are for verification purposes.

As two experiments are compared an uncertainty assessment is conducted. For the solution verification and validation the grid convergence method developed by Eça & Hoekstra [11] is used. The ITTC [25] guidelines are used to determine the uncertainties of the experiments.

The grid required a specific approach for the refinement, as it is a hexedral unstructured grid. In the refinement the initial cell size is altered with a factor, this leads to an automatic change of the other refinement variables. Only two faces required extra refinement steps (free-surface and the gap of the rudder). The timestep is altered with the same factor as the initial cell size. The viscous layers have a different treatment and are changed to get the correct diffusion from the viscous first layer to the first layer of the euler mesh.

The convergence of the data was positive for all the cases. Both the forces on model and rudder are assessed, as well as different variables, the velocity, normalised vorticity, viscous stress and the λ_2 around the model. The uncertainty from the convergence of the forces is for some variables significant. In some cases this originated from a limitation of the method.

The validation of the forces showed in some cases some differences between the results of the towing tank experiments and the CFD simulations. These difference are probably originating from a difference in turbulence intensity or a suboptimal grid, although the latter is contradicted by the verification.

However, the results of the CFD simulations and the verification and validation study are suitable for this study. When the exact forces are more important than a visualisation of the wake, the grid should be optimised. The verification of the other variables than the forces showed good results.

A number of conclusions were found in this study. Firstly, the results of the towing tank experiments showed similarities to the previous experiments by Keuning et al. [32]. Differences are found in stall angles for positive rudder angles. These differences raise questions on the correctness of either of the experiments.

Secondly, no reasonable explanation is found for the negative drag forces found in the towing tank experiments. It is expected that these originate from the set-up of the rudder.

Thirdly, the lift curve found in the experiments is confirmed by the CFD data for the test cases. The physical effect behind the early stall behaviour of the rudder is still unknown. It is indicated that a part of the decrease in stall angle, a couple of degrees, is caused by the influence of the keel, when the disturbance passes on the low pressure side of the rudder. The hull is responsible for the remaining decrease. The CFD data indicates an influence of the vorticity of the keel and the boundary of the hull to cause a disturbance on the rudder.

The hypothesis stated is not confirmed in this study, but the CFD results show indications of the influence of the vorticity of the keel for positive rudder angles for a leeway angle of 3° .

A final remark about the use of CFD for these kinds of problems: CFD is a helpful tool for these kind of problems, however, it is also a difficult tool. False conclusions could be drawn if incorrect settings are used. In the future CFD will become a more and helpful tool, as computer power increases and CFD codes improve.

The main recommendation of this study is the following: a dry test should be conducted to check for crosstalk, to see the influence of moments on the measurements of the rudder. It is expected that this test will answer the uncertainties in the results of the lift and drag curves of the rudder.

Secondly, towing tank test with only the rudder should be conducted to find the undisturbed stall angle of the rudder.

Thirdly, the towing tank experiments should be recreated to determine the correctness of the results from this study and the results found by Keuning et al. [32].

Apart from these recommendations on the towing tank experiments, additional CFD simulations are required on the same set-up and possibly with different settings.

Contents

Preface	iii
Abstract	v
Nomenclature	viii
1 Introduction	1
2 Background	3
2.1 Previous research	3
2.2 Side force and yaw moment.	4
2.2.1 Extended keel method	4
2.2.2 Slender body theory	4
2.2.3 Interaction of wings	5
2.3 Vortex dynamics	6
2.3.1 Vortices from foils	7
3 Numerical experiments	9
3.1 Boundary layers.	9
3.1.1 Viscous layers	10
3.2 Discretisation	12
3.2.1 Momentum, turbulent and free-surface equations.	12
3.2.2 Time and pressure-velocity coupling.	15
3.2.3 Algorithm	16
3.3 Turbulence modelling.	16
3.3.1 SST-Menter	16
3.3.2 EASM	17
3.3.3 DES-SST	18
3.3.4 Concluding	18
3.4 Overset	19
3.5 Boundary conditions	19
3.5.1 Exterior boundaries	19
3.5.2 Solid boundaries.	20
3.6 Simulation set-up.	20
3.6.1 Model	20
3.6.2 Domain	21
3.6.3 Grid	22
3.7 Numerical results	24
3.7.1 Boundary layer (y^+)	24
3.7.2 Pressure over hull surface	24
3.7.3 Vortex identification	25
3.7.4 Forces	28
4 Towing tank experiments	31
4.1 Measurement set-up	31
4.1.1 Turbulent stimulation	33
4.1.2 Alignment of the components	34
4.2 Approach	35
4.3 Elaboration procedure	36
4.3.1 Turbulence stimulation	36
4.3.2 Rotation of forces	37

4.4	Results	38
4.4.1	Hull and keel forces	38
4.4.2	Rudder forces	39
4.4.3	Comparison previous experimental data.	42
4.5	Conclusions of the experimental results	44
5	Uncertainty assessment	45
5.1	Code verification	45
5.2	Solution verification	45
5.2.1	Possible sources of errors in CFD simulations	45
5.2.2	Discretisation error	46
5.2.3	Grid development for the grid refinement	47
5.3	Uncertainty assessment of the towing tank experiments	48
5.4	Solution validation	50
5.5	Results of the uncertainty assessment.	51
5.5.1	Verification other variables.	53
6	Analysis of results	57
6.1	Comparison between experiments	57
6.1.1	Model forces	57
6.1.2	Rudder forces	57
6.2	In-depth analysis	59
6.2.1	Drag part.	60
6.2.2	Lift part	62
7	Conclusions and recommendations	67
7.1	Recommendations	68
	Bibliography	71
A	Computational Fluid Dynamics	75
A.1	Derivation of the RANS equations.	75
A.2	Turbulence modelling.	76
A.3	Discretisation	77
B	Lines plan	79
C	Original test matrices	81
D	Results of the experiments	85
D.1	Hull related plots	86
D.2	Keel related plots	88
D.3	Rudder related plots	89
E	Experimental uncertainty assessments	95
E.1	Model.	96
E.2	Keel	97
E.3	Rudder	98
F	Uncertainty assessment	99
F1	Test case $\beta = 3^\circ$ and $\delta = 0^\circ$	100
F2	Test case $\beta = -3^\circ$ and $\delta = -5^\circ$	104
G	CFD results discussed in chapter 6	109
G.1	Drag part	110
G.2	Lift part	112

Nomenclature

Upper case

A	Log-law constant	[-]
A_{lat}	Lateral area	[m^2]
AR	Aspect ratio	[-]
AR_e	Effective aspect ratio	[-]
B	Beam of the model	[m]
B	Log-law constant	[-]
B_{WL}	Beam on waterline	[m]
C_D	Drag coefficient	[-]
C_f	Friction coefficient	[-]
C_L	Lift coefficient	[-]
C_p	Prismatic coefficient	[-]
C_{Di}	Induced drag coefficient	[-]
CFL	Courant-Friedrichs-Lewy condition, see equation 3.20.	[-]
CLR	Centre of lateral resistance	[-]
D	Diffusion factor	[-]
D	Experimental results	
D_{FS}	Diffusion factor of the free-surface	[-]
E	Difference between experimental and numerical results	
F_0	outer layer velocity gradient for the logarithmic region	[-]
F_1	Function	
F_{DES}	Function	
F_x	Drag force	[N]
F_y	Side force	[N]
Fn	Froude number	[-]
$H.O.T$	Higher order terms	[]
K	Turbulent kinetic energy	[m^2/s^3]
L	Length of the model	[m]
L_{ref}	Reference length	[m]
L_{WL}	Waterline length of the model	[m]

LCB	Length location of centre of buoyancy	[%]
M_{x_r}	Roll moment of the rudder	[Nm]
M_{z_h}	Yaw moment of the model	[Nm]
$\mathcal{P}_{i,j}$	Rate of production of Reynolds stress	[m ² /s ³]
Q	Second invariant	[1/s]
$\mathcal{R}_{i,j}$	Pressure-rate-of-strain tensor	[m ² /s ³]
R	Discrimination ration	
R_r	Residual resistance	[N]
R_t	Total resistance	[N]
Re	Reynolds number	[-]
\mathbf{S}	Strain rate tensor	[1/s]
S	Numerical results	
S	Wetted area	[m]
S_c	Wetted area of the barehull	[m]
T_c	Draught of the canoe body	[m]
U	Flow velocity in x -direction	[m/s]
U_0	Undisturbed flow velocity in x -direction	[m/s]
U_D	Experimental uncertainty	
U_{input}	Parameter uncertainty	
U_{num}	Numerical uncertainty	
U_{val}	Validation uncertainty	
V_0	Undisturbed flow velocity	[m/s]
V_{ref}	Reference velocity	[m/s]
V_{wake}	Flow velocity in the wake	[m/s]
V_s	Velocity of the model	[m/s]
Lower case		
b	Span of an appendage	[m]
c	Chord length of the appendage	[m]
f_1	inner layer velocity gradient for the logarithmic region	[1/s]
g	Gravitational Constant	[m/s ²]
Δh	Grid size	[m]
h_i	Grid size	[m]
n	Number of refinements	[-]
p	Observed order of grid convergence	

p	Pressure	[Pa]
r	Grid refinement factor	[]
Δt	Time step	[s]
t	Thickness of the appendage	[m]
t	Time	[s]
u	Flow velocity in x direction	[m/s]
u^+	Normalised near wall flow velocity	[-]
u_τ	Friction velocity	[m/s]
v	Flow velocity in y direction	[m/s]
w	Flow velocity in z direction	[m/s]
x	Dimension	[m]
y	Dimension	[m]
y^+	Non-dimensional wall distance	[-]
z	Dimension	[m]

Greek Symbols

α	Angle of attack	[°]
α	Coefficient for numerical uncertainty estimate	
β	Leeway angle	[°]
β^*	Constant of SST-model	[]
δ	Boundary layer thickness	[m]
δ	Rudder angle	[°]
δ_ν	Viscous length scale	[m]
δ_{ij}	Kronecker delta	[m ² /s ³]
δ_{model}	Modelling error	
ϵ_Φ	Discretisation error	
ϵ	Rate of dissipation of turbulent kinetic energy	[m ² /s ³]
θ	Pitch angle	[°]
κ	Von Kármán constant	[-]
Λ	Sweep back angle	[°]
λ_2	Second eigenvalue	[]
μ	Dynamic viscosity	[kg/ms]
ν	Kinematic viscosity	[m ² /s]
ρ	Fluid density	[kg/m ³]
τ_w	Wall shear stress	[Pa]

Φ	Variable	
ϕ	Roll angle	[°]
ϕ	Variable	
Φ_D	Downwind variable	
Φ_f	Variable at cell face	
Φ_{UU}	Far upwind variable	
Φ_U	Upwind variable	
$\tilde{\Phi}$	Normalised variable	
Ψ	Yaw angle	[°]
Ω	Rotation tensor	[1/s]
ω	Specific dissipation rate of turbulent frequency	[1/s]
∇	Gradient vector	[1/s]
∇	Volume	[m ³]
∇_c	Volume of the canoe body	[m ³]



Introduction

In the past decades numerous research in the towing tank of the TU Delft has been done to sailing yachts, from which a VPP program is developed, which can help designers assess the performance of their concept designs. A part of the performance analysis is the assessment of the location of the centre of lateral resistance and the influence of the rudder on location. In addition, the rudder forces are also of importance when assessing the manoeuvrability of sailing yachts.

In the early '00 of this century Keuning et al. [32] looked into the hydrodynamic forces on the rudder and the influence of the hull and keel on these forces. The main aim of this research was to find the downwash angle and the flow reduction on the rudder, due to the presence of the keel and hull. In addition to this, they have assessed the lift and drag forces on the rudder and found an unexplainable phenomenon in the lift curve of the rudder, namely an asymmetric stall lift curve.

This study continues on the findings of the research conducted by Keuning et al. [32]. The aspects which are examined in greater detail are the lift and drag forces on the rudder, with varying rudder angles. The study contains a computed fluid dynamics (CFD) analysis and towing tank tests, the latter are executed to validate and expand the experimental data found by Keuning et al. [32].

The goal for this research is to find and clarify the physical phenomenon which induces the rudder to stall at smaller rudder angles when subjected to a negative rudder angle (during bearing away). This leads to the main question to be answered in this report is: What physical phenomenon is at the basis of the asymmetric stalling behaviour on the rudder of a sailing yacht?

Expected is that this phenomenon is caused by a flow interaction of the keel tip vortex on the low pressure side of the rudder.

The main research question is supported with the following sub-questions:

- What is the exact location and shape of the lift curve near the negative stall angle?
- What are the best settings for the CFD simulations?
- What is an expectable uncertainty for the experiments?
- Are CFD simulation an useful tool to assess the problem?

These sub-question are at the basis of the structure of the report, the latter will be answered in chapter 7.

Structure of the report

This report is constructed as follows; in chapter 2 the previous research of Keuning et al. [32] is explained in more detail; besides this summery a short analysis will be given on the physical phenomena related to the problem. Chapter 3 discusses the numerical experiments, relevant settings are highlighted and the results are presented. The towing tank experiments will be discussed in chapter 4 and follow the same approach as chapter 3; first the important aspects of the set-up are discussed, after which the results are presented. The validity of the two experiments, mainly the numerical part, and the uncertainties are discussed in chapter 5. An analysis and comparison of the results of the two types of experiments is given in chapter 6 and the overall conclusions are given in chapter 7. Finally, some other details and figures for reference purposes are presented in the Appendices.

2

Background

This chapter gives more insight into the research to the problem and the physics discovered by it. The study of Keuning et al. [32], and the studies it is based on, are considered in more detail. After which some relevant physical effects are presented.

2.1. Previous research

As explained in chapter 1 the study of Keuning et al. [32] is the basis of this research. The problem assessed in this research is an unexpected stall behaviour of the rudder. Figure 2.1 presents an example of the rudder lift curve found by Keuning et al. [32], the figure shows the lift curve behind a high aspect ration keel (keel 5).

The problem of unexpected stall behaviour of the rudder was only a small part of the study. The entire study of Keuning et al. [32] contained analysis on the residual resistance of the keel, rudder resistance and flow velocity reduction and the downwash angle of the keel.

For the residual resistance of the keel an increases of the resistance is found when the center of buoyancy is brought further from the surface.

As for the flow velocity reduction, this is obtained from the difference in resistance ($\frac{Rr_{wake}}{Rr_{free}} \approx 0.9$). It was concluded, that the free velocity fraction is the following: $\frac{V_{wake}}{V_0} \approx 0.95$. It appears that the velocity fraction depends on the Froude number, so wave generation and orbital velocity are a part the flow velocity reduction.

The downwash angle of the keel causes the angle of attack of the rudder to decrease by a couple of degrees. Figure 2.2 shows an example of the results of the downwash angles found by Keuning et al. [32]. The figure shows that the angle of attack on the rudder indeed decreases and that the relative influence of the downwash angle increases with the leeway angle. As seen before, this downwash angle is of importance for the rudder lift curve.

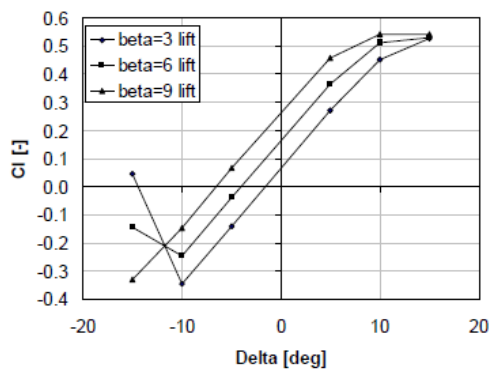


Figure 2.1: The lift curve of the rudder behind keel 5 found by Keuning et al. [32].

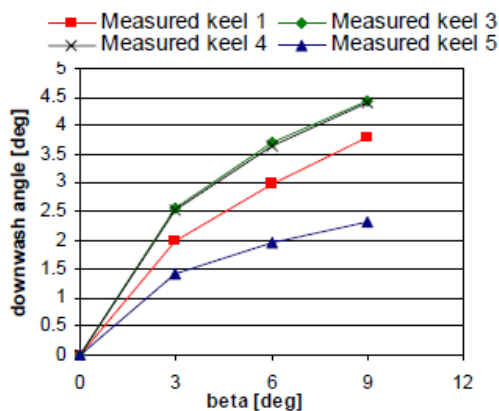


Figure 2.2: Downwash angle versus leeway angle for a number of keels without heel [32]

Before the study of Keuning et al. [32], J.A. Keuning and K.J. Vermeulen performed a couple of studies on the yaw balance of a sailing yacht. Two studies have interesting comments on the rudder performance. The first, by Keuning and Vermeulen [30] is on the straight line yaw balance of a sailing yacht and the second is on developing a tacking method by Keuning et al. [31].

The latter study gives an interesting comment on the lift reduction of the rudder. Keuning et al. [31] state the following: "when the tip vortex 'hits' the rudder a strong reduction may be expected."

The study by Keuning and Vermeulen [30], has an interesting comment on the downwash angle of the keel. They state that the sidewash on the rudder is caused by the rolled up vortex sheet of the keel.

It appears that the issue discussed in Keuning et al. [32] was already discovered in previous studies and that the authors of both studies assume that the performance of the rudder is largely influenced by vortices originating from the keel.

2.2. Side force and yaw moment

Most of the studies in the past years looked into a model for the center of lateral resistance. All the underwater bodies (hull, keel and rudder) contribute to this. In this section the effect of these bodies will be explained.

2.2.1. Extended keel method

The extended keel method introduced by Gerritsma [16], assumes that the most significant part of the side forces of a sailing yacht is produced by its appendages. The lift for these appendages can be approximated using lift theories. In Gerritsma's theory [16] the contribution by the hull is taken into account by extending the keel(/rudder) to the waterline.

One of the equations to estimate the lift on the appendages proposed by Gerritsma [16] is presented below:

$$\frac{dC_L}{d\alpha} = \frac{5.7AR_e}{1.8 + \cos\Lambda \sqrt{\frac{AR_e^2}{\cos^4\Lambda} + 4}} \quad (2.1)$$

Where AR_e is the effective aspect ratio of the appendage, this is twice the AR because of the hull functioning as an end plate. Λ is the sweep back angle of the appendage and α is the angle of attack. From the equation is concluded that the slope of the lift curve is mainly dependent on the aspect ration and the sweep angle [30].

2.2.2. Slender body theory

Nomoto and Tatano [45] proposed to add the slender body lifting line theory to Gerritsma's method. So the contribution of the hull has been added to the extended keel method.

A slender body is a body where the breadth and depth are much smaller than its length. When the body is positioned obliquely in an ideal (inviscid) flow, a yaw moment arises on the body. This moment is known as the Munk moment. Because of the point symmetry in the force distribution, the idealised Munk moment can be considered as a pure couple with no resultant side force, the d'Alambert's paradox, see figure 2.3.

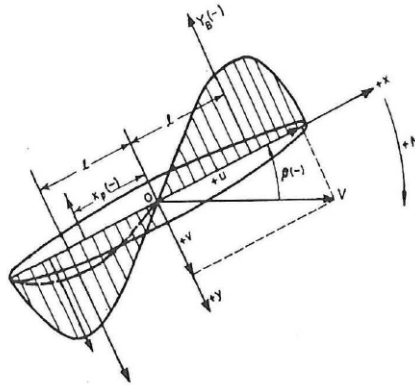


Figure 2.3: Force distribution acting on a slender body in an oblique ideal flow [37].

The Munk moment will lose its couple effect due to flow separation and vortex generation downstream. As a result of these viscous effects, the pressure and the force distribution on the aft ship reduces, which in turn results in a side force on the body [37], [45], [30].

The flow separation originates from the adverse pressure gradients of the hull. Besides the separation, the keel (not the appendage) will shed vortices, due to the keel being a sharp edge.

These viscous effects are of interest when one is assessing hull-rudder interaction. Figure 2.4 shows a similar effect in the lift curve as in figure 2.1, while no keel is present. This would lead to the possibility that this vortex shedding and separation of the hull would interfere with the flow around the rudder. The same pressure drop which reduces the couple in the Munk moment could also have an effect on the pressure distribution around the rudder.

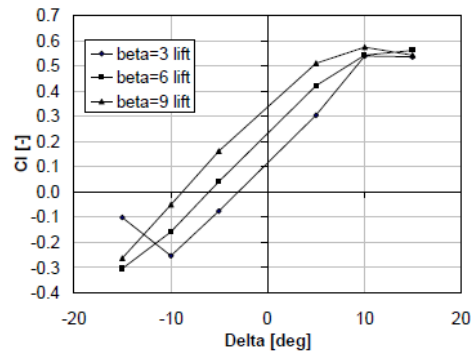


Figure 2.4: Lift forces of the rudder without keel fitted to the model, Keuning et al. [32].

2.2.3. Interaction of wings

As this research is on the interaction between a body and two wings, interesting aspects could be found in studies to the influence of the hull and wing of the tailplane of an aircraft.

First, Hoerner [17] dedicate a small paragraph on tandem wing arrangement. Here he states that the rear airfoil is so to speak climbing in the vortex sheet of the front foil. The rear airfoil has a different angle of attack due to the downwash. Also, the front foil is influenced by the rear foil, depending on the type of configuration; positively or negatively.

In this study the forces of the tailplane affecting the total forces are examined, but also the flow characteristics around the aircraft, as well as the boundary layer around the tailplane.

For this study, wind tunnel experiments have been performed with a couple of tailplane configurations. The forces and moments on the hull have been measured, as well as the wake for which two rakes were used; the rakes measured the dynamic pressure around the model. The two rakes measured at the boundary layer and at a large distance from the body. The results are corrected for wind tunnel blockage.

Three statements were made in the conclusions. The first two are on the mounting positions, negligible interference was found for the mounting positions away from the body and a small interference of the body on the tailplane lift was found for the mounting position on the body. The final statement might be more relevant for this study: "the body interference is a function of the downwash field, this interference worsens when a extended planform wing is used or a clean wing with high-lift devices."

Below some additional comments to the tailplane interference are listed:

- A partial stall at 13° is found; it is written to the poor state of the leading edge of the wing.
- In an isolate tailplane test, a possible partly separation near the leading edge is found, occurring at 6° incidence.
- Lovell [38] states: "After the location of stall the shape of the curve is determined by two factors: the fuselage boundary layer and the spanwise static-pressure gradient caused by the potential flow field around the wing-body combination." Also, the dynamic pressure is not uniformly reduced, because

of the boundary layer and the flow separation moving inboard from the tip, as the angle of incidence increases.

- In other statements, Lovell [38] states that the wing planform has a large influence on the wake measured at the tailplane. And the wing-body combination has a large influence of the vortex-sheet, especially in the inboard region.
- The boundary layer across the tailplane, first, has a typical flat-plate boundary layer in adverse pressure gradients. "After the stall angle, the boundary layer is effected by presumably a reduced dynamic head in the local free stream, and the boundary layer is similar to that of a flat-plate boundary layer."
- The final interesting remark of this paper, Lovell [38] states: "The vortices leaving the wing-body junction can be seen to cause cross flow on the body immediately adjacent to the wing but they are sufficiently weak for them to have little effect on the surface flow pattern at the tail."

Finally, this study provides some interesting figures on the interaction effect on the lift and drag curves. In the drag and lift curves no particularities are shown. This might be because only the model forces are measured. In the boundary layer measurements some interesting aspects are shown, for example an decelerating flow for the extended planform wing. The latter figures show on one axis no dimensionless distance, without clarification of the absolute distance it is difficult to make a qualitative analysis.

2.3. Vortex dynamics

As stated in section 2.1, the most likely explanation of the unexpected behaviour in the lift curve of the rudder is the tip vortex of the keel. The aim of this section is to get a better understanding of the physics by discussing the relevant vortex dynamics.

Kundu et al. [33] states: "Vorticity is a vector field that is twice the angular velocity of a fluid particle. A concentration of codirectional or nearly codirectional vorticity is called a vortex. Fluid motion leading to circular or nearly circular streamlines is called vortex motion." In other words, a vortex is formed when a concentration of fluid particles with a certain rotation and a circular streamline are present. From Kundu et al. [33] it becomes clear that a rotation of fluid particles does not necessarily form a vortex. An important comment on this subject comes from Kundu et al. [33]: "A vortex tube cannot end in the fluid and has to make a closed loop".

Vortices can be represented in terms of vortex lines or as a vortex tube. Vortex lines are constructed from the tangent to the local vorticity vector and vortex tubes are closed surfaces which have a vortex line in the center. According to Kundu et al. [33], the strength of a vortex tube defined as the circulation computed over the closed surface of the tube. These definitions of are of importance in the vortex identification, discussed in chapter 3 [33], [27].

Within the turbulent boundary layer all kinds of vortex structures can be found and even could grow to influential vortices or vortex streets. The latter structures are seen in flows around bluff bodies, where flow separation occurs due to adverse pressure gradients. This separation forms eddies, which could detach from the object due to instability in the flow, forming vortices. For example a flow around a cylinder forms a von Karman vortex street for sufficient high Reynolds numbers [33], [48].

Besides vortices originating from flow separation, large eddy structures could also originate from turbulent boundary layers. On the edge of the boundary layer (the line between the turbulent flow and the outer flow, called viscous super-layer by Pope [48]) valleys of non-turbulent flow could be formed; from these valleys large eddy structures could be separated [48].

Around the near wall regions pairs of counter rotating vortices are detected and are identified as dominant vortical structures, by [48]. Further away from the wall horseshoe vortices or hairpin vortices are identified by [48] as vortical structures.

2.3.1. Vortices from foils

In this study the vortices are expected to originate from the working of foils. This section gives a short introduction on the vortex structures originating from lift producing foils. I. Abbott [20] and Hoerner [17] both give the following analysis on the vortices from a foil:

In airfoil theory it is commonly known that lift is a function of the circulation around a foil. A foil experiences a circulation around its span [33]. For foils of finite length the circulation (bound vortices) decreases towards the tips, because of this trailing vortices are formed, see figure 2.5. These trailing vortices form a vortex street. Hoerner [17] approaches the vortex street more theoretically; the vortex street becomes a spanwise sheer flow due to a summation of the circulation of the trailing vortices. The effect of this vortex street is a downward (for positive lift) velocity component and is called the downwash.

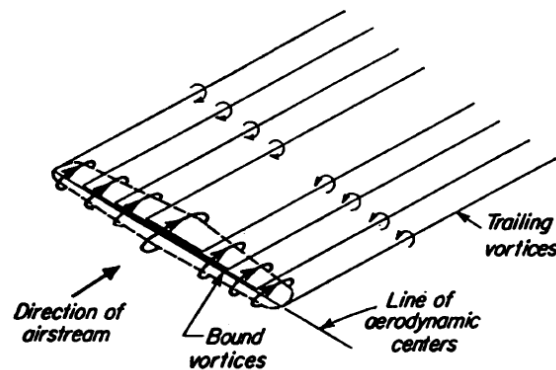


Figure 2.5: A schematic representation of the circulation around a foil [20].

The downwash has a rotating effect on the flow around the foil in the direction of the circulation. The consequence is a decrease in the effective angle of attack and subsequently the lift and drag forces are rotated. The rotation of the lift forces gives an additional drag component in the undisturbed flow direction, this is the induced drag or the drag due to lift. The angle at which the flow around the foil is rotated is called the induced angle of attack, this is generally half of the downwash angle.

Due to the effect of a pressure gradient over the wing tip has the flow the tendency to flow across the wing tip. The flow component from the high pressure side is combined with the flow over the low pressure side and forms a vortex. This process starts from the leading edge of the wing and takes place as soon as lift is generated. As a result of the circulation, the vortex street and the viscous wake are rolled up into the generated tip vortex core, increasing the diameter of the tip vortex. The diameter of the tip vortex grows with roughly the square root of the downstream distance, according to Devenport et al. [9]. Apart from the increasing tip vortex, the vortex is dissipated in the direction of the flow and moves slowly inboard [20], [17], [9].

3

Numerical experiments

In this chapter the set-up and the results of the numerical experiments will be discussed. First, some background will be discussed which is relevant for these simulations. After this background the simulation set-up is touched upon. The chapter will be concluded with a short section on the results.

3.1. Boundary layers

As discussed in Kundu et al. [33], Pope [48], White [56] and Weymouth [55] a turbulent boundary layer consists of a number of regions, namely:

1. Inner region; extends from the wall to $y^+ \approx 30$. This layer contains the so called viscous sub-layer ($y^+ < 5$) and the buffer layer ($5 < y^+ < 30$).
2. Overlap region; this is the region where the flow is dominated by the Reynolds stress. This region lies between the inner region and the outer flow region.
3. Outer flow region; extends from $y/\delta > 0.2$. This is the majority of the domain and can be seen as the outer flow and resembles a free shear flow.

Note: the y^+ value is the normalised distance to the wall and u^+ is the normalised near wall velocity. By the following equations:

$$u^+ = \frac{\bar{u}}{u_\tau} \qquad y^+ = \frac{y}{\delta_v} \qquad (3.1)$$

$$u_\tau = \sqrt{\frac{\tau_w}{\rho}} \qquad \delta_v = \frac{\nu}{u_\tau} \qquad (3.2)$$

Equation 3.1 and equation 3.2 show that y^+ is a local Reynolds number and thus its value determines the relative importance of viscous and turbulent processes [48].

In the viscous sub-layer assumed is that the viscous stress dominates over the Reynolds stress, i.e. laminar behaviour. This means that the shear stress can be written in the following way:

$$\tau_w = \mu \frac{\partial \bar{u}}{\partial y} \qquad (3.3)$$

$$\rho u_\tau^2 = \mu \frac{\partial \bar{u}}{\partial y} \qquad (3.4)$$

From equation 3.3 can be concluded that the velocity profile in the inner region in terms of the normalised flow variables is the following: $u^+ = y^+$ [48],[55].

According to Kundu et al. [33], neither the viscous stresses nor the Reynolds stresses are negligible in the buffer layer. This region is dynamically important, because it is the location where the turbulence production takes place. For this region it is difficult to find an expression; several studies have suggested a solution,

for example Monkewitz et al. [41] and Spalding [52] [56], [48], [33], [44].

The overlap region, also called the logarithmic region, needs to couple the inner layer velocity gradient (f_1) to the outer region velocity gradient ($F_0 = \frac{U_0 - U}{u_0}$), done with the use of the following equation:

$$y^+ f_1'(y^+) = - \left(\frac{y}{\delta} \right) F_0' \left(\frac{y}{\delta} \right) \quad (3.5)$$

Both sides are independent, so they need to be equal to the same constant $\frac{1}{\kappa}$. After integration the log law is found [56], [48], [33], [44].

$$u^+ = \frac{1}{\kappa} \ln y^+ + B \quad \frac{U_0 - U}{u_0} = - \frac{1}{\kappa} \ln \left(\frac{y}{\delta} \right) + A \quad (3.6)$$

Deriving the velocities in the overlap region could be assumed to be questionable, as the assumption for the inner region velocity is not completely fair, due to the buffer layer. Although, the logarithmic law is compared to experimental data, which shows good agreement for the region between $30 < y^+ < 300$ [56], [48], [33], [44].

The laminar boundary layers have a simpler velocity profile, as the outer flow in the laminar flow is assumed to behave like an inviscid flow. Near the wall the flow velocity is assumed to be zero (no-slip) and at a distance from the wall, outside the boundary layer, the flow velocity is equal to the velocity at infinite distance. Furthermore, it is assumed that the flow in z-direction is non-existent in the boundary layer. Using these assumptions, and that the flow in z-direction is two dimensional, the following relevant function can be found:

$$\frac{\partial u}{\partial x} + \frac{\partial v}{\partial y} = 0 \quad (3.7)$$

$$u \frac{\partial u}{\partial x} + v \frac{\partial u}{\partial y} = - \frac{1}{\rho} \frac{\partial p}{\partial x} + \nu \frac{\partial^2 u}{\partial y^2} \quad (3.8)$$

$$0 = - \frac{\partial p}{\partial y} \quad (3.9)$$

To express the boundary layers thickness Kundu et al. [33] mentions three definitions for the boundary layer. First, the δ_{99} : the distance at which the flow velocity is 99% of the flow velocity at infinite distance. Secondly, there is the displacement thickness; this is the distance the wall needs to be displaced outward to maintain the same mass flux. Thirdly, there is the momentum thickness, which corresponds to the loss of momentum. The displacement thickness is the commonly used thickness, this thickness is also interpreted as the distance of the streamlines outside the boundary layer [33], [44].

In Newman [44] figure 3.1 is presented, showing a comparison of the turbulent and laminar boundary layer thickness. It is showed, in this figure, that the turbulent boundary layer is larger and has a higher near wall velocity, which results in an increased shear stress.

According to NUM [47], HEXPRESS uses two methods in the viscous layer insertion: the fixed first layer thickness and the variable first layer thickness.

3.1.1. Viscous layers

NUMECA [47] uses viscous layers to resolve the flow in the boundary layers. These layers are high aspect cell inserted near the wall, at an user defined distance. NUMECA [47] uses two methods for this; fixed first layer and variable first layer. The first method is the preferred method and will be discussed below.

In the fixed first layer method, a first layer thickness and the number of viscous layers are to be determined for each object in the domain. The first layer thickness is determined from the y^+ . This y^+ is estimated with the following equation:

$$y^+ = \max \left(y_{min}^+, \min \left(\frac{30 + (Re - 10^6) * 270}{1e9}, y_{max}^+ \right) \right) \quad (3.10)$$

$$y_{min}^+ = 30 \quad (3.11)$$

$$y_{max}^+ = 300 \quad (3.12)$$

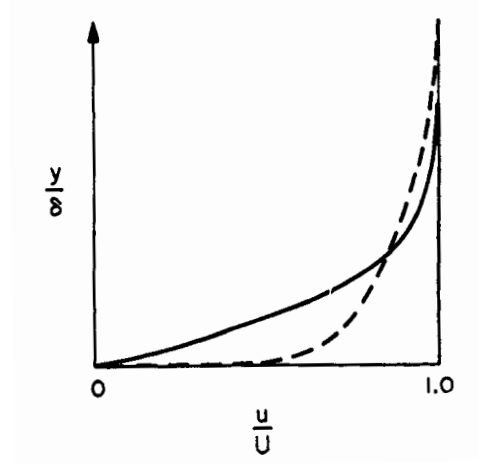


Figure 3.1: A comparison between the laminar (solid line) and the turbulent (dashed line) boundary layer thickness [44]

NUMECA [46] advises to locate the first viscous layer in the overlap region and probably uses the log-law to determine the flow characteristics. When the y^+ is determined NUMECA [46] determines the first layer distance with the following formula:

$$y = 6 \left(\frac{V_{ref}}{\nu} \right)^{-\frac{7}{8}} \left(\frac{L_{ref}}{2} \right)^{\frac{1}{8}} y^+ + H.O.T. \quad (3.13)$$

Another way of estimating the first layer distance is to use the definition of y^+ and complete it with a estimate for the friction coefficient, see equations 3.14, 3.15.

$$y = \frac{\nu Y^+}{u_\tau} \quad (3.14)$$

$$u_\tau = \sqrt{\frac{\tau_w}{\rho}} = \sqrt{\frac{1}{2} V^2 C_f} \quad (3.15)$$

Two options are given for the friction coefficient, a power law and the ITTC friction coefficient:

$$C_f = \frac{0.027}{Re_x^{\frac{1}{2}}} \quad (3.16)$$

$$C_f = \frac{0.075}{(\log Re - 2)^2} \quad (3.17)$$

Table 3.1 shows an example of the determination of the first layers distance, using the three mentioned methods. In the table, the y^+ distance is estimated and determined, in the first rows one can see that the difference is quite small. Note, in the simulations the y^+ for the rudder should be around one in order to capture the stalling effect better; however, this would not make a fair comparison between the different first wall distance estimation methods.

The difference in y^+ estimated and determined has only a small influence on the wall distance. A larger influence can be found when different equations are used to determine the first wall distance. The wall distance proposed by NUMECA [46] gives the highest value, almost by a factor of 1.5, compared to wall distances determined by a friction coefficient. Using the ITTC [23] friction formula or a power law, will result in small differences in the distance. This difference increases with a decreasing reference length.

The wall distance used in the grids will be calculated by the ITTC [23] friction formula, with a determined y^+ distance.

Table 3.1: The first layer cell distance for the three components, calculated with different methods, discussed in section 3.1. The estimated values of y^+ use the y^+ calculated with the equation proposed by NUMECA [46]. Note: the final first layer distance of the rudder is near one, these values are used for the comparison.

	Hull	Keel	Rudder
$y^+_{determined}$	30	30	30
y^+_{NUMECA}	31.1	30	29.8
Determined y^+			
$y_{wall_{NUMECA}}$	$6.3 \cdot 10^{-4}$	$4.7 \cdot 10^{-4}$	$4.3 \cdot 10^{-4}$
$y_{wall_{ITTC}}$	$4.1 \cdot 10^{-4}$	$3.2 \cdot 10^{-4}$	$2.9 \cdot 10^{-4}$
$y_{wall_{power}}$	$4.3 \cdot 10^{-4}$	$3.6 \cdot 10^{-4}$	$3.5 \cdot 10^{-4}$
Estimated y^+			
$y_{wall_{NUMECA}}$	$6.6 \cdot 10^{-4}$	$4.7 \cdot 10^{-4}$	$4.2 \cdot 10^{-4}$
$y_{wall_{ITTC}}$	$4.2 \cdot 10^{-4}$	$3.2 \cdot 10^{-4}$	$2.9 \cdot 10^{-4}$
$y_{wall_{power}}$	$4.5 \cdot 10^{-4}$	$3.6 \cdot 10^{-4}$	$3.4 \cdot 10^{-4}$

Usually turbulence stimulators are used during the experiments to match the flow conditions in full scale and in model scale. In CFD this could be done more realistic with increasing the hull roughness. However, NUMECA [43] uses only a smooth wall for its calculations. This could result in a probable mismatch between the amount of turbulence and the viscous resistance around the model in the CFD simulations and the experiments; it will be beneficial in future studies to assess the need for turbulence stimulators.

3.2. Discretisation

An important part of the numerical computations is the discretisation of temporal and spatial variables; it is even fundamental for a numerical method to discretise. As with all aspects of computational flow dynamics, multiple methods of the discretisation of time and spacial derivatives are available. In ISIS the discretisation is only partly accessible as a user input; mainly the discretisation of the momentum, turbulent and free-surfaces equations are open for user input, these options will be discussed in section 3.2.1. The other parts of the discretisation, as for example the temporal or the pressure velocity coupling, are quite complicated and discussing them in detail would exceed the aim of this chapter. For details on this part of the discretisation see Nantes and CNRS [43]. In Appendix A the basics of the discretisation will be explained.

NUMECA [43] uses a finite volume method to discretise the flow. This method solves the momentum and mass conservation equations in integral form. The velocity field is obtained from momentum conservation and the pressure field follows from adapted mass conservation equations [43].

3.2.1. Momentum, turbulent and free-surface equations

The options given in fineMarine to discretise are mostly upwind based discretisation methods. A couple of given options are single differencing schemes, for example: Upwind differencing scheme (UDS), Centred Differencing Scheme (CDS) or Second Order Upwind differencing scheme (SOU). In addition to these, there are a number of schemes which have combined schemes, as for example Hybrid, Gamma Differencing Scheme (GDS) or ALVSMART.

The latter schemes switch between UDS and a different higher order scheme. The differencing schemes in NUMECA are all linear interpolation between the cells, the error made in this interpolation is the order of a differencing scheme. NUMECA gives as a option to use schemes which range from first order (UDS) to third order (QUICK), the higher the order of a differencing scheme the more accurately the solution will be solved. In addition, some structures in the flow will not be resolved correctly when a wrong differencing scheme is chosen. For example, the vorticity is the curl of the velocity, thus to find the gradient of the velocity at least a third order differencing scheme has to be used, if the error is assumed to be the delta of the velocity [15]. It is important to get the differencing scheme as high as possible, because in this research these flow structures will be of interest.

Apart from this accuracy a discretisation needs to comply to three conditions, see Appendix A, one of those is boundedness. This boundedness states that a value in a cell or cell face needs to lie between the

upwind cell value and the downwind cell value [34], to ensure no strange peaks occur in the flow. The problem with the higher order methods is that the interpolation takes place over multiple cells and by doing so it does not satisfy the boundedness condition. Gaskell and Lau [13] solved this problem by introducing the convection boundedness criterion (CBC).

The CBC works in the following way: in figure 3.2 four locations are shown, UU, U, f and D, which represent the far upwind cell centre, the upwind cell centre, the face and the downwind cell centre. At these locations the following values of a variable Φ can be found: Φ_{UU} , Φ_U , Φ_f and Φ_D . The value of Φ_f is going to be approximated, bounded by the results of other nodes. The easiest way to bound the value for Φ_f is to normalise it with the values of Φ_{UU} and Φ_D with the use of equation 3.18, as proposed by Gaskell and Lau [13]. A schematic representation of the normalisation and the bounded values of Φ_U and Φ_f can be seen in figure 3.3.

$$\tilde{\Phi} = \frac{\Phi - \Phi_{UU}}{\Phi_D - \Phi_{UU}} \quad (3.18)$$

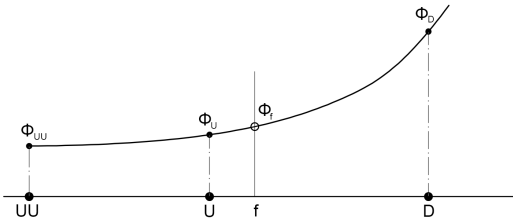


Figure 3.2: The definition of cell values around a cell face used in the convection boundedness criterion (CBC).

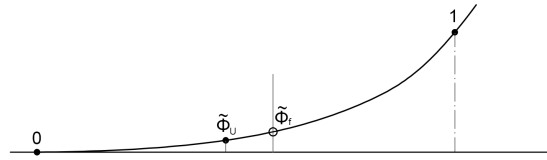


Figure 3.3: The definition of the normalised cell values around a cell face used in the CBC.

Figure 3.3 shows that the magnitude of both $\tilde{\Phi}_U$ and $\tilde{\Phi}_f$ needs to be between zero and one, bounded by the normalised values of Φ_{UU} and Φ_D . This can also be seen in figure 3.4, the so-called Normalised Variable Diagram (NVD), where the $\tilde{\Phi}_U$ and $\tilde{\Phi}_f$ are plotted on the axis, showing the relation between the values of the upwind cell and the face of interest for the different discretisation schemes. The figure illustrates that the approximation is bounded by the upwind differencing scheme (UDS) and the downwind differencing scheme (DDS), the UDS is the only scheme which satisfies the boundedness criterion unconditionally. The DDS bounds the value for Φ_f in an opposite way as the UDS, the Φ_f cannot exceed the value ϕ_D [13], [43], [26], [42].

Figure 3.4 also shows the behaviour of different discretisation schemes, which do not necessarily satisfy the boundedness criterion unconditionally. All three examples given intersect the point $(\frac{1}{2}, \frac{3}{4})$, although they intersect at different locations on the y -axis. The passing through the point $(\frac{1}{2}, \frac{3}{4})$ indicates a second-order accuracy and then doing so with a slope of $\frac{3}{4}$, indicates third-order accuracy [36].

To summarise, the higher order discretisation schemes are only usable within the box bounded by UDS and DDS (the grey area), in here they satisfy the boundedness criterion. This method is used in a number of discretisation schemes within ISIS, in figure 3.5 an example is given for the gamma-differencing scheme (GDS) and in figure 3.6 an example for the AVLSMART scheme. In these schemes the UDS is used when the solution is outside of the CBC; within the CBC the central-differencing scheme (CDS) or quadratic upstream interpolation (QUICK) are used. Within these two methods a blended function is used to transfer from UDS to CDS or QUICK and vice versa. The locations from where this blending occurs is different for each method and case [43].

FineMarine has also the option to use discretisation schemes without this convection boundedness criterion, for example upwind or second order upwind. Also, an option is given to use the hybrid discretisation scheme. This scheme is a combination of central-differencing and upwind differencing schemes. The switch in this case is performed using the Peclet number, which is the relation between the convective and diffusive transport in the flow.

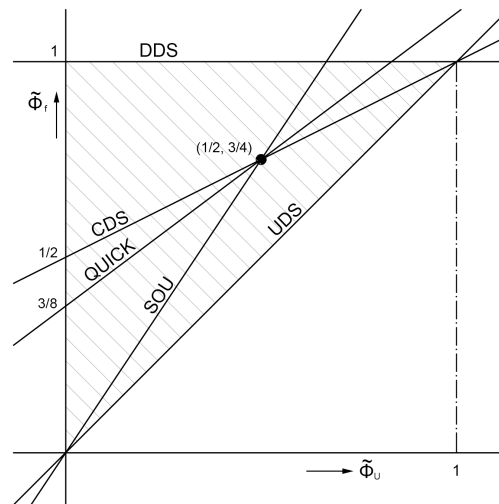


Figure 3.4: The Normalised Variable Diagram for a number of discretisation methods. The definitions are given in figure 3.2.

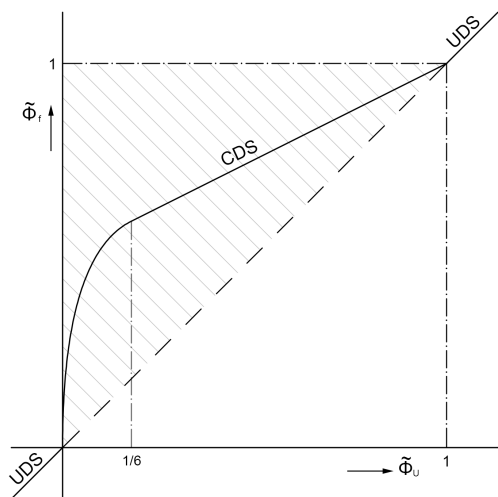


Figure 3.5: The NVD of the Gamma-differencing scheme. Where UDS is the upwind-differencing scheme and CDS is the central-differencing scheme.

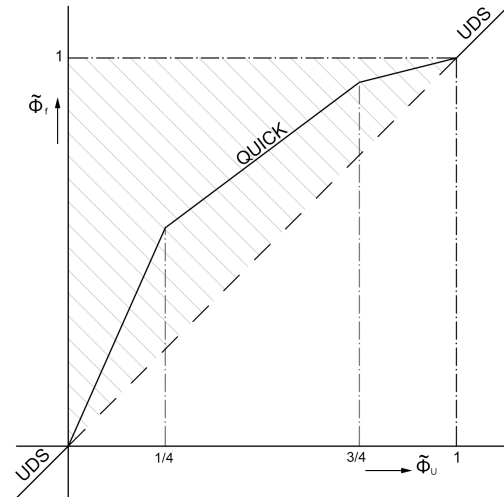


Figure 3.6: The NVD of the AVLSMART scheme. Where UDS is the upwind-differencing scheme and QUICK is the quadratic interpolation scheme.

The above described options are for the turbulence and moment discretisation. For the discretisation of the free-surface a couple of additional options are given, from which BRICS (or BICS) is the recommended option. BRICS and BICS are similar models, with the difference that BRICS has an additional reconstruction function to optimise the algorithm. Both models use the inter-gamma scheme (IGDS) as their basis and switch to GDS when the Courant number gets too high. The idea behind this is that UDS induces artificial diffusion of the free-surface and CDS induces unwanted oscillations. The IGDS uses the same method as GDS, with DDS instead of CDS in the bounded area, the only limitation being the Courant number.

For these simulations it is desired to use a third order discretisation method in the momentum and turbulence, in order to be able to possibly capture the gradient of the vorticity. When using lower order methods this gradient would disappear in the truncation error [15]. The only third-order method available is AVLSMART, which has QUICK at its basis.

QUICK can be seen as a corrected linear interpolation. The correction is made by a term proportional to the upstream-weighted curvature. The interpolation can be summarised in equation 3.19. Also according to Leonard [36], the interpolation in QUICK is a quadratic interpolation, resulting in a third-order truncation error.

$$\Phi_f = \frac{1}{2}(\Phi_U + \Phi_D) - \frac{1}{8}(\Phi_{UU} + \Phi_D - 2\Phi_U) \quad (3.19)$$

If, for example, AVLSMART uses a discretisation scheme it will be difficult to induce the scheme to use QUICK, it could be possible for the BRICS scheme which is controlled by the Courant number. In a discretisation scheme like AVLSMART the determining factor is the amount of convection in the flow; this is difficult to control. One of the few things that might effect the convection is the Courant number. The Courant number affects the amount of flow to pass a cell each timestep; when the Courant number is high this could be seen as a if there is high convection in the flow. Although, this is only a small part which influences the convection. More important are the flow characteristics and the shape of the model, which are difficult to control.

For the discretisation of the free-surface BRICS will be used, mainly because it is a recommended setting of NUMECA. Note: the exact free-surface is not of utmost interest.

AVLSMART will be the discretisation scheme for both the turbulence and the momentum equations. Firstly, and most important, because this could be a third-order scheme and secondly, because it is recommended by NUMECA.

3.2.2. Time and pressure-velocity coupling

The governing equations used in ISIS are inherently time dependent; in order to solve these equations, time is needed to be discretised as well as the spatial domain. The basic idea of time discretisation is to ensure that the variables can be determined at time intervals to get a staggered evolution of the flow in time.

In Nantes and CNRS [43] the time derivatives are evaluated using three-level Euler second-order accurate approximations. In the derivatives the current time, the previous and the anterior to the previous time step are taken into account. Coefficients are used in the time derivative of a variable, these coefficients are obtained from a Taylor series expansion from the current time and depend on the delta of the time steps. The time derivative obtained here will be used in the generic discretised equations for the momentum and the free-surface [43].

In fineMarine [46] the only aspect which can be changed regarding the time discretisation is the size and method. In fineMarine a number of options are given to change the time step during computation. One example is the hyperbolic time step, where the time step can be increased or decreased after a fixed time. The recommended option is to use the uniform time step, with a time step size determined by the reference length and velocity.

The determination of the time step size is dependent on the CFL number, or Courant number, see equation 3.20. This equation shows that the CFL number is a relation of the distance travelled by the fluid to the cell distance. To ensure stability the distance travelled should not exceed the cell size in the same direction. Therefore the CFL number should not exceed a value of one. For calculations in NUMECA, a robust program, the CFL number could increase to around 10 without stability issues [46].

$$CFL = \frac{|u|\Delta t}{\Delta h} \quad (3.20)$$

In equation 3.20 the $|u|$ represents the absolute flow velocity, Δt is the time step and Δh is the grid size in the flow direction.

The pressure-velocity coupling in ISIS is constructed on the integrated continuity equations and is based on the SIMPLE algorithm of Rhie and Chow [1983, cited from [43]]. Certain points in the algorithm are given some additional attention. First, the formulation of density discontinuities, or discontinuities in the pressure gradient; for the latter the pressure equation is based on $\frac{\nabla p}{\rho}$. Secondly, the (pseudo)time derivatives are interpolated in such a way, that when a steady solution is expected the pressure formulation is independent of (pseudo)time.

In fineMarine two types of pressure solvers can be selected. One is the basic solver (PCGSTAB_MB), the second option is to use BoomerAMG, which uses the algebraic multi grid method to solve the pressure. The latter uses different grid sizes to speed up the calculations; the solver switches to a coarser grid to find solutions and will change back to the original grid size using the values found in the coarse mesh. ISIS uses the dynamic switch solver as default setting, which uses the PCGSTAB_MB to find a solution first. If this solution is not found after 30 non-linear iterations it switches to BoomerAMG to see if the process speeds up. If this is not the case it switches back to PCGSTAB_MB [46].

3.2.3. Algorithm

An algorithm is used in ISIS to find the correct flow quantities each time step. The simulation and algorithm start with initializing the flow quantities at $t = 0$. The next step is to define a new time step: $t = t + \Delta t$. From this last step onwards the process is repeated at every time step. The procedure continues with the updated flow quantities of the previous time step. The iteration in each time step is summarized in NUM [46]. The enumeration from Nantes and CNRS [43] is adapted to include the theory discussed and will start from defining the new time step.

1. Create a new time step with $t = t + \Delta t$
2. Start iterative procedure flow quantities from the previous iteration
3. If needed, compute the phase concentration for each fluid and update fluid properties
4. If needed, compute turbulent quantities
5. Solve momentum equations to obtain new velocities
6. Solve pressure equation to obtain a new pressure field
7. Update the velocities face fluxes and correct the velocity components with the new pressure field
8. When the non-linear residual are to high, go to step 2
9. Go to step 1 and update the time

As can be seen above, ISIS uses a non-linear iteration inside the time step to iterate through the equations to get a more converged flow quantity. This ensures that the evolution of the simulations is close to physical.

Within ISIS there are also a number of additional parameters, as for example relaxation methods or options to change the discretisation of the governing equations and methods to speed up the calculations. These will not be changed during the simulations, information on these subjects can be found in the documentation of NUMECA [46] and Nantes and CNRS [43].

3.3. Turbulence modelling

When the Navier-Stokes equations are averaged (the process for the governing equations for the RANS methods) the Reynolds stress tensor becomes an unsteady term in the equation. This is explained in Appendix A. The Reynolds stress tensor needs to be modelled to solve the RANS equations and for this purpose turbulence models are created. In this section, the models are going to be discussed, which could be useful for the CFD simulations.

3.3.1. SST-Menter

This turbulence model is part of the two equation models. It uses the Boussinesq assumption (see Appendix A) as the basis of the model [34].

The model combines the $k - \omega$ and $k - \epsilon$ model. The $k - \omega$ model is found to be a robust and suitable model for near wall flow and the $k - \epsilon$ model for the outer boundary layer flow. When these are combined, it will lead to a more suitable turbulence model.

In order to blend the two models, the $k - \epsilon$ model is transformed to a $k - \omega$ formulation. This is done by using a function F_1 to blend the two models; in this blending the following formula is used:

$$\phi = F_1\phi_1 + (1 - F_1)\phi_2 \quad (3.21)$$

In this formula ϕ_1 are the original coefficients of the $k - \omega$ model and ϕ_2 are the transformed coefficients of the $k - \omega$ model.

Besides this blending, the SST-Menter model modifies the eddy viscosity to improve prediction of separated flows due to adverse pressure gradients [43],[40].

The problem with these two equations models, according Nantes and CNRS [43], is that they underestimate the retardation and separation of the boundary layer due to adverse pressure gradients. This leads to too optimistic performance of the turbulent flow around smooth bodies, as the models do not account for important effects of the transport of turbulent stresses. This problem will not be an issue with the use of algebraic models. However, Nantes and CNRS [43] used an additional blending function to improve the transport of turbulent stresses. Also, Nantes and CNRS [43] state that in 3D flow the SST model is not always superior to the BSL model ($k - \omega$ model). A final remark on these models: Nantes and CNRS [43] state that with a computation of a wing-body junction the $k - \omega$ and $k - \epsilon$ were unable to predict the intensity of the horse-shoe vortex.

Another comment on the SST-menter model comes from Jongen and Gatski [28], firstly they state that the popularity of the two equations models (the SST-menter model is part of this group) comes from their simplicity. But they also state that these models "have the deficiency of being based on a Boussinesq isotropic eddy-viscosity concept." The final statement Jongen and Gatski [28] make is the following: "These models lack the universality required for the calculation of complex flows, and this is due to inadequate representation of the significant physical processes governing the Reynolds stress tensor."

3.3.2. EASM

The EASM, Explicit Algebraic Stress Model, is part of the algebraic stress models (ASM) and is developed from the six differential stress models of the Reynolds stress. The ASM results from the differential equations, according to Jongen and Gatski [28], by approximating the convective and diffusive transport of the Reynolds stresses. This results in the differential equations of the Reynolds stress becoming algebraic and thus form a set of six algebraic equations [28].

In Pope [48] the following equation of the Reynolds stress can be found:

$$\mathcal{D}_{ij} \equiv \frac{D\langle u_i u_j \rangle}{Dt} - \frac{\partial}{\partial x_k} \left(\frac{C_s k}{\epsilon} \langle u_i u_j \rangle \frac{\partial}{\partial x_k} \langle u_i u_j \rangle \right) \quad (3.22)$$

$$= \mathcal{P}_{ij} + \mathcal{R}_{ij} - \frac{2}{3} \epsilon \delta_{ij} \quad (3.23)$$

Where the \mathcal{P}_{ij} is the rate production of Reynolds stress, which contains the derivative of the velocity. \mathcal{R}_{ij} is the pressure-rate-of-strain tensor and ϵ is the rate of dissipation of turbulent kinetic energy. The \mathcal{D}_{ij} combines the effect of turbulent transport and viscous diffusion and is modelled in ISIS by the Daly and Harlow model, according to Nantes and CNRS [43]. The pressure-rate-of-strain is modelled in ISIS by a quasi linear SSG model [43]. The above described approximations, lead to a set of algebraic functions for the Reynolds stress equations. The derivation continues with defining the Reynolds stress anisotropy tensor.

The implementation of an EASM model requires two transport equations to be solved to find the turbulent velocity and length scales. Nantes and CNRS [43] uses the two equation model $k - \omega$ for this. Secondly, two modifications are made to the original EASM model by Nantes and CNRS [43]. The turbulent eddy viscosity definition is altered and "the contribution of the non-linear part of the Reynolds stress to turbulence production is taken into account in three-dimensional flow computation.", Nantes and CNRS [43].

For a complete derivation and implementation in ISIS Nantes and CNRS [43] should be consulted. Nantes and CNRS [43] refers to, among others, Jongen and Gatski [28], Gatski and Speziale [14], Launder and Sandham [35].

In the above one can see that the ASM models of EASM preserves the anisotropy of the transport of Reynolds stress and give closure to some of the equations the Reynolds stress models; this makes the EASM model more

suitable for modelling complex flows. This is supported by Deng et al. [6], who state that EASM performs better than the SST-model in ship resistance cases and also the aft-body vortex is better predicted by the EASM model.

One of the drawbacks of this model is the increased computation time, compared to the two equation models. Also, the EASM model could underperform in flow dominated by convex curvature or with rapid transients [43], [28], [18].

In NUMECA [46] the option is given to use rotation correction for the EASM turbulence model. This function is discussed in Deng and Visonneau [7]. The rotation correction could improve the prediction, because the EASM model (among others) has difficulty in modelling swirling motion. The method proposed to solve this is based on the invariants of vorticity, strain rate tensor and the Richardson number.

From the results discussed in Deng and Visonneau [7] it appears that turbulence models without rotation correction, even the Reynolds-stress models, have indeed difficulty in predicting the swirling motion in the test cases. The model with rotation correction, for this test case the Launder-Sharma model, seems to perform only slightly better, than all the other models without rotation correction.

It is unclear if the EASM model will be improved by the rotation correction. It might be possible, as NUMECA [46] has implemented it in their model.

3.3.3. DES-SST

The final turbulence model discussed here and an option to use in this study, is the Detached Eddy Simulations (DES) coupled with the SST-*menter* model (DES-SST). The idea behind this turbulence model is to reduce the computation time of a Large Eddy Simulation (LES) method, by using a two RANS model near the wall [18], [43].

In LES methods the large scale flow rotations (eddies) are simulated, while the smaller eddies are modelled. This requires specific demand for the grid generation, the grid needs to be able to capture the smallest simulated eddies. Using this method in the entire domain leads to long calculations and possibly difficulties around complex bodies. The possible issues of LES around the body are solved in DES by using a RANS turbulence model around the model, it does not require a small grid size and uses less time to resolve the turbulent boundary layer [18], [46].

The modification of the DES model in the SST model can be found in the dissipation term of the *k*-transport equation. In this equation an extra term is added, F_{DES} , see equation 3.24. This F_{DES} is a function of the grid spacing, turbulent length scale and a blending function [43].

$$\rho \varepsilon = \beta^* \rho K \omega F_{DES} \quad (3.24)$$

Overall DES delivers improved results in comparison with 3D RANS and good results for large separation regions. Furthermore, it can be applied for several engineering problems, due to the way it is constructed [18], [51].

A large issue in the Detached Eddy Simulations is the coupling between the RANS model and the LES. The first main issue on this subject is that both models approach the simulation of turbulence in a different way. RANS models its turbulence and LES more or less tries to simulate it. This could lead to discrepancies in the transition, possibly resulting in a sharp transition between the two models. In addition to this problem, the grid requirements for the models are also different and could lead to problems at the couple interfaces of the models. The final issue for DES is that it also has problems with grid convergence studies [18], [51].

In short, the main issues with DES are found in the wall region and the coupling of this wall region to the outer region.

3.3.4. Concluding

To conclude this section on turbulence models, of the models discussed here the EASM turbulence model will be used without the rotation correction for these simulations. Hereto are a couple of reasons:

Section 3.3.1 and 3.3.2 show that isotropy of the Reynolds stress is a problem with two-equation models. This could lead to inaccuracies in the flow as it is expected that the flow field around the hull is complex. Is it desirable to use a different model than the two-equation models.

Detached Eddy Simulations could be an interesting option to be used as turbulence model, mainly because of its ability to capture vortex structures. Although, in this simulation it is expected that the flow separation is limited and that the vortex structure originating from the boundary layer could be of importance. It is decided not to use DES for these simulations, because of the issues with the coupling of the models around the boundary layer edge, as mentioned in section 3.3.3. Also, DES simulation will take more time than the EASM simulations.

The rotation correction will not be used in these simulations. First, and foremost, because it is unclear if the function of Deng and Visonneau [7] improves the rotation in the flow, even though it is implemented in NUMECA [46]. Secondly, the limitations of the EASM model are understood, while effect of this rotation correction on the flow is still unclear.

3.4. Overset

In fineMarine and Hexpress the option to use an overset method is implemented. The idea behind this method is to use different domains and meshes for objects that require large motions, including large motions in domains with a default motion. This is a good tool for ships in waves or ships within manoeuvring simulations. However, it could also be used for rudders, these often have large angles of rotation. A standard mesh of NUMECA can handle deformations due to rudder angles of around 3° [22].

The overset grid method requires a connection between the different grids. The connection made by interpolation of the overlapping cells and results in three types of cells in the domain: active, blanked and interpolated. Blanked cells fall outside of the usable domain and are thus neglected. A difficulty in using overset is determining the value in the interpolated cells. Nantes and CNRS [43] uses a least squared approach (based on a linear polynomial) for higher interpolation; this ensures second order accuracy, but suffers from stability problems. The second interpolation method is a weighted approach. Both methods use an interpolation stencil, selecting the appropriate cells for interpolation based on the donor cell [43].

It seems that overset is a useful function for these kinds of test cases. Although, because of the interpolation, which could introduce inaccuracies in an important location and the difficulty to get it working, it was decided to not use this function.

3.5. Boundary conditions

NUMECA [46] has implemented a number of boundary conditions. The conditions implemented are the most used boundary conditions in numerical simulations, ranging from 'slip walls' to 'wall-function' for solid boundaries, mirror conditions (e.g. for exterior boundaries) or variation in in- and outflow options.

This section discusses only the relevant options for this study. In the simulations only two boundary conditions are used: 'solid walls' and 'exterior boundaries', so the conditions for these boundaries are discussed in this section.

3.5.1. Exterior boundaries

For the exterior boundaries, the outside of the box, there are a number of options in NUMECA [46]:

1. Far field
2. Prescribed pressure (Dirichlet condition)
3. Zero pressure gradient (Neumann condition)
4. Wave generator

The last one is of no importance, because the simulation does not contain waves.

The prescribed pressure method, as the name already suggests, sets the pressure of a particular plane to a predetermined value. NUMECA [46] states that there are two options available: a frozen and an updated hydrostatic pressure. The latter option should be used for the top and bottom in the domain for a 3D multi-fluid simulation. The other option could be of use in single fluid simulations.

The zero pressure gradient sets the pressure gradient on the boundary to zero. When the pressures and velocities at a certain outflow are unknown, this is the preferred method to use.

In the simulations the top and bottom boundaries of the domain have a prescribed hydrostatic pressure. The rest of the domain boundaries are far field.

As the domain will move as a whole in the simulations the exterior boundaries could act as an inflow or outflow. In these cases NUMECA [46] will apply a Dirichlet or Neumann condition on those planes, depending on the local flow characteristics.

3.5.2. Solid boundaries

The solid boundaries have three standard options in NUMECA [46]: Slip, No-slip and wall-functions. The first is suitable for non-viscous simulations and therefore only usable for the surfaces above the water.

The other two options both assume zero velocities near the wall, where the velocity in z -direction is already zero because of the no-penetration condition. The difference between the two is found in the modelling of the area with a distance of roughly $y^+ = 30$, i.e. the viscous layer and/or the buffer layer. The wall-function models this region, whereas the no-slip condition needs to calculate it.

The wall-function ensures it is possible to place the first grid node or cell boundary at a distance of $y^+ = 30$, in the fully turbulent overlap region. From this position, the local flow quantities will be used to calculate flow quantities in the viscous layer at the first cell. The wall-functions use the log-law relations together with the k , ϵ and ω parameters [56],[48], [4].

The advantage of using these wall-functions is that for turbulent flows the mesh size is reduced and the solver does not have to process the complex flow near the wall. For general CFD simulations, e.g. standard resistance calculations, it is the preferred method. One of the drawbacks of using wall-functions is that the function does not work for separated flow, because of the logarithmic properties of the wall function. For these kinds of flows NUMECA [46] advises to use the standard no-slip condition and the first node distance at $Y^+ < 1$ [56],[48], [4], [46].

For these simulations it is chosen to use wall-functions, where possible, i.e. on the hull surface and keel. As the stall angle of the rudder is of interest, the wall-function cannot be applied; here, the no-slip condition will be used.

3.6. Simulation set-up

This section discusses the simulation set-up. It will include the following topics: the model, grid generation and the choices regarding the set-up of the simulation.

3.6.1. Model

The model (TUD366) is a parametric variation on an America's Cup Competition (IACC) rule (TUD329) made in 1992. These models were used at the TU Delft towing tank for keel influence on sailing yachts. Chapter 4 describes the towing tank set-up in more detail.

One of the difficulties in using an old model for CFD simulations is the lack of digital models. Apart from the lack of a digital model, this model also was a parametric variation drawn by computer in the nineties of the last century and lacked a proper lines plan.

Furthermore, there were doubts about the model's condition. The model is made of wood via the plank-on-frame construction method and as the model was stored in the towing tank for circa 20 years, it could have been warped. Also, building a model via the construction method of plank-on-frame introduces more uncertainties than present day methods. There are a number of steps in the plank-on-frame method where symmetry could be an issue.

In order to make a correct comparison with the least amount of geometric uncertainty, it was decided to scan the model. This is done using an Optotrak Certus camera [21]. The output of this scan was a point cloud, which is then traced in MAXsurf [2]. This introduces some uncertainties: the tracing in MAXsurf is done by hand and only for one side of the hull, because of time considerations. Nevertheless, it is believed to be the most sound method available at the moment.

The deviation of the scan to the model can be found in table 3.2. This deviation is found by using the Rhinoceros function point deviation, which gives statistics on the difference of a point cloud to line segments or a surface [50].

The table shows that the differences between the physical model and the numerical model are small, a mean difference of 1.3 millimetres. Also, the asymmetry of the physical model is small, in the order of a millimetre. Resulting in a modelling error of around 0.009 millimetres. This error will be used in the comparison of the numerical and physical experiments, see chapter 5.

Table 3.2: The difference between the scanned model and the current numerical model. In this analysis the scanned model's point cloud is compared to the traced model. The portside of the scanned model is used to trace the numerical model.

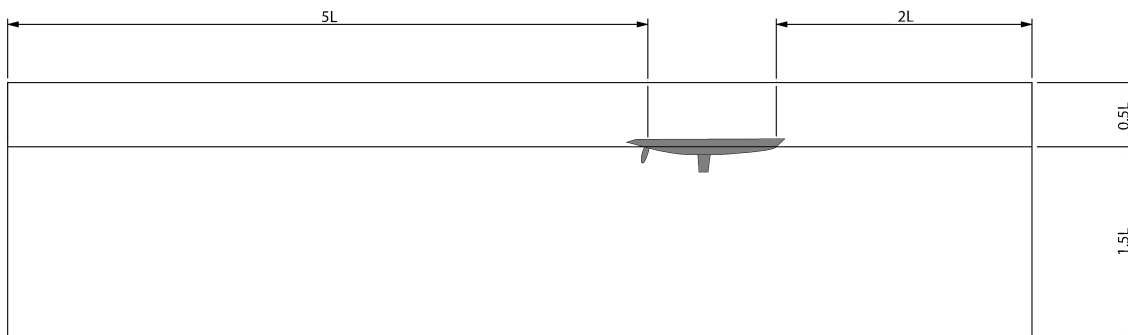
	Mean [mm]	Standard deviation [mm]	Standard error [mm]
Starboard	2.06	1.08	0.015
Port side	1.07	0.79	0.007
Total model	1.26	0.99	0.009

3.6.2. Domain

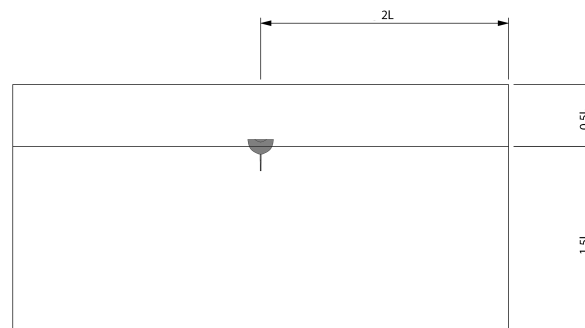
The size of the domain is based on recommendation from NUMECA [46] and the requirement of an orthogonal mesh. In figures 3.7a and 3.7b the dimensions of the domain are shown.

The domain should be large enough, so no interference occurs between the boundary and the flow around the model. However, when the domain is too large the mesh will become also larger than necessary. The distance from the model to the boundary is especially important in the wake, as it is unacceptable when the wave system is reflected back to close to the model. For the inflow, as long as there is a uniform inflow, the dimensions of the boundary are less important. The same arguments apply to the vertical dimensions of the domain. Depth is more important than height, because the air above the waterline is hardly contributing to the resistance and flow (of water) around the model.

For these simulations the domain in front of the model is two waterline lengths in x -direction, whereas the distance behind the model is $5L_{WL}$. The half width and the height, in total, are again $2L_{WL}$. The height is divided in $0.5L_{WL}$ above the waterline and $1.5L_{WL}$ below, see figures 3.7a and 3.7b.



(a) The domain seen from the side.



(b) The domain seen from the aft ship.

Figure 3.7: The domain for the CFD simulations.

3.6.3. Grid

The grid is an important factor for the accuracy of the results of the simulation. If a grid is not properly constructed the simulations will most likely give inaccurate results. Because the grid is so deciding for the accuracy of the results a grid convergence study is conducted, chapter 5 discusses this study.

The mesh is created in the unstructured mesher of NUMECA; Hexpress. This mesher uses an unstructured hexahedral mesh. In mesh generation it is from utmost importance to create an orthogonal mesh. The way hexpress works is to use an orthogonal initial mesh and a refinement based on splitting those initial cells in four. It is possible to alter this process by using certain settings, which could be useful for, for example the free-surface. After the mesh adaptation, the mesh is snapped to the body and then optimised. The final step in the meshing is the insertion of the viscous layers as discussed in section 3.1 [47].

At the locations where the flow is of particular interest, the mesh needs to be fine enough to be able to capture it, first of all around the body. The appendages and keel section (of the hull) are refined. Furthermore, two boxes are created, one around the model and one between the keel and rudder, the latter being the most refined one. The free-surface is refined over the z -axis. For the free-surface refinement no specific attention was given to ensure a correct refinement of the wave system, because the exact wave geometry is not of interest.

In table 3.3 the refinement and target cell sizes can be found for the fine grid (the middle grid in chapter 5). For a couple of components the precise refinement ratio is important, as for example a fixed number of cells need to be applied in the rudder gap; for others it is more a visual choice. The target cell size is zero for most of the components, because Hexpress will then automatically find the correct cell size, based on the refinement ratio and the initial cell size. This is especially important with grid refinement studies, when geometrically similar grids are necessary, more on this is described in chapter 5.

Table 3.3: The grid refinement and target cell sizes for each component for the fine grid.

	Refinement ratio	Target cell size (x, y, z)
Hull	6	(0, 0, 0)
Bow curve	6	(0, 0, 0)
Aft ship curve	7	(0, 0, 0)
Keel	7	(0, 0, 0)
Keel trailing edge	11	(0, 0, 0)
Keel leading edge	7	(0, 0, 0)
Rudder	8	(0, 0, 0)
Rudder trailing edge	12	(0, 0, 0)
Rudder gap hull	12	(0, 0, 0)
Rudder leading edge	9	(0, 0, 0)
Free surface	8	(1.096, 1.096, 0.0054)
Box 1	4	(0, 0, 0)
Box 2	6	(0, 0, 0)

The viscous layer insertion is connected to the choice of boundary condition, discussed in 3.1. Section 3.1 explains the difference if either no-slip or a wall function are used.

For the rudder it is desirable to have a lift and drag curve which are close to the ones found in the experiments, so the no-slip boundary condition will be used. The other surfaces of the model do not require the same accuracy of results, so in order to optimise the computation time these boundary conditions will be set to wall-function.

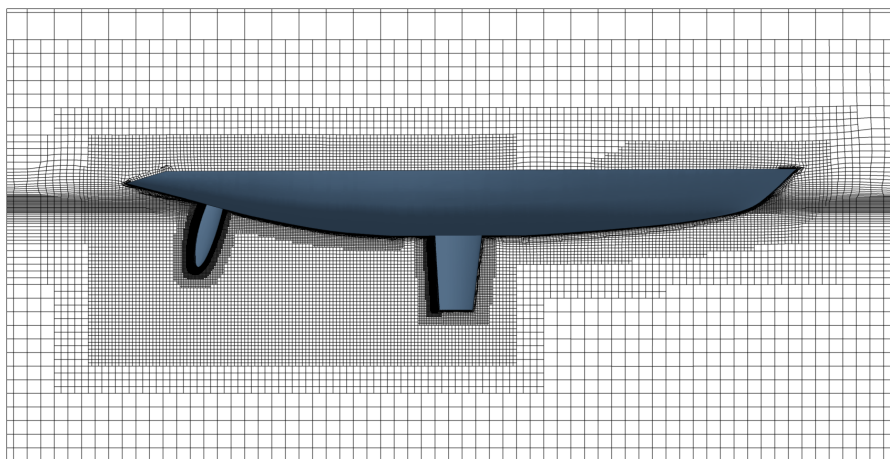
A consequence for the grid is that the rudder requires more viscous layers and a smaller first cell distance in order to resolve the flow accurately. In table 3.4 the y^+ , first cell sizes, number of viscous layers and the inflation factor for each surface can be found.

The choice of a wall distance of $y^+ = 30$ for the hull and keel is advised by NUMECA [46]. The wall distance of $y^+ = 5$ is used to reduce the mesh size and to prevent negative or skewed cells. The location of the first cell size is within the viscous sub-layer and will be appropriate for the simulations.

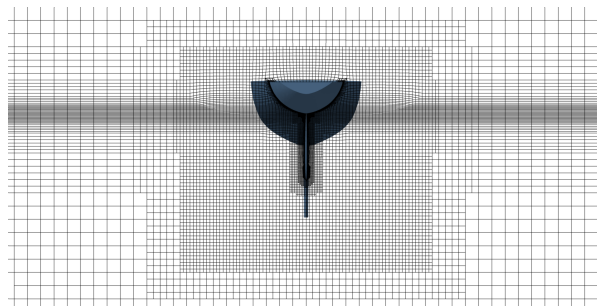
Table 3.4: The viscous layer settings for simulations with a fine grid.

	Determined y^+	First layer distance [m]	Number of layers	Inflation factor
Barehull	30	$4.05 \cdot 10^{-4}$	21	5.1
Keel	30	$3.16 \cdot 10^{-4}$	19	5.5
Rudder	5	$4.8 \cdot 10^{-5}$	26	6.1

In case of using a laminar flow model, the boundary conditions will be set to no-slip, because the wall resolved boundary condition does not apply for laminar boundary layers. The viscous layers are not to be changed, because of the less complex nature of the boundary layer in laminar flow. The mesh around the rudder could be over dimensioned, it is expected that this will only have minimal effect on the computation time.



(a) The grid seen from the starboard side.



(b) The grid seen from aft ship.

Figure 3.8: The grid for the CFD simulations. The grid displayed is the fine grid or middle grid size.

In figure 3.8a and 3.8b the constructed grid is shown for the middle refinement. This grid is used in all the simulations. More on the choice of grid refinement can be found in chapter 5.

The grid complies to the in this section described intentions. The free-surface, appendages and the keel of the hull are refined to satisfaction. The two refinement boxes are easily observed.

However, the grid also shows a couple irregularities:

- Figure 3.8a shows a large hole in the refinement at the deck of the model, this is not an issue.
- The small hole in the refinement near the trailing edge of the keel should have been avoided. However, it is not expected that this irregularity has a significant influence on the flow around the rudder, as no additional flow structures will be made at the location of the irregularity and the refinement of the irregularity is equal to the refinement between the keel and rudder.
- The region between the keel and rudder could have been more refined, this refinement should also have been continued to the side of the rudder. This would have captured the influence of the keel better, see section 5.5.1.

3.7. Numerical results

The final section of this chapter discusses the results of the CFD simulations. Beside the results, this chapter will also present the visualisation methods and type of figures which will be used in the final analysis of the results in chapter 6. In chapter 6 the results of both experiments will be analysed into greater detail, this means that the results discussed and methods discussed here do not contain a comparison between the experiments.

3.7.1. Boundary layer (y^+)

Below in figures 3.10 and 3.11 the values for the y^+ are presented for the case of 3° leeway and 0° rudder angle. With these plots it is possible to check whether the assumptions made for the first layer thicknesses in section 3.6.3 are correct. The variable y^+ is the non-dimensional wall distance. The determination of this distance is described in section 3.1. For the definition of the leeway and rudder angles, see figure 3.9.

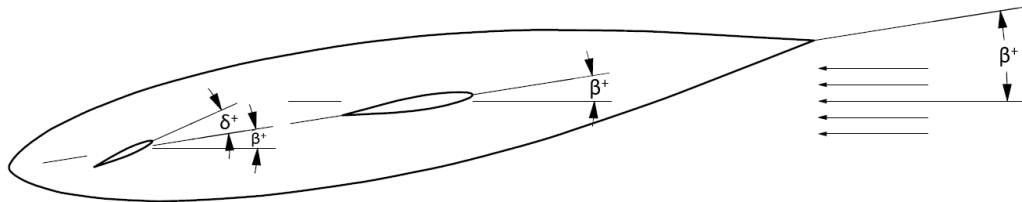


Figure 3.9: The defined positive direction of rotation for different the components in the xy -plane.

As explained in section 3.6.3, the rudder and hull/keel have different boundary conditions. The chosen boundary conditions can be derived from the figures. Namely: the rudder has a y^+ of below 2.5, because of the no-slip boundary condition and the rest of the hull has a y^+ of between 5 and 30, as expected with a wall function boundary.

For a wall resolved boundary condition (i.e. a no-slip boundary condition) the y^+ distance for the first cell should be below five, preferably around one. In this case the rudder has a y^+ below 2.5, so the first wall distance can be assumed to be correct.

When the wall-function boundary condition is used the first wall distance should be around $y^+ = 30$. From the figures can be seen that the large part of the hull and keel have an y^+ between 15 and 20. These values will still lie within the buffer region according to section 3.1. NUMECA [46] is a robust program and is able to accommodate for this smaller y^+ value, even to values of $y^+ = 1$ for the wall-function boundary condition. However, it still could result in a deviation of resistance. According to NUMECA [46] the error of a incorrect first layer distance could be in the range of 3 – 4%.

To conclude, the first layer distance is fine, but could have been optimised for the hull and keel. This would have lead to a better prediction of the drag forces. In addition, a wall resolved boundary condition leads to a more accurate prediction of the boundary layer and the instabilities originating from this layer. With more resources it would have been favourable to have simulations where all boundaries were wall resolved, in order to get a more complete wake prediction.

3.7.2. Pressure over hull surface

The dynamic pressure plots over the hull surface will give an indication of the low and high pressure zones over the hull surface. With a possible indication of separation zones. In figures 3.12 and 3.13 the dynamic pressure over the hull is presented, for the test case of 3° leeway and 10° rudder angle.

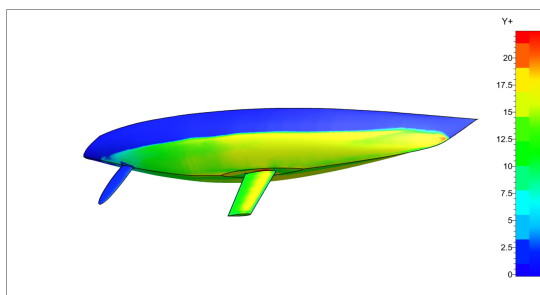


Figure 3.10: The y^+ distribution over the hull, seen from starboard, for $\beta = 3^\circ$ and $\delta = 0^\circ$.

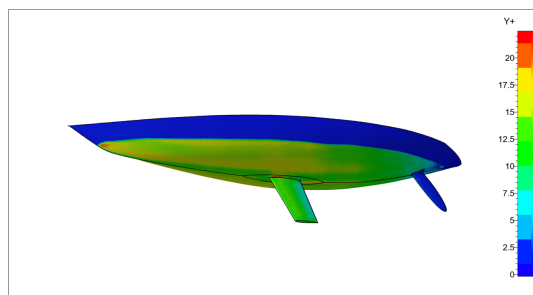


Figure 3.11: The y^+ distribution over the hull, seen from port, for $\beta = 3^\circ$ and $\delta = 0^\circ$.

From experience a low pressure on the port side of the keel and hull and a low pressure on the starboard side of the rudder are expected. Both regions are visible in the figures. Also the pressure from the flow around a body is visible from these figures, this pressure corresponds with the waves generated on the free surface. Note: The hole in the keel indicates a lower pressure than the range.

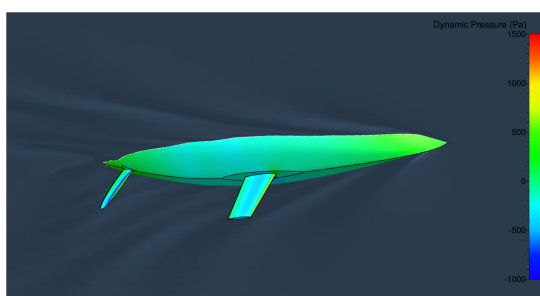


Figure 3.12: The dynamic pressure distribution over the hull, seen from starboard, for $\beta = 3^\circ$ and $\delta = -10^\circ$.

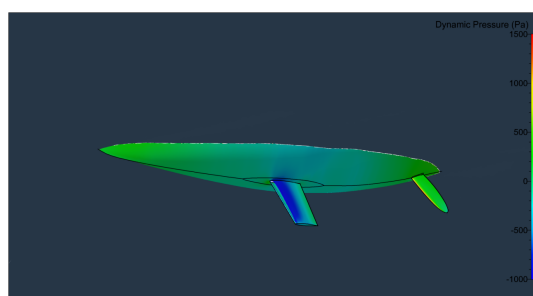


Figure 3.13: The dynamic pressure distribution over the hull, seen from port, for $\beta = 3^\circ$ and $\delta = -10^\circ$.

3.7.3. Vortex identification

Vortex identification is a difficult subject in fluid dynamics. In the course of time quite some studies have been conducted to it. In NUMECA two types of vortex identification are implemented, namely λ_2 and Q -invariant or second invariant. Both belong to the region-based methods and work on finding the locations in the flow where the pressure is the lowest.

There are a number of definitions for vortex structures, for example Hunt et al. [19] states that Eddy zones are zones with strong swirling motions, which can also contain stretching. Outside these zones irrational swirling is excluded. Also, when the pressure in a zone tends to a minimum, a gradient should be present across the streamline [19]. Note, a pressure minimum in the flow does not necessarily mean a vortex centre, as mentioned in Jeong and Hussain [27].

The second invariant method is the second invariant of the ∇u , or Q . According to Jeong and Hussain [27] Q is defined in the following way, see equation 3.25.

$$Q = \frac{1}{2} (|\mathbf{\Omega}|^2 - |\mathbf{S}|^2) \quad (3.25)$$

$$|\mathbf{S}| = \sqrt{\text{tr}(\mathbf{S}\mathbf{S}^t)} \quad (3.26)$$

$$|\mathbf{\Omega}| = \sqrt{\text{tr}(\mathbf{\Omega}\mathbf{\Omega}^t)} \quad (3.27)$$

In these equations the $|\mathbf{S}|$ is the symmetric component and $|\mathbf{\Omega}|$ the asymmetric component of ∇u . The Q represents the equilibrium of the local shear strain and the vorticity. A final aspect of the Q -invariant is that the function vanishes at the wall, because at the wall the magnitude for the shear strain and vorticity are equal. Also, the Q can be interpreted as the source term of the pressure in the Navier-Stokes equations[27].

The second method, the λ_2 , also uses the symmetric and asymmetric components of ∇u . This method uses the symmetric part of the gradient of the Navier-Stokes equation. The viscous and unsteady terms are neglected, from the symmetric part of the gradient, resulting in a sum of the square of the symmetric component $|\mathbf{S}|$ and the asymmetric component $|\mathbf{\Omega}|$. In short, the vortex core is defined as the connected region with two negative eigenvalues. This means that in the vortex core the second eigenvalue of $|\mathbf{S}|^2 + |\mathbf{\Omega}|^2$ is negative [27].

The difference between the two methods is basically the way the eigenvalues are used to determine the location of the vortex core. As explained above, the λ_2 method assesses at which location the $\lambda_2 < 0$ and the Q -invariant uses the sum of the eigenvalues of $-\frac{1}{2} \text{tr}(|\mathbf{S}|^2 + |\mathbf{\Omega}|^2)$, the sum should be negative at a location of a vortex core. The different way of interpretation could lead to different results.

In Jeong and Hussain [27] a comparison is made in order to check their developed λ_2 method. They state that indeed both methods discussed here show similar results for a large amount of test cases. Only for cases where strong external stretching behaviour was present, a difference was found in the results of the two models. From which Jeong and Hussain [27] assumed a incorrect Q -invariant. Although, these statements are made by the developers of the λ_2 and thus could be biased. From their analysis and the way the functions are constructed it is obvious that there is little difference between the two models.

The post processing of the data will be done with the use of λ_2 . This method appears more accurate than the Q -invariant. Jeong and Hussain [27] state that the methods discussed here are only be looking for the vortex core region and will not give a measure of the influence region of the vortex. In order to assess the influence of these vortices, the local pressure, relative velocity and vorticity will be assessed on the same plane as the λ_2 .

An example of the use of the λ_2 criterion for the vortex detection is displayed in figures 3.14 and 3.15, for the case of 3° leeway and 5° rudder angle. In these figures the tip vortices of the keel and rudder are distinguishable and also a vortex originating from the hull. In addition to these vortex structures the figures show also structures near the free-surface, the meaning of these is unclear. Finally, near the appendages, especially near the rudder in figure 3.15. Some kind of sheet vortices seems to originate.

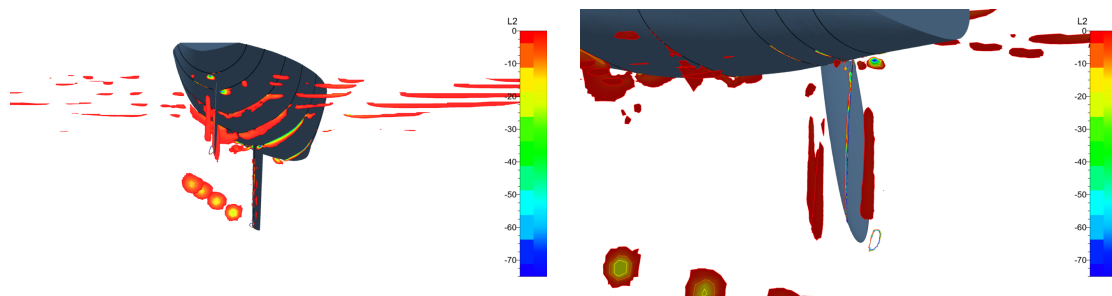


Figure 3.14: The λ_2 as vortex detection for the CFD simulations, for $\beta = 3^\circ$ and $\delta = 5^\circ$.

Figure 3.15: The λ_2 as vortex detection for the CFD simulations, for $\beta = 3^\circ$ and $\delta = 5^\circ$.

In figures 3.16 and 3.17 the dynamic pressure is plotted on the same planes as the λ_2 . From these plots the following aspects are clearly visible: high pressure side of the rudder, the tip vortex of keel and rudder. The influence of the tip vortices on the pressure around the rudder is not detectable in these specific figures.

Figure 3.17 shows a remarkable transition in pressure. Namely, the pressure on the yz -plane downstream from the rudder is significantly higher than the pressure on the low pressure side of the rudder seen on the yz -plane, which intersects the rudder.

The most notable aspect from figure 3.16 is the high pressure found around the rudder region. The magnitude of the pressure here is significantly higher, than in for example the keel region. This corresponds with a low speed, made visible in figures 3.18 and 3.19.

The influence of the keel on the pressures around the rudder seems difficult to detect from these figures.

The vorticity and velocity in x -direction on the yz -planes from the λ_2 are presented in figures 3.20 and 3.21 and figures 3.18 and 3.19, respectively. In both pairs of plots of the vorticity and velocity the tip vortices are clearly visible.

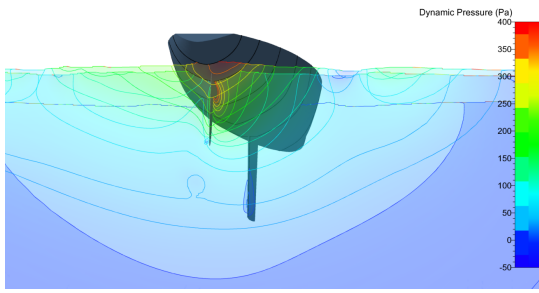


Figure 3.16: The dynamic pressure over yz -planes to visualise the wake, for $\beta = 3^\circ$ and $\delta = 5^\circ$.

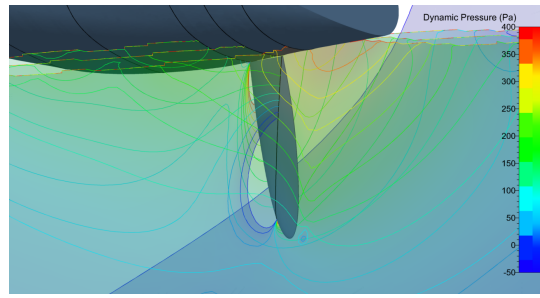


Figure 3.17: The dynamic pressure over yz -planes to visualise the wake, for $\beta = 3^\circ$ and $\delta = 5^\circ$.

Apart from the location of the tip vortices, figures 3.18 and 3.19 show also a kind of vortex sheet originating from the keel. In these figures the influence of the tip vortex and vortex sheet can be seen, which seem to induce an increased velocity on the port side of the hull.

In the same figures, figures 3.18 and 3.19, a large area of reduced flow speed is observed near the rudder and the hull surface. Near the hull on the port side of the rudder the flow almost shows signs of counter flow and separation. This is due to adverse pressure gradients and the natural peak in pressure around the aft ship.

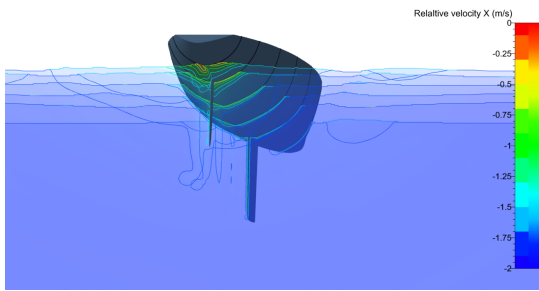


Figure 3.18: The relative velocity in x -direction plotted over yz planes to visualise the wake, for $\beta = 3^\circ$ and $\delta = 5^\circ$.

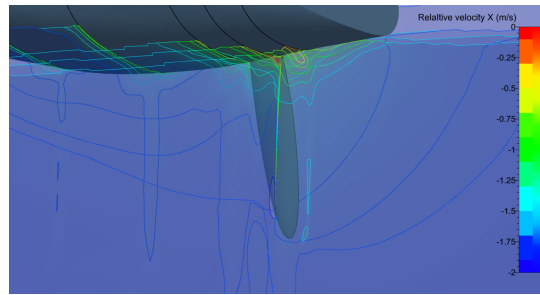


Figure 3.19: The relative velocity in x -direction plotted over yz planes to visualise the wake, for $\beta = 3^\circ$ and $\delta = 5^\circ$.

The normalised vorticity plot in figure 3.20 shows the size of the tip vortex from the keel, as well as the development of this vortex, together with the vortex sheet described in section 2.3. Besides the vortices of the keel, figure 3.20 gives also an estimate for the boundary layer of the hull. In figure 3.21 the tip vortex and the vortex sheet can be identified. Interesting is the strong vorticity just above the tip vortex. It could be an interaction with the vortex sheet of the keel or an indication the rudder near the boundary layer of the hull is significantly less effective. No expected horseshoe vortex is identified from the keel and rudder.

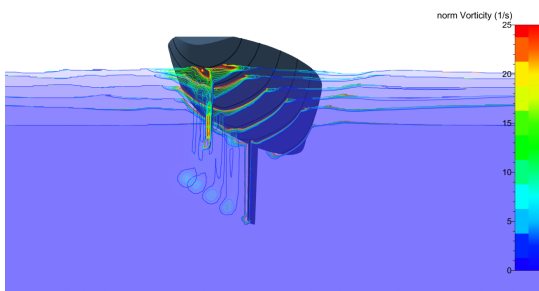


Figure 3.20: The normalised vorticity as vortex detection for the CFD simulations, for $\beta = 3^\circ$ and $\delta = 5^\circ$.

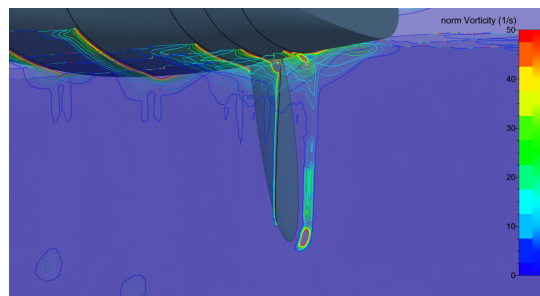


Figure 3.21: The normalised vorticity as vortex detection for the CFD simulations, for $\beta = 3^\circ$ and $\delta = 5^\circ$.

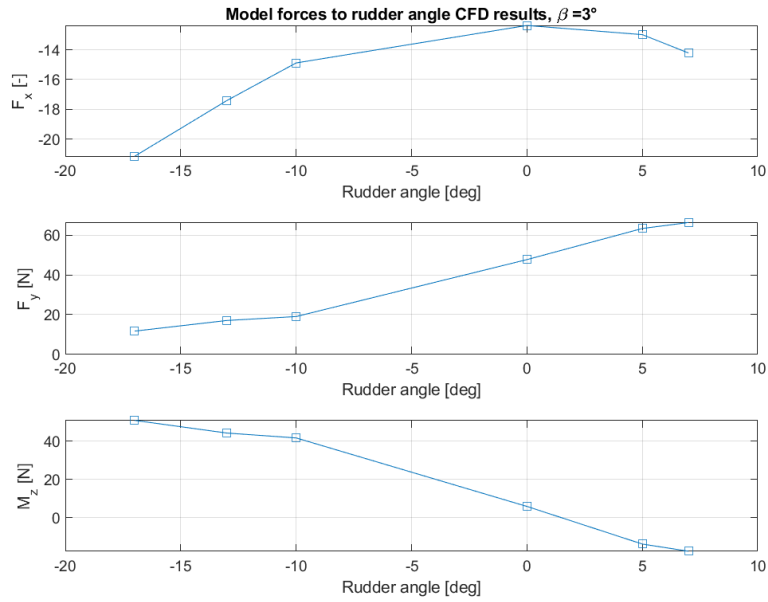
3.7.4. Forces

The goal of the CFD simulations is to be able to "look into the wake". As a measure whether these simulations are correct or contain critical flaws, it is interesting to compare the forces from the CFD simulations and the towing tank tests. In this section only the forces obtained from the CFD simulations are presented. In chapter 6 the forces from the CFD simulations are discussed in more detail and compared to the towing tank results. For both the CFD simulations of the 3° leeway and the 0° without keel. The latter simulations are not presented in this chapter, because these simulations only contain a small amount of rudder angles and would give inconclusive figures.

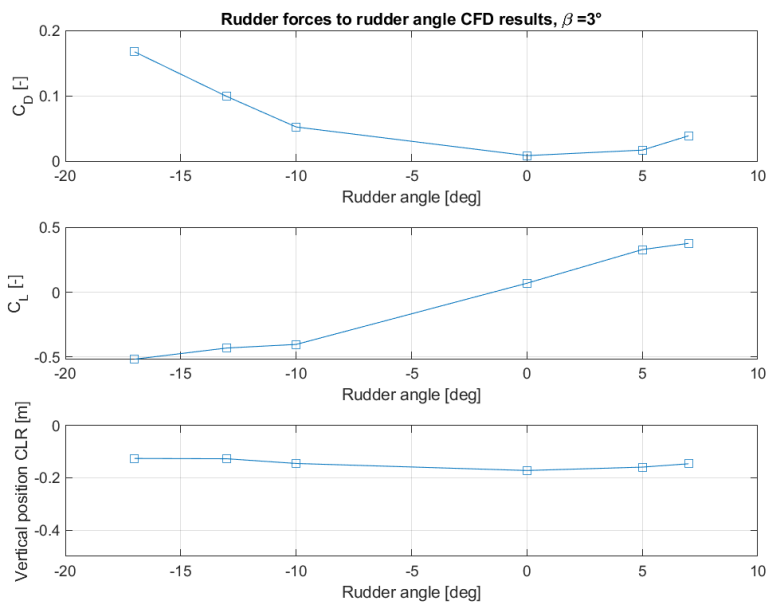
The figures 3.22a and 3.22b show the model forces and the rudder forces obtained from the simulations, for one leeway angle of 3 degrees. From the figures, it seems that a stall behaviour is present at a rudder angle of -10° and 5°, see figure 3.22b. This is concluded from the shape of the drag and lift curves of the rudder. Note, the lift curve only shows a slight change in direction and not the sharp change that one would expect.

Apart from the stall angles figure 3.22b the lift curve also shows the downwash angle, from the shift of the lift curve to the right. This downwash angle should be similar to the downwash angle found from figure D.7, from this latter figure the downwash angle from the experiments is -1.14 degrees for 3° of leeway. For the CFD results the downwash angle for 3° of leeway is -1.64 degrees. Concluding, both angles can be assumed to be comparable.

In the drag curve in figure 3.22b, an asymmetry in the 'resistance bucket' is found, this is due to the oblique in flow of the rudder.



(a) The model forces.



(b) The rudder forces.

Figure 3.22: The forces from the CFD simulations for the leeway angle of 3° .

4

Towing tank experiments

The previous study into the rudder forces on a sailing yacht was conducted at the towing tank of the TU Delft and was part of a larger research into the influence of the rudder on the moments acting on the hull. A new test series is set-up in order to validate the previous outcomes, especially the earlier described phenomena where this research is based on, see chapter 1 and chapter 2. Besides the validation of the previous experiments, the new tests are also an important validation tool for the numerical experiments. The old tests did not provide sufficient information to build a numerical model from, as their exact experimental set-up and findings were not properly documented. The insufficient information of the old tests, set-up and results, also gave complications in the comparison between the newly obtained and the old results, this is further addressed in section 4.4.3. In the new test set-up care is taken to recreate and reuse the previous set-up as much as possible.

4.1. Measurement set-up

In these towing tank tests the TU Delft model 366 is used. This is a parametric variation in beam over draft of a model based on the International America's Cup Competition (IACC) rule (TUD 329) made in 1992. The dimensions of this hull shape can be found in table 4.1 and the lines plan can be seen in figure 4.1, a larger version of the lines plan can be found in Appendix B.

Table 4.1: The dimensions of the bare hull of the model used in the towing tank tests.

		bare hull
Volume	$\nabla_c [m^3]$	0.07
Length	$L [m]$	3.39
Waterline length	$L_{WL} [m]$	2.74
Beam	$B [m]$	1.5
Beam at waterline	$B_{WL} [m]$	0.49
Draft	$T_c [m]$	0.15
Wetted area	$S [m^2]$	1.1
Prismatic coefficient	$C_p [-]$	0.53
LCB from midship	$LCB [\%]$	-5.0

The hull will be fitted with a parent model of a keel variation that has been used, among others, within the Delft Systematic Keel Series [29]. The rudder in principal has the same dimensions as used for the previous test campaign. Although, because the original rudder was skewed, a new one has been constructed based on the dimensions of the old rudder. The dimensions of the appendages can be found in table 4.2.

The hull, keel and rudder all contain dynamometers. The forces on appendages are measured in both two and three degrees of freedom, on the keel (F_x, F_y) and the rudder (F_x, F_y & M_x), respectively. The model as a whole is fitted to the 6-DOF measurement frame of the TU Delft. This set-up is mounted on the carriage using the hexapod, ensuring a fixed position (within the limitations of the hexapod) during the test program. A fixed position will simplify CFD simulations.

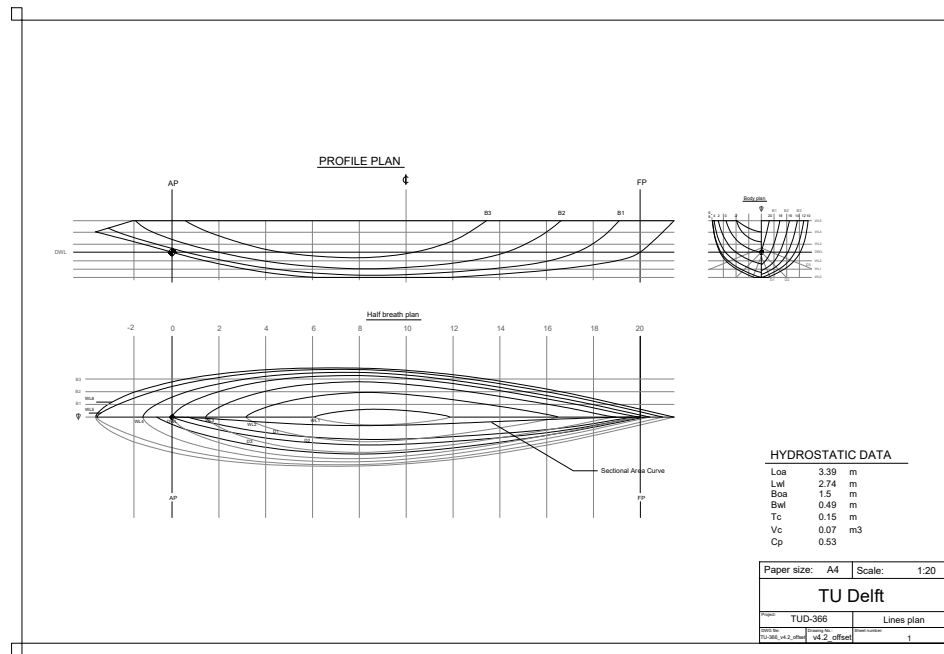


Figure 4.1: The lines plan of the bare hull, a larger version of this figure can be found in Appendix B.

Table 4.2: The dimensions of the appendages used in the towing tank tests

		Keel	Rudder
Span	b [m]	0.374	0.339
Mean chord	\bar{c} [m]	0.231	0.115
Geometric Aspect Ratio	AR [-]	1.623	2.9
Sweepback angle	Λ [°]	9.85	15
Lateral Area	A_{lat} [m ²]	0.086	0.03
Wetted Area	S [m ²]	0.177	0.07
Volume	∇ [m ³]	0.0014	0.00026
Thickness/chord ratio	t/c [-]	0.1	0.12

The rudder is connected to an angle gauge, which has an option to clamp the rudder. The precision of this gauge is in the magnitude of degrees. For alignment purposes, the rudder could be rotated by tenths of degrees. See figure 4.3 for the clamp. Underneath this angle gauge the dynamometers are fitted, to which the rudder stock is connected. No other connections to the hull are used in the measurement set-up for the rudder. A part of the rudder stock is flattened at the location of the screw of the bracket, this screw fixes the rudder stock position.

The keel is connected to the hull with a series of clamps and dynamometers, see figure 4.2. A latex seal is fitted between the keel stock and an inner hull connection, in order to make a watertight connection. This seal has a negligible influence on the force measurements. A final component added to the keel set-up is a silicone seal between the outside hull and the keel, to prevent unwilling tip effects and pressure losses. In order to check whether the seal is working properly, video recordings were made during some tests. These recordings did not show any vibrations or irregularities.

The forces acting on the rudder are measured in three degrees of freedom, the lift and drag forces are measured and additionally the moment around the x axis. The latter is important for determining the height location of the centre of lateral resistance (CLR). The idea is, that when the pressure field around the rudder is influenced by shed vortices of the keel, the location of the centre of lateral resistance will change. There was no need to find the change in CLR for the keel.

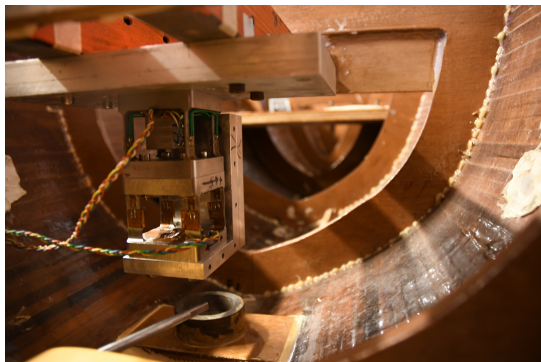


Figure 4.2: The keel connection bracket, dynamometers and the inner hull connection of the latex seal used for the tests; the latex seal is not shown.



Figure 4.3: The rudder angle gauge, dynamometers and clamp used for the tests.

It is expected that the model forces in x and y direction (F_x , F_y) and the moment around z -axis (M_z) are the most appropriate forces to be used in the validations. In order to measure these forces, the model is fitted with the 6-component measurement frame of the TU Delft. This frame will also measure forces and moments in other directions, this will not be an issue.

4.1.1. Turbulent stimulation

For consistency, the turbulence stimulators are positioned at the same locations as used in previous experiments. The first strip is located at the forward perpendicular, the last strip after the shoulder and one strip is located between the first and last. At the location of the last strip, the flow should not be accelerating any more to ensure no reattachment of the flow occurs. The location of the first strip depends on the point at which the flow should become turbulent. At full scale the flow over the hull is first usually laminar and after a certain distance it becomes turbulent, depending on the flow characteristics and the surface roughness [33]. Therefore, the strip is ideally located at a small distance from the bow, to have a short laminar flow before it is induced to be turbulent. At higher towing speeds the model will sink and create a bow wave, this ensures that the first part of the flow around the hull is laminar, when the first strip is located at the forward perpendicular. At low speeds, however, this is not necessarily the case, but then it is questionable how effective the stimulators are in creating turbulence. As the model will be towed at reasonably high speeds during these test series, the first part of the boundary layer is most likely laminar.

The width of the strips on the hull are conform the TU Delft guidelines: 20 millimetres.

The strips on the appendages are located at the same location as used during the experimental campaign of 2005. The single strip on the keel has a width of 10 millimetres and will be located at 6% and 4% of the cord length from the leading edge for the top and bottom part, respectively. The strip on the rudder has half the width of the strips on the keel; 5 millimetres and is located at 6% of the cord length from the leading edge. Due to the shape of the rudder the tip will be completely covered by the strip, this could influence the expected tip vortex. However, it is expected to have a marginal effect on the results. The locations are in the same order of magnitude as I. Abbott [20] mentioned in his book as standard practise of NACA.

Van den Bosch and Pinkster [53] did some research on the types of turbulence stimulators and visualising their effects. They compared studs, sand strips and rotating rods. In this research a number of interesting effects were found.

First of all, the flow along the hull is directed downwards, following the buttock lines; this is a point of attention for placing the stimulators. Furthermore, they found that the studs and sand strips were effective, with the sand strips proving to be better in suppressing separation. Concluding, van den Bosch and Pinkster [53] stated that they found it hard to say whether the created turbulence resembles the natural turbulence, i.e. the velocity profile in the boundary layer and the corresponding frictional resistance.

An important aim of these towing tank tests is to validate the CFD results. Ideally the boundary layer and the turbulent energy of the boundary layer should match between the two experiments. As it is unclear in

what amount the turbulence is created around the model in the experiments and because modelling of the turbulence stimulators is difficult in NUMECA [46], its assumed that in the CFD simulations the turbulence model on a smooth wall will deliver sufficient results, see also the boundary layer of the CFD simulations in figure 4.4. However, further research is necessary on this topic.

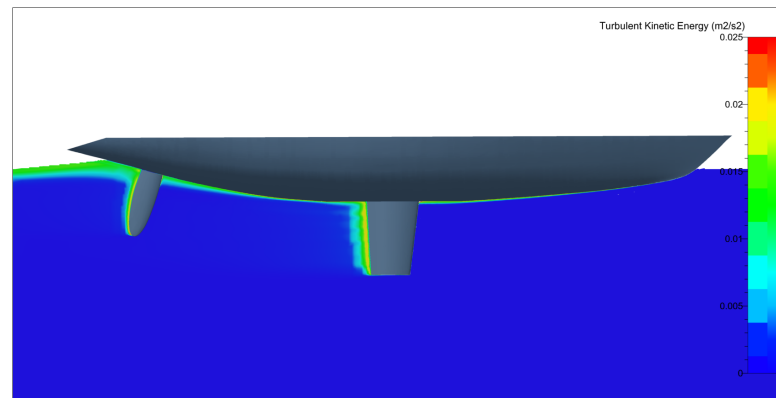


Figure 4.4: The turbulent kinetic energy from the CFD simulations for the validation test case with 3° of leeway and 0° of rudder angle.

4.1.2. Alignment of the components

Before the tests series, care was taken to align the components, i.e. the appendages and the 6-component frame. The 6-component frame was carefully positioned relative to the centreline. The alignment of the appendages was done by using a laser level and a bushing, which fitted neatly in the rudder stock and rudder trunk to ensure alignment in the x, y plane, the laser was used to ensure alignment around the z -axis. In figure 4.5 and figure 4.6 the pictures of the alignment using the laser are presented.

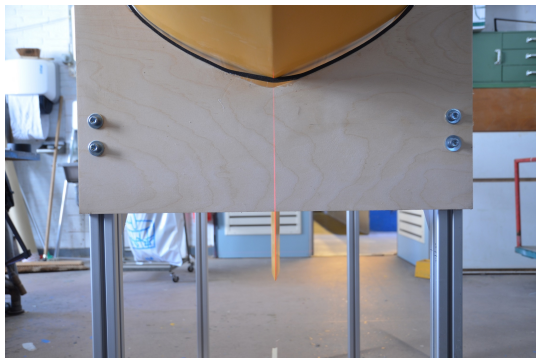


Figure 4.5: The alignment of the keel.

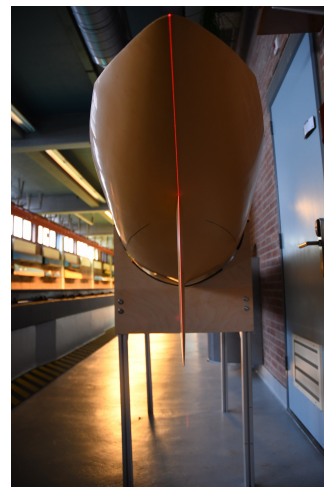


Figure 4.6: The alignment of the rudder

A number of specific measurements were performed to check the alignment during the test series. First the hull was towed without leeway, with the keel attached. To check the alignment of the hull, the side forces of the 6-component frame and the keel are compared for a fair assessment. The side forces measured by the 6-component frame should be close to the measured side forces of the keel, this indicates no leeway angle of the hull. Also, the yaw moment should be close to zero for these tests, because the centre of effort of the keel forces are below the centre of the 6-component frame, no influence is found of the keel on the total yaw moment of the model. After the series the hull was towed without appendages and the above described assumptions appeared to be correct.

The keel alignment is then checked by giving the model some positive and negative leeway. When the keel is correctly aligned, the plot of the side forces versus the leeway should intersect the origin; when a small

deviation is seen, the misalignment of the keel can be found. The found angle was negligible for this test series.

After the alignment of the hull and keel, the rudder is added and aligned following the same procedure as for the hull, i.e. finding the location of the minimum side force and moment. It was not opted to use leeway angles, because the effect of the wake of the hull and keel on the rudder is still unclear. The lack of yaw moment of the model supports the minimum side force and momentum of the rudder. When the rudder is aligned properly a minimum should be found in the yaw moment of the model. As with the keel, the alignment of the rudder can be checked from the results of the lift and drag of the rudder in various figures, for example figure 4.14 or figure 4.15. In both figures the misalignment is concluded from a skewed drag 'bucket' or a lift curve which is not intersecting the origin; the figures show that the misalignment of the rudder is only marginal.

Concluding, all the components are aligned to satisfaction. The results of the alignment tests can be found in table 4.3.

Table 4.3: The final values for the alignment criteria, for the hull and appendages.

Hull		Keel		Rudder	
F_{y_h} [N]	-0.55	F_{y_k} [N]	-0.54	F_{y_r} [N]	0.2
M_{z_h} [Nm]	0.01	ψ [deg]	0.1	M_{x_r} [Nm]	0.1

4.2. Approach

In the previous tests, the model is tested through a series of four leeway angles, eight rudder angles and two heeling angles including the upright condition. For the latest test set-up this program was too comprehensive for the time available. The test matrix has been reduced firstly by using only one keel configuration, with the possibility to test two configurations (with keel and without keel) if time allowed; secondly, by only looking at negative rudder angles. Appendix C displays the initial test matrix for the configuration with keel 1; due to findings, the rudder angle range was expanded to the positive angles.

The trim and sinkage values for the different speeds come from an experiment of Keuning and Binkhorst [29], which are also used by Keuning et al. [32], see appendix C. Please keep in mind that Keuning and Binkhorst [29] use the old convention used in the towing tank, where the positive rotation is upwards. In the recent experiments another convention is used, namely the right hand axis system, see figure 4.7.

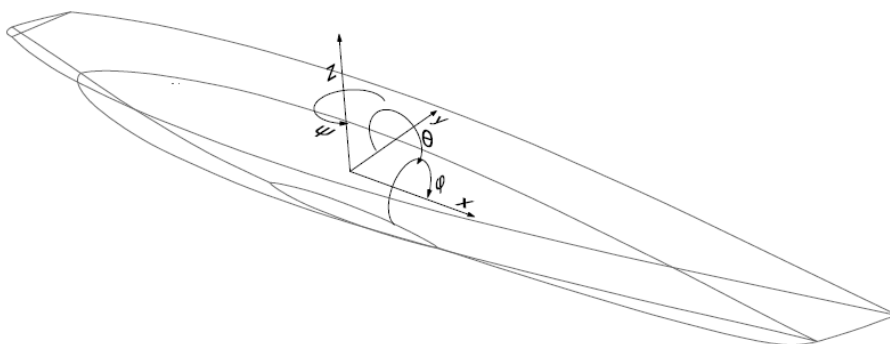


Figure 4.7: The definition of the hull fixed axis system (right hand axis system).

In appendix C the initial test matrix shown. Two resistance curves are constructed between Froude 0.1 and 0.6, for defining the influence of the turbulence stimulators.

The test series will start with leeway angles from -3° to 9° in intervals of 3° . The rudder angles are varied from -5 to -15 degrees with an interval of 2 to 1 degrees, in order to find the angle at which the profile starts

to stall. For validation purposes an additional rudder angle of 5° is added. For each leeway angle two repeated tests will be conducted: one at a rudder angle of 5° , within its normal lift range and one at 15° , to double check the measurements after the expected stall angle.

The above described procedure for finding the rudder's lift and drag curves is repeated for a case without keel. In the previous experiments it is seen that the investigated phenomena also appears in the case without keel, see chapter 2. If this is again the case it would contradict the hypotheses that a vortex from the keel is the cause of the problem.

4.3. Elaboration procedure

This section describes the elaboration of the results from the towing tank experiments. As a guideline the documentation of ITTC [24] is used. First, the filtering of the signal is discussed.

The first oscillation in the measured signal to be discussed is an irregular wave in z -direction. This oscillation comes from a standing wave in the towing tank, with a period of around 60 seconds. In the test series a second oscillation in the measured signal was detected, this was an oscillation in the x -direction with a period of 10 seconds. The latter oscillation was due to interference of the amplifiers used. Both of these oscillations can be filtered with the use of a band pass filter, which will cut off the low and high frequencies in the signals.

The frequencies of the waves found are 0.1 Hz and 0.02 Hz , the latter being the standing wave in the tank. With these frequencies, the lower bound of the filter will be 1 Hz , the upper bound is estimated at 6 Hz . The bounds are not critical in this analysis, because only the mean forces were of interest [1].

The first step according to the ITTC [24] is to correct measurements for the velocity deviation in the runs and temperature. The temperature correction for these tests was so small that the proposed correction procedure would not significantly change the resulting forces, so it was decided to neglect this. In table 5.5 the error of neglecting the temperature correction can be found for three different temperatures. The velocity correction is taken into account in the elaboration.

4.3.1. Turbulence stimulation

The model is equipped with single and double carbonium strips as turbulence stimulators. Before the final measurement data can be used, a correction must be made for the addition of these turbulence stimulators. As mentioned earlier, the strips are added to induce the flow to go from laminar to turbulent, getting more comparable to the viscous and inertial forces for a model at full scale. Not only is the resistance of the hull and appendages affected by the stimulators, the lift is also affected, as can be seen in figure 4.8. According to I. Abbott [20] only the maximum lift is affected by the additional roughness of the strips and only when the roughness is located less than 20% of the cord length from the leading edge. However, figure 4.8 shows that the slope of the lift curve is affected by the stimulators, this effect can also be seen in figure 62 of I. Abbott [20]. As this subject is outside the scope of this research it is not included in the corrections. Only the drag is corrected for the turbulence stimulators, as is the standard practise of the TU Delft towing tank. The influence of turbulence (stimulators) on lift could be an interesting subject for further research.

A velocity range from $Fn = 0.2$ to $Fn = 0.35$ is used to elaborate the correction coefficient. At lower velocities there is a chance of reattachment and at higher velocities the turbulence stimulators are of less importance, as the influence of the strips is largely found in the frictional resistance. The velocity range is kept the same for keel and rudder, in order to eliminate possible errors in the measurements. The selection of the coefficients is based on the standard deviation. Ensured is that the standard deviation of the coefficient data is less than the standard deviation of the repeated measurements. The selected coefficients can be found in the table 4.4 below.

Table 4.4: The coefficients used to correct the turbulence stimulators.

	$C_{f_{strips}}$ [-]
Hull	0.017
Keel	0.030
Rudder	0.027

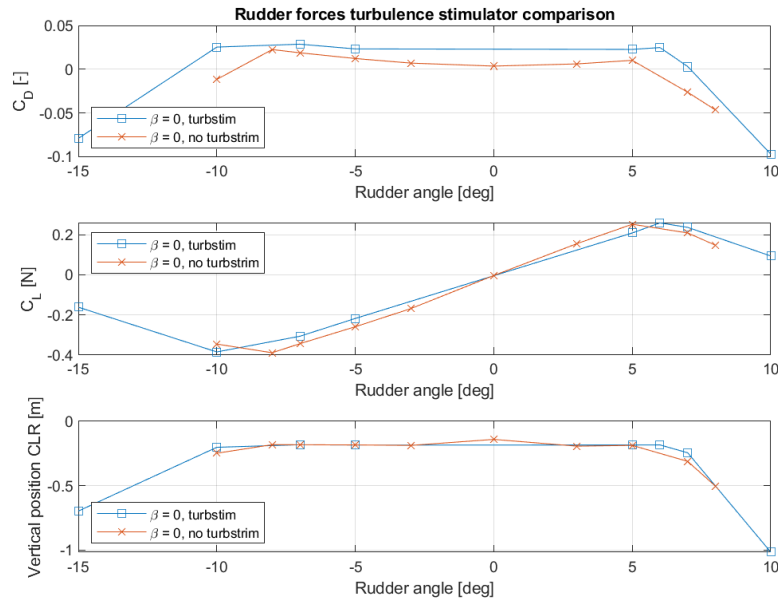


Figure 4.8: A comparison of the rudders' lift and drag tested with and without carboniumstrips.

4.3.2. Rotation of forces

The forces are measured relative to their bodies, however, it is common practise to present the forces in the earth fixed axis system. The forces are thus rotated to the earth fixed coordinate system. The angles which the forces will be rotated around can be found in figure 4.9. This figure shows that the hull (model) and keel forces are rotated by β , the leeway angle. The rudder force has an additional angle δ , rudder angle, which will be added to the leeway angle.

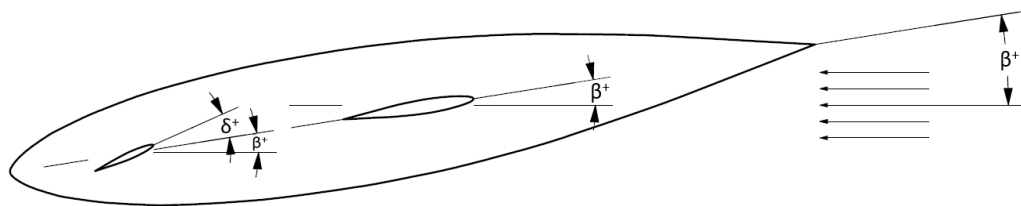


Figure 4.9: The defined positive direction of rotation for the components in xy -plane.

The rotation of the forces to the earth fixed coordinate system, which has its x -axis in the towing direction, means that the forces are now relative to the undisturbed incoming flow. Also, the rotation allows the forces of the appendages to be expressed in lift and drag, the drag being positive in flow direction. As can be seen in figure 4.14, the lift curves of the rudder are still shifted right and left, depending on the leeway angle. This is due to the downwash of the keel. The angle at which the flow reaches the rudder is equal to the shift of the lift curve: the downwash angle. This angle can be found in figure D.7. In order to make the check for symmetry in the rudders' lift and drag curve easier, the curves are also corrected for the downwash angle, thus the flow on the rudder is the local incoming flow, see figure 4.17.

4.4. Results

The focus of this research is on the rudder forces, but some other aspects will also be highlighted, like the hull and keel forces. This section will compare the results to previous research. The graphs referred to in this section can also be found in Appendix D, where nearly all of the experimental results is displayed. Note; all the plotted forces in this section are in the earth fixed coordinate system, unless mentioned otherwise.

In chapter 6 the conclusions of this section will be explained in more detail and compared to the numerical results.

4.4.1. Hull and keel forces

The results presented here confirm that the towing tank tests were executed with little errors and the graphs in this subsection also provide an estimate of the accuracy of the alignment and measurements.

In figure 4.10 the resistance curves for the model, keel and rudder are plotted. These measurements are conducted to determine the influence of the turbulence stimulators on the resistance. The results displayed here are corrected for this additional resistance. The figure shows that the resistance for all three components behaves as expected. Due to a small number of measurements some resistance characteristics, like humps and hollows, cannot be detected.

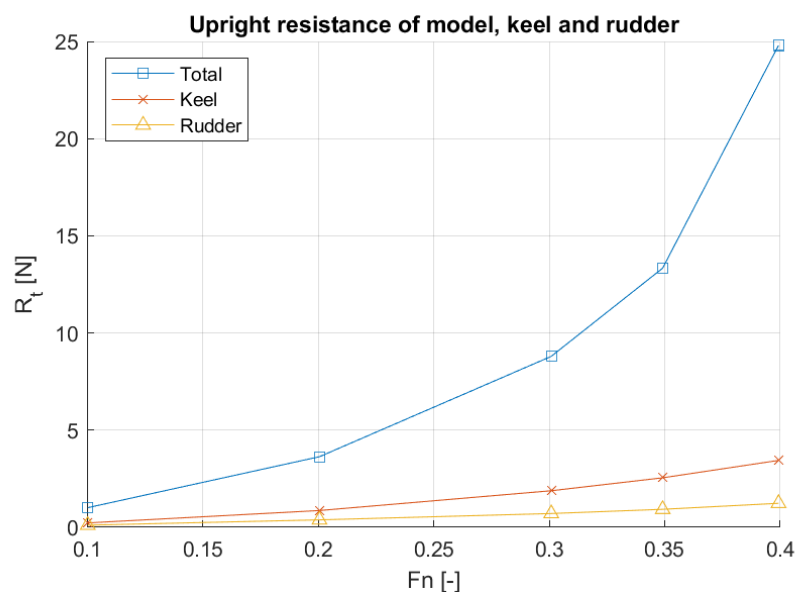


Figure 4.10: The resistance curve for the model, keel and rudder measured at 5 different speeds.

The drag force, side force and yaw moment of the model are plotted against the rudder angle in figure 4.11. As can be seen that all variables are influenced by the force of the rudder. The results presented in this figure are like they were expected. The resistance increases with increasing rudder angles, with a minimum force around the 2° . The side force and moment around the z -axis are both positive for positive rudder angles.

The influence of the rudder on the yaw moment is displayed in figure 4.12. The forces without the influence of the rudder should be constant for a constant yaw angle, however, this is not the case. When the rudder stalls (see figure 4.14) a sharp increase is seen in the moment curves without rudder influence. It could indicate an error in the measurements of the rudder.

The lift and drag forces on the keel are as expected; this is shown in figure 4.13, where the lift and drag coefficients of the keel are plotted against the leeway angle. For the drag coefficient the typical resistance 'bucket' is seen, common for the resistance of airfoils. The lift curve is linear relative to its angle of attack and no stall behaviour is shown.

Only two irregularities are found in these results for the keel, both have to do with the alignment of the keel. The most difficult part of the installation of the keel was to get the correct rotation of the keel around

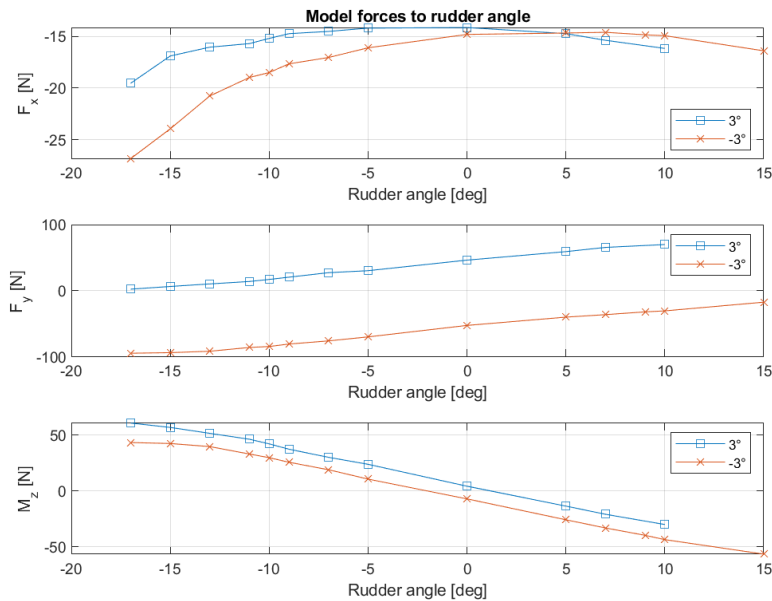


Figure 4.11: The drag force, side force and yaw moment of the test case with 3° and -3° yaw angle.

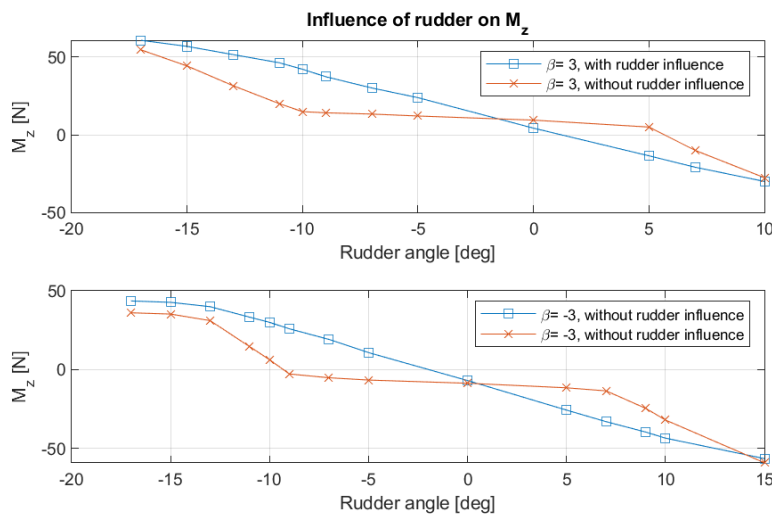


Figure 4.12: The yaw moment with and without the rudder influence on the moment for the test case with 3° and -3° yaw angle.

its z -axis. The made error can be found in both plots, namely: the bucket is skewed anticlockwise and the lift curve does not intersect the origin exactly. Both indicate to an error smaller than one degree, during the tests it was decided that there was no time available to adjust this angle.

4.4.2. Rudder forces

The results which are presented in this subsection were the main focus of the experiments and are of great importance for the research. In the experiments, as can be read in section 4.2, the first intention was to focus around the negative rudder angles. During the experiments it appeared that a complete rudder sweep was necessary for a number of leeway angles. Some more details can be found in section 4.2.

The first graph, see figure 4.14, presented in this section will be the rudders' lift, drag curve and the distance of the CLR to the hull for 3° and -3° .

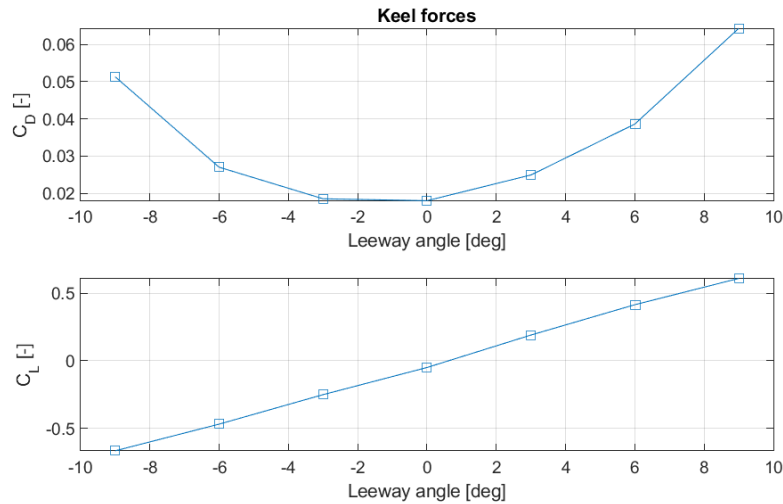


Figure 4.13: The lift and drag of the keel in earth fixed coordinate system.

The first thing to be noticed from figure 4.14 is the negative resistance coefficient (C_D) in both graphs. As described in 4.3, the forces plotted in these figures are relative to the undisturbed incoming flow, i.e. earth fixed coordinate system.

Remarkable is that the resistance flips right after the rudder stalls and that this stalling happens at a reasonably low rudder angle, or low angle of attack. The lift and drag plotted to the angle of attack is presented in figure 4.17.

In addition, the CLR of the rudder also shows some unexpected behaviour. When the rudder stalls, the distance from the CLR to the hull increases. It could be that a vortex close to the hull or a large influence of the wave system of the model is the cause of this strange behaviour. In chapter 6 the conclusions will be discussed in further detail.

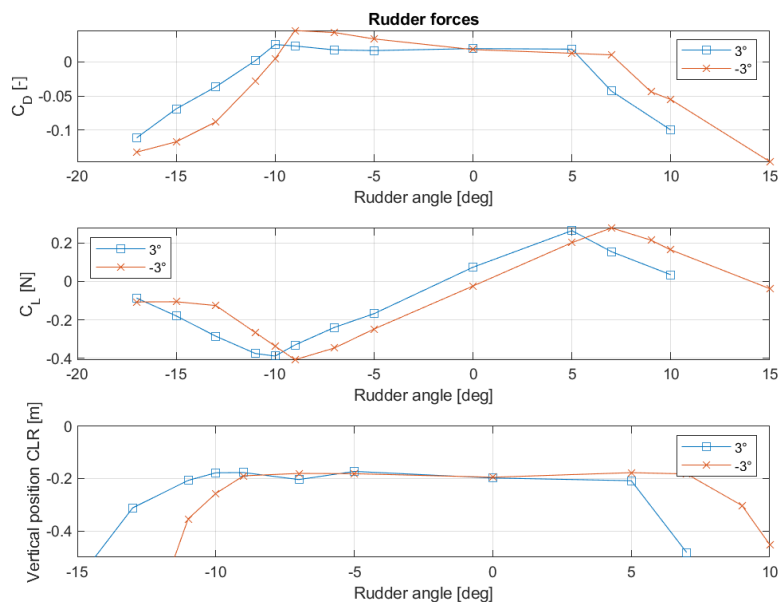


Figure 4.14: The rudder lift and drag forces on the reference earth coordinate system, together with the distance from the hull to the CLR of the rudder, for a leeway angle of 3° and -3° of leeway.

Figures 4.15 and 4.16 indicate that the effects found in figure 4.14 are not accidental errors. Also, the figures 4.15 and 4.16, which show the rudder forces measured without keel influence, give strong indications that the possible physical effects do not originate from the keel, as was expected earlier, but are probably originating from another source.

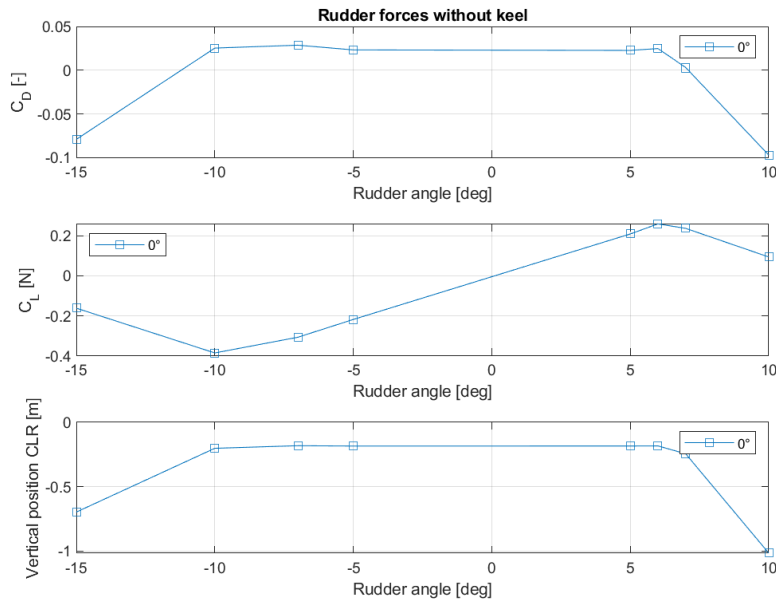


Figure 4.15: The rudder lift and drag forces on the reference earth axis system, together with the distance from the hull to the CLR of the rudder, for a leeway angle of 3° and -3° of leeway, for the tests without the keel.

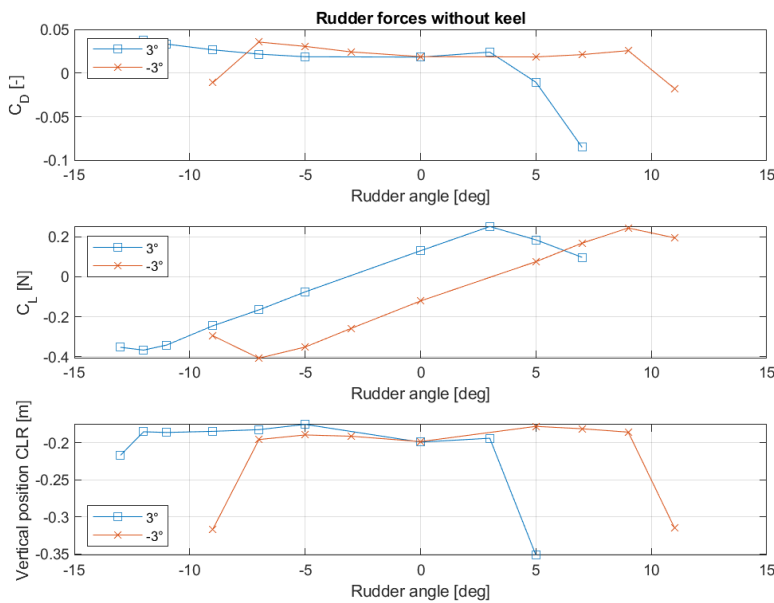


Figure 4.16: The rudder lift and drag forces on the reference earth axis system, together with the distance from the hull to the CLR of the rudder, for a leeway angle of 6° and -6° of leeway, for the tests without the keel.

The way figure 4.17 is presented gives a clear comparison between the drag and lift curves for positive and negative leeway angles. If a phenomenon would occur inducing a change on the leeward side of the hull, this should be visible in this figure. However, this is not the case. Still, for positive rudder angles the stall angle is low and for the negative rudder angles it is a little lower than expected ([20]).

A way to check symmetry is to see whether the downwash angles for positive and negative leeway angles are equal. This should lead to, for example, alignment mistakes or asymmetry in the hull or appendages. In figure 4.17 shows that the downwash angle difference is around 20% relative to the mean. As said before, this could be caused by alignment mistakes or asymmetry of the model, but as concluded in section 4.1.2 these two causes seem unlikely. It could also be due to circulation in the tank, could cause this difference in angle of incidence, or a combination of both.

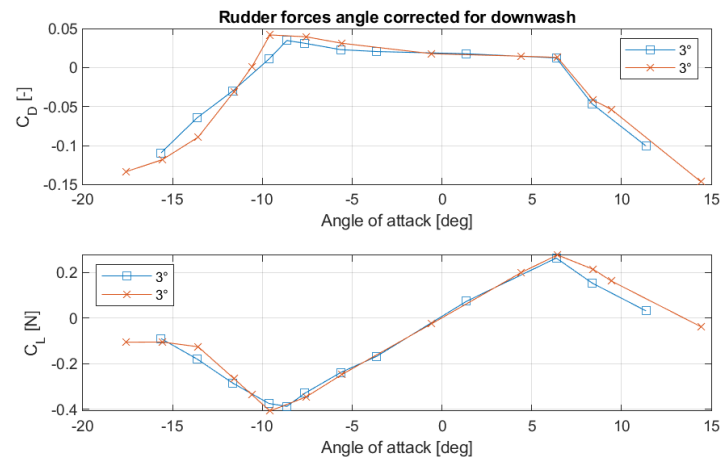


Figure 4.17: The rudder forces for 3° and -3° of leeway, corrected for their downwash angle. The angle of incidence on the rudder is relative to the local flow.

4.4.3. Comparison previous experimental data

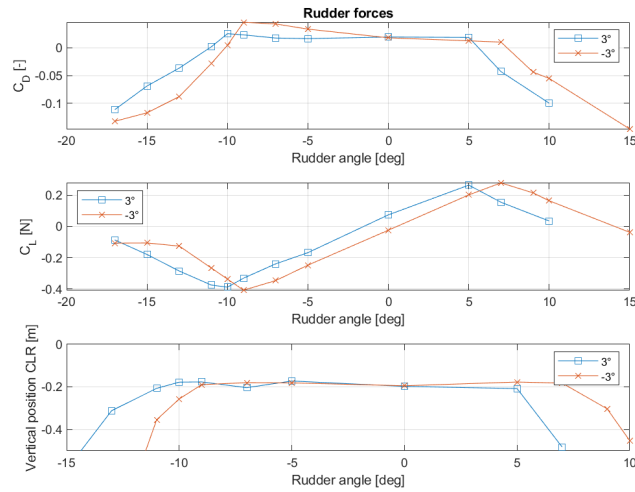
The results are now roughly analysed, the question remains to what extent the newly obtained experimental results are comparable to the previous results. Note, because it is not entirely clear how the old results were obtained and what the uncertainty of these results is, they will only be compared globally to the newly obtained results. Assumed is, however, that globally the same procedure is used in elaboration of the data. The newly obtained results will also be the benchmark in the comparison with the CFD results and the old experimental results will be neglected.

As for the lift and drag curves of the rudder, the same magnitude of forces is found for both the lift and drag curves, looking at the forces at 5° , -5° and -10° . Also, looking at the lift curve in the negative rudder angle region, both plots show the same stall angle for the 3° leeway angle. For the positive rudder angles, however, the similarity is not the case, the results in figure 4.18a showing a smaller stall angle than the results of figure 4.18b.

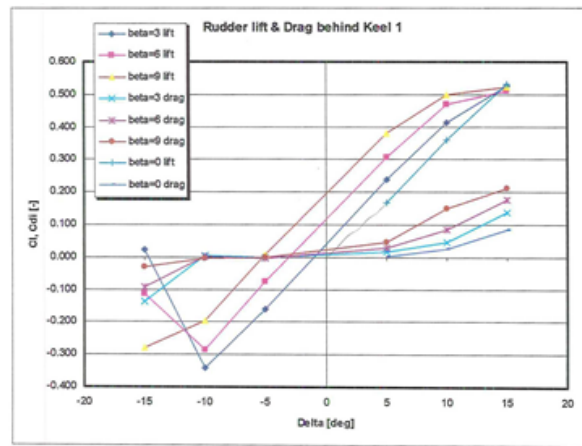
As for the drag curves, the same unexpected behaviour of a negative C_D is found after the stall angle of the rudder, this could indicate a physical phenomenon causing the positive drag. However, the drag forces in 4.18b are the induced drag, this could give a difference in the results.

To conclude the comparison between the old and the new results, the downwash angle is compared. First, one can immediately see the correspondence in linear behaviour.

When taking a closer look, it can be concluded that the magnitudes of the angles found in both cases deviate. For the 3° leeway angle the smallest difference is found to be 0.035° , increasing to 2.7° for 9° of leeway. Note: in the previous experiments, as far as known, only positive leeway angles are tested for keel 1, the downwash angles for those are thus compared. The difference could originate from a deviation between the set-up of the experiments. It is unlikely that a physical phenomenon is behind the deviation. For this comparison it would be beneficial to perform similar experiments.



(a) The rudder lift and drag forces on the reference earth coordinate system, together with the distance from the hull to the CLR of the rudder, for a leeway angle of 3° and -3° of leeway.



(b) The rudder lift and drag found in the experiments conducted by Keuning et al. [32] for a number of positive leeway angles over a range of rudder angles.

Figure 4.18: Two figures for the comparison of the towing tank data found in these experiments and found by Keuning et al. [32].

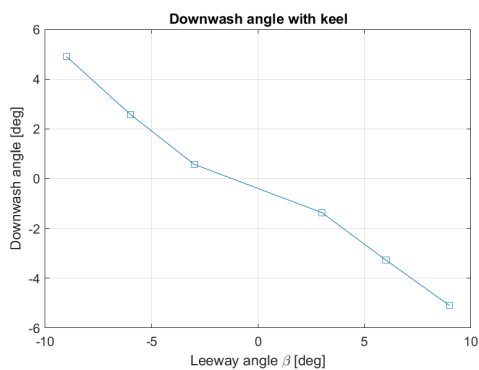


Figure 4.19: The downwash angle of the keel on to the rudder.

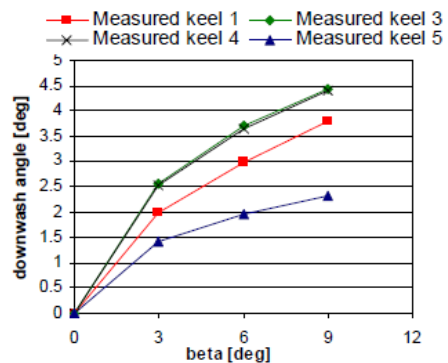


Figure 4.20: The downwash of the keel on to the rudder for the test case with keel, found by Keuning et al. [32]

4.5. Conclusions of the experimental results

The results of the hull and the keel are as expected with no strange behaviours. Also, the precision in alignment and calculations are to be assumed sufficient, without known errors.

The rudder forces show a number of unexpected aspects in the results. Firstly, the negative resistance coefficient found after stalling of the rudder. Secondly, the moment of stalling of the rudder raises some questions.

It seems that this negative drag coefficient is a measurement error as this effect is not visible in the total drag versus rudder angle. From the results it seems that the lift curve for the negative rudder angles seem to be physical. The analysis on these results will continue in chapter 6.

The comparison with the results of the previous experiments only gave the confirmation that the stall angle for the negative rudder angle is a repetitious phenomenon in both experiments; this substantiates the argument that the phenomenon is physical.

The comparison of the downwash angle and the stall angle of the positive rudder angles, however, raises questions on the correctness of either of the experiments.

Further research needs to be undertaken to give a decisive answer on the correctness of the experimental results and to give an answer on the possible physical phenomena giving the unexpected experimental results.

5

Uncertainty assessment

Uncertainty assessments are an important tool in comparing different types of experiments, or even different experiments. So in order to be able to compare the towing tank results with the numerical results, an uncertainty assessment must be made for both experiments. In this chapter the uncertainty assessment of both the numerical experiments and towing tank tests are discussed. The focus of this chapter is on the numerical uncertainties; section 5.3 is dedicated to the uncertainty of the towing tank tests.

Within the numerical experiments there are multiple sources of uncertainties/errors to be found. In Eça and Hoekstra [10] these error sources are discussed in more detail, possible error sources are: modelling errors, programming errors, numerical errors, round-off errors, iterative errors and discretisation errors. All these errors are discussed throughout this chapter, in combination with the methods to determine them.

In this chapter, first the code verification and the necessary steps are discussed; afterwards a section will follow on solution verification and validation.

5.1. Code verification

By using a commercial CFD code for this research, the code verification is already executed by the developers of the code/program. Code verification is namely the assessment if the code indeed solves the equations correctly, without bugs etcetera [10]. NUMECA participates in a number of workshops. In these workshops a test case is given for code developers, which then can be executed to determine if the code solves the test case correctly. An example of such a workshop is the Tokyo 2015 workshop. Both d'Aure et al. [5] and Deng et al. [6] did a verification and validation study for it, both concluded that the results they found for the resistance tests had a deviation; for d'Aure et al. [5] of around 2%; for Deng et al. [6] of around 7%. Deng et al. [6] also concluded that it is difficult to obtain a grid independent solution for wake flow for a grid with less than 10 million cells.

NUMECA and Nantes and CNRS [43] ensured that the implemented code is verified, which is confirmed by Deng et al. [8]. So from here on, it is assumed that there is no need for a code verification.

5.2. Solution verification

"Solution Verification is an ongoing activity that should preferably be performed for every application of the code.", as stated by Eça and Hoekstra [10]. This means that preferably for each computation the solution is verified. However, this is for most users impracticable, also because in some applications a comparable solution is not available. The latter is to some extent the case in this study. Because it is not clear what the solution should be around the found stall angles in the towing tank experiments. In addition to this the time for the numerical experiments is too limited to perform a verification study for each case. As a compromise a verification study has been conducted for two cases, from which the outcome was as expected.

In this section the solution verification used for the two cases will be discussed. This verification will be done via a grid refinement study, based on the method by Eça and Hoekstra [10] and Eça and Hoekstra [11].

5.2.1. Possible sources of errors in CFD simulations

As discussed in the introduction of this chapter, within numerical simulations there are a number of error sources which influence the correctness of the simulations. In this section the most important errors in nu-

merical simulations are discussed. This section can be seen as a summary of Eça and Hoekstra [10].

Modeling errors; these errors are quite intuitive. It is the error due to the CAD/domain model. First of all, in studies as this one an unavoidable error is made between the CAD model, used for the simulations and the, at best, by hand finished towing tank model, the difference is discussed in section 3.6.1. In addition to these errors, Eça and Hoekstra [10] also state that the modelling of the domain has influence on the modelling error. The modelling errors are of influence in the validation part of the numerical uncertainty assessment [10].

Numerical errors; as CFD methods are numerical methods, naturally numerical errors are present. In numerics three possible errors sources can be assigned:

Round-off errors: are a product of the finite precision of computers. The round-off error can be seen as the error made because of a maximum number of decimals available. Usually, the round-off errors are negligible, although they could limit the amount of grid-refinement.

Iterative errors: originate from non-linearities in the calculations. Eça and Hoekstra [10] state, that possible sources in RANS equations come from: the convective terms, deferred correction and turbulence closure. In the essence it should be possible to decrease the iterative errors to machine precision, although in reality this level of convergence is seldom reached, especially for complex flows. According to Eça and Hoekstra [10], the iterative error can be neglected when it is two or three times lower than the discretisation error, although they also state that this is often not the case and the iterative error is incorrectly neglected.

The discretisation error: is the largest error of the errors mentioned here. This error originates from the discretisation of the simulations. The discretisation error will decrease with an increasing grid size. To determine this error a grid refinement study can be used. This requires a couple of geometrically similar grids refined with the correct intervals. This method is used here to determine the discretisation error [10].

5.2.2. Discretisation error

A program developed by MARIN [39] will be used for the estimation of the discretisation error. This program is based on the method described in Eça and Hoekstra [11] and is based on a least-square fit through the outcomes of the grid refinement simulations. From this fit the errors for each grid will be determined and could also be used to estimate the solution at a infinite fine grid, i.e. the physical solution for the CFD simulations. This is important in the section about validation.

The method of Eça and Hoekstra [11] has a couple of requirements for the grids, in order to ensure decent results. First of all, a minimum of 4 grids is required to come to a decent fit. All of these grids need to be geometrically similar and fall in the asymptotic range. The geometric similarity require the grids to be refined with a constant factor. Apart from the demands for the grids, the solutions over these grids need to converge monotonous. Whether this is the case or not, can be determined with the discrimination ratio:

$$R = \frac{(\Phi_1 - \Phi_2)}{(\Phi_2 - \Phi_3)} \quad (5.1)$$

The indices (1, 2 and 3) stand for fine, medium and coarse grids. The following can be concluded from the discrimination ratio, according to Eça and Hoekstra [11]:

- Monotonic convergence: $0 < R < 1$
- Monotonic divergence: $R > 1$
- Oscillatory convergence: $R < 0$ and $|R| < 1$
- Oscillatory divergence: $R < 0$ and $|R| > 1$

When the solutions meet the above described requirements; the fit and uncertainties can be found using the by Eça and Hoekstra [11] proposed method. First of all, the method uses the following equation to determine the discretisation error:

$$\epsilon_\Phi = \alpha h_i^p \quad (5.2)$$

The α , p and the standard deviation of the fit are found with the use of a set of non-linear equations.

The fit is made from these parameters, as well as the uncertainty estimate. The uncertainty estimate is based on, among others, the standard deviation and the difference between the actual value and the fitted value. Also a safety factor is used in the uncertainty estimate, which is either 1.25 or 3 depending on the standard deviation and the difference between the maximum and minimum value from the CFD simulations. This has as a consequence that if the data set is not perfect the uncertainty could become large [11].

When the solutions does not meet the requirements, determined from the value of R or p , Eça and Hoekstra [11] proposes the use of linear functions and quadratic functions for the fit. Whether a linear or quadratic fit, or a combination, is used depends on the standard deviation; the fit with the smallest standard deviation is favoured. The reason for the use of linear or quadratic functions is that CFD simulations are often executed in a second order or lower method. When the appropriate values for the Φ_{fit} , standard deviation and the error are found, the normal procedure of estimating the uncertainty can be used.

There are a number of possible reasons why the data set could not be optimal. According to Eça and Hoekstra [11] an important reason is not having geometrically similar grids and grids not being in the "asymptotic range". Also, additional functions within turbulence models, which ensure the overshoot, could give complications in the assessment.

5.2.3. Grid development for the grid refinement

The previous section mentioned the requirements for the grids, chapter 3 discusses the development of the base grid, this grid will be refined and coarsened for the grids in the refinement study. As discussed above, minimal four grids are necessary for the analysis, so in this analysis five grid sizes are used.

In addition to the requirement of the grids being geometric similarity; are the distances between the different grid sizes also of importance. The distance between the grid sizes is linked to the asymptotic range, when the grid sizes are chosen with care, it is more likely that the results fall within the asymptotic range. An important measure for the grid refinement is the grid refinement factor: $r = \frac{h_{i+1}}{h_i}$, where h_i is a typical grid size. When grids are produced with the use of this grid refinement factor it is ensured that a geometrically grid is produced with the same distance between the sizes [49].

A grid refinement factor of 2 is proposed by Roach [49]. This would mean that the grid is doubled or halved. Although, this is not necessary or feasible for this particular case. For practical reasons ITTC [3] proposes to use a refinement factor of $\sqrt{2}$.

The grid refinement to ensure geometric similarity is straightforward for structured grids and specific unstructured grids. However, Hexpress [47] requires a specific approach. This is discussed in the next paragraphs.

As explained in chapter 3, Hexpress [47] is an unstructured mesher, working with hexahedral cells, and uses certain settings to change the grid size. Hexpress [47] works with an initial mesh, which is refined to the wishes of the user. In the refinement the cells are divided by a factor, which is equal to 2^n where n are the number of refinements. The refinement is only possible at the faces of the body or in a predetermined box and is diffused away from the selected location by a predetermined factor.

Applying a geometric similar grid refinement on a Hexpress [47] mesh is not as straightforward as other program/methods, because in Hexpress [47] no function is available which automatically refines the meshes with a factor. NUMECA [46] advises to make use of the initial mesh, target cell sizes and the refinement diffusion to refine or coarsen the mesh. As these mesh parameters require integers, the refinement factor proposed by ITTC [3] is of no use to the grid refinement. NUMECA [46] proposes to a factor $\frac{1}{4}$ and an initial mesh size of a multiple of four.

The settings for the three refinement criteria used in Hexpress [47] are displayed in table 5.1. The equations used to find the correct values for the parameters are shown in the first row. The other rows show the parameters for the different grids. As explained in chapter 3; are the free-surface and the gap of the rudder the only faces with a target cell size and a different diffusion.

In Hexpress [47] the boundary layer is discretised with the use of viscous layers. These layers are related to the y^+ distance of the face, see chapter 3. As the y^+ distance influences the first layer thickness of the viscous layers and the y^+ is a fixed value for every grid, the first layer distance will be a fixed value in the grid refinement. The number of viscous layers are important to couple the viscous layers to the euler mesh. As the euler mesh changes over the grid refinement, is it necessary to change the number of viscous layers for every grid. These viscous layers will not change with the use of the grid refinement factor, but relative to the first cell distance from the wall of the euler mesh.

Table 5.1: The settings from the grid refinement in Hexpress [47]. The variable r_i indicates the refinement factor, the D is the diffusion factor, the n is the number of cells and h is a typical cell distance.

	r_i	D	initial cell size	target cell size FS	D_{FS}
equations	-	-	$(n_x, n_y, n_z) * r_i$	$(h_x, h_y, h_z)/r_i$	$D_{FS} * r_i$
coarse	0.75	2	(12, 6, 3)	(1.83, 1.83, 0.0072)	3
medium	1	3	(16, 8, 4)	(1.37, 1.37, 0.0054)	4
fine	1.25	4	(20, 10, 5)	(1.10, 1.10, 0.0043)	5
finer	1.5	5	(24, 12, 6)	(0.91, 0.91, 0.0036)	6
very fine	1.75	6	(28, 14, 7)	(0.78, 0.78, 0.0031)	7

A second deviation in the grid refinement is the gap between the rudder and the hull. In this gap the cell size will stay constant throughout the different grids. When the cell size is not kept constant this will lead to impractical small mesh sizes for the finer grids and the mesh size in the gap will quickly become too large in the coarsened grids. In table 5.2 the number of viscous layers can be found as well as the refinement factors for the rudder gap.

Table 5.2: The settings for the viscous layers and the refinement of the rudder gap, for the different grids.

	Number of viscous layers (hull, keel, rudder)	Inflation factor	ref_{gap}
coarse	(24, 21, 28)	6.7	13
medium	(21, 19, 26)	6.1	12
fine	(21, 18, 25)	6.4	12
finer	(20, 17, 24)	6.4	12
veryfine	(19, 16, 23)	6.2	12

The final variable to be changed for a proper grid refinement study is the size of the time step. As discussed in chapter 3, the suitable time step depends on the flow velocity and the grid size. The Courant number is the measure for the correct time step size. In short, the Courant number should be the same over the grid range and the time step should decrease/increase with the same factor as the typical grid size h_i , thus with the refinement factor r_i . In table 5.3 the time steps for the grids are shown. The reference time step value is made for the medium grid according to proposed value by NUMECA [46].

Table 5.3: The time step values for each grid. In the first line the equation is given to adapt the time step.

	time step
equation	$\Delta t / r_i$
coarse	0.02
medium	0.015
fine	0.012
finer	0.01
veryfine	0.009

5.3. Uncertainty assessment of the towing tank experiments

In the introduction of this chapter is mentioned that a comparison is made between the experimental results and the CFD results. Because of this comparison, an uncertainty assessment has to be made for the experiments. The recommended procedure of the international towing tank conference (ITTC) will be used in the assessment.

The first uncertainty source discussed by ITTC [25], is the geometric uncertainty. This is the deviation of the constructed model and its lines plan. Included in this uncertainty is the density of the water, which influences the displacement of the model. The ITTC [25] states, that these differences are so small, or hard to numberise, that they can be neglected from the uncertainty estimate.

In this particular case, the actual model is measured and copied, thus the deviation between the lines

plan (CFD model) and the actual model is assumed negligible. Also the model is towed underneath the hexapod, which holds the model in one position, thus the model will hardly be affected by the change of water temperature. This position is daily checked to ensure correct measurement conditions.

The second source stated by ITTC [25] contains the installation uncertainty, which contains, among others, the uncertainty due to the misalignment of the set-up. In section 4.1.2 the alignment procedure used in these tests is described. During the tests this alignment is done to the best of capabilities, following the process used by the towing tank. For these reasons and others ITTC [25] advise to neglect this uncertainty source.

The ITTC [24] also recommends to perform a data reduction. This data reduction consist of correcting the measurements to the desired velocity and the correction of the viscosity for the water temperature. The difference in water density due to the temperature variation is negligible.

After a short analysis it appears that both corrections are negligible small, see table 5.4 and table 5.5. The correction for the velocity will be made in the experimental data, to ensure leaner calculations. The correction for the viscosity is rather more cumbersome and the improvement will not justify the time spent on the additional calculations.

Table 5.4: Error of the total resistance due the correction for the velocity in x -direction for the model, keel and rudder, in a percentage of the measured resistance.

Vel [m/s]	Model [%]	Keel [%]	Rudder [%]
1.04	-0.0017	-0.0017	-0.0017
1.81	-0.003	-0.003	-0.003
2.07	-0.0029	-0.0029	-0.0029

Table 5.5: Error of the total resistance made, because of the correction of viscosity, due to water temperature variations for three different temperatures, in a percentage of the measured resistance.

Temp [°C]	Model [%]
20.4	0.0081
20.6	0.0123
20.1	0.0018

After the data reduction only two uncertainty components are left, one of them is the uncertainty in the dynamometers. These are tested before the test commenced, using the methods of the TU Delft towing tank, by placing a series of weights on the sensor and removing these for both the positive and negative measurement direction. This to find the effect of hysteresis and to be able to determine the uncertainty of the sensors.

The uncertainty is determined by comparing the delta of the forces to the delta of the changes in voltage. This uncertainty is expressed in a percentage of the mean ratio of the delta of the forces over the delta of the voltage. In figure 5.1 the output of the sensor is plotted against the force applied. Showing different points and lines for increasing and decreasing force. From this graph is it is possible to see that the hysteresis is small for this sensor and almost negligible.

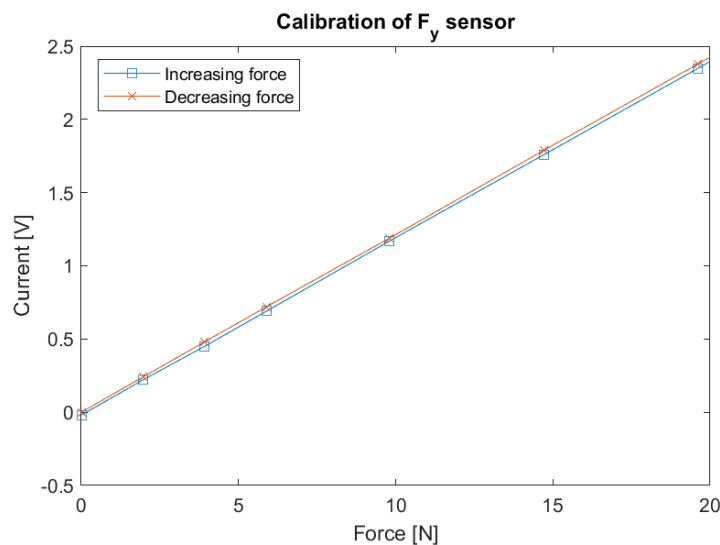


Figure 5.1: An example of the results of the calibration of the F_y sensor for the rudder. Both the increasing force and the decreasing force are displayed, plotted against the voltage given by the sensor, showing the hysteresis of the sensor. For visibility reasons is the range of the x -axis is decreased.

For the moment sensors the same procedure is followed. Only the procedure with the weights is done twice at a distance from the sensor. The distance between the two measurements is a known fixed distance. From this procedure the zero points of the arm can be located and the uncertainty of the distance between the two measurements can be derived.

The final uncertainty source for the experiments according to the ITTC [25] is the uncertainty from repeated measurements. This uncertainty can be determined with certainty if a large series of repeated measurements is conducted, if not, ITTC [25] advises to consult a database of similar tests. The first method to determine the uncertainty was not an option due to time restrictions, the latter is also difficult as there are hardly similar tests with a test program to determine the repeated uncertainty.

To determine the repeated uncertainty an educated guess is made based on a couple of measurements which are repeated one or two times. The linearity in the lift curve of the rudder is not used for the determination, because this method is only useful for the uncertainty of the lift force for the rudder and the time needed to implement this only would give minor improvements. To follow the advice of the ITTC [25], some reference values from Nico van der Kolk [54] are used as a guideline.

In ITTC [25] a method of using a table is proposed. Each row is for the uncertainties of importance, with the last rows for the combined uncertainty. The use of such a table gives a good overview for the uncertainty components for each particular case. In figure 5.2 and figure 5.3 examples are given of the uncertainty tables and in Appendix E all tables are given. Note, this exercise is only done for the cases which will be compared with the CFD simulations.

Fx_model (beta=3, delta=0)	Type	Uncertainty	Remark
Wetted Area	B	0,03%	neglectable
Dynamometer	A	0,17%	minor
Speed	B	0,29%	minor
Watertemp	B	0,02%	neglectable
Repeated, single	A	1,39%	dominant
Combined, single		1,43%	
Conf interval, single		2,87%	
Repeated, mean	A	0,70%	
Combined, mean		0,84%	
Conf interval, mean		1,69%	

Figure 5.2: An example of the uncertainty table to the example of the ITTC [25]. The model resistance is displayed for the test case of 3° leeway and 0° rudder angle.

Cl_rudder (beta=-3, delta=-5)	Type	Uncertainty	Remark
Wetted area	B	0,03%	neglectable
Dynamometer	A	0,28%	minor
Speed	B	0,29%	minor
Watertemp	B	0,02%	neglectable
Repeated	A	2,55%	dominant
Combined		2,58%	
Conf interval		5,16%	
Repeated, mean	A	1,25%	
Combined, mean		1,31%	
Conf interval, mean		2,63%	

Figure 5.3: An example of the uncertainty table to the example of the ITTC [25]. The uncertainty of the lift coefficient of the rudder is displayed for the test case of -3° leeway and -5° rudder angle.

5.4. Solution validation

The solution and code can now be verified and the uncertainties of the experiments are determined. What remains is to validate the solutions. This validation is conducted, again, according to Eça and Hoekstra [10].

The first important remark Eça and Hoekstra [10] is the following: "we cannot speak of a 'validated code'" Because the validation is done for every problem and variable."

Eça and Hoekstra [10] use the ASM V & V 20 standard in their paper. This method uses a comparison between the difference of the results and the uncertainties determined. The first quantity to derive is the difference between the experimental (D) and numerical results (S): $E = S - D$. The uncertainty used for this validation is the sum of the different uncertainties:

$$U_{val} = \sqrt{U_{num}^2 + U_D^2 + U_{input}^2} \quad (5.3)$$

U_{num} is the numeric uncertainty, U_D the experimental uncertainty and U_{input} is the parameter uncertainty, Eça and Hoekstra [10] advice to neglect this latter variable.

For the validation, the U_{val} needs to be compared to E , this leads to two outcomes according to Eça and Hoekstra [10]:

1. $|E| \geq U_{val}$ the modelling error is comparable to δ_{model} . If δ_{model} is sufficient small the model may be accepted as acceptable for practical purposes, otherwise the model needs to be improved.
2. $|E| \leq U_{val}$ indicates that the modelling error is smaller than the uncertainty, which does not necessarily mean a correct model. If U_{val} is large, attempts should be made to decrease the value. When the uncertainty is small, the model has a good agreement with the experiments.

5.5. Results of the uncertainty assessment

The uncertainties are determined for both experiments, as described in the previous sections. This section presents a couple of examples of the results of the grid refinement study. Both the verification and the validation will be discussed for the examples. The remainder figures will be showed in Appendix F.

The figures presented in this section show the numerical results, the fit, the experimental results and their uncertainties. This is true for all graphs presented regarding the uncertainty assessment.

Figure 5.4 shows the uncertainties for the drag force of the model. In this graph the fit is second order, which would mean that the solution converges with a second order. The solution of the numerics agrees with one of the demands of Eça and Hoekstra [11], namely that the results are in the asymptotic range. From this figure it is also clear that the uncertainties decrease over the grid range, which indicates the desired convergence behaviour. For F_x the grid convergence study indicates a suitable grid for further simulations.

The comparison of the experimental results to the numerical results shows that the numerical results underestimate the drag forces, with a difference of around 2 Newton. There are a couple of possible reasons for the underestimate of the CFD results. One of them is the level of turbulence, which is mentioned later in this section. Another is a suboptimal grid, which is contradicted by the verification. As the error bars of both results overlap, theoretically the values can be assumed equal. According to the validation criterion, discussed in section 5.4, the modelling error is smaller than the validation uncertainty for the middle grid and the uncertainty is acceptable.

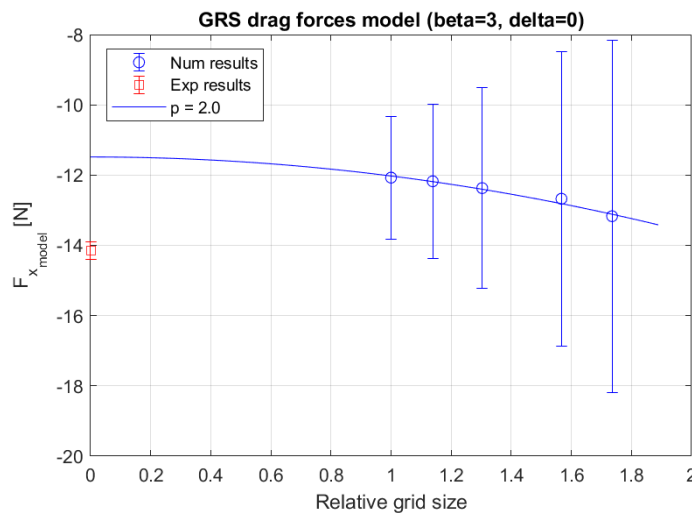


Figure 5.4: The grid convergence plot of the drag of the model, for the test case with $\beta = 3^\circ$ and $\delta = 0^\circ$.

Figure 5.5 shows another result of a grid refinement study. This particular example has a different order of convergence than in figure 5.4, but has smaller uncertainties. Similar to the previous discussed graph are the results in the asymptotic range and the uncertainty again decreases over the grid range. The asymptotic range indicates a valid use of the method and the decrease again indicates a suitable grid.

In the validation of the data, as in the previous discussed graph, the error bars of the experiments do overlap, also the experimental value overlaps with all error bars, excluding the finest. However, the side force

seem to be overpredicted in the CFD simulations. Another difference with figure 5.4 is the magnitude of the uncertainties, in this case the uncertainties are smaller. As for the validation criterion of Eça and Hoekstra [11], the modelling error is smaller than the validation uncertainty: the uncertainty for the finest and middle grid size are both acceptable.

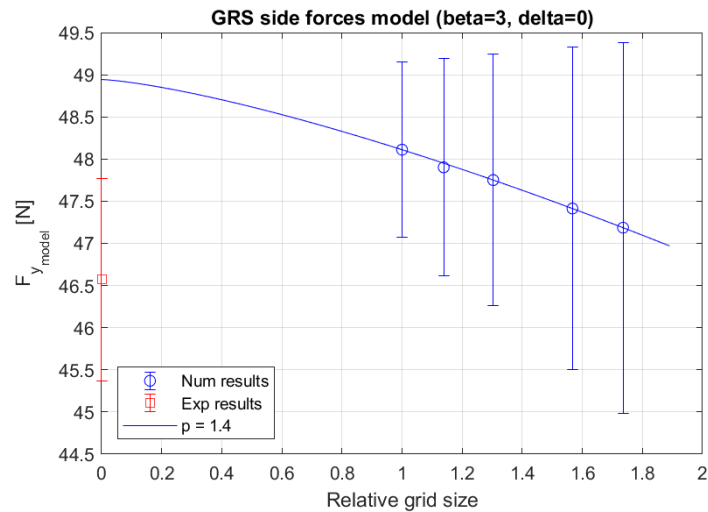


Figure 5.5: The grid convergence plot of the side force of the model, for the test case with $\beta = 3^\circ$ and $\delta = 0^\circ$.

In figures 5.6 and 5.7 the uncertainty assessment of the rudder forces are plotted. The drag coefficient of the rudder, in figure 5.6, shows similar uncertainty behaviour as the resistance force of the model. These figures again show a grid convergence of the second order and the uncertainty decreases over the grid range.

The comparison of the experimental drag coefficient and the numerical drag coefficient do not show an overlap. The CFD simulations underestimate the drag coefficient by such an amount that the value of the drag appears to fall outside the range. This difference is not shown in figure 6.2, because the values are small and it is not the main reason of these simulations. So it is assumed that the difference for this particular case is still acceptable in the bigger picture. The main reason for the deviation is the alignment of the rudder; the test case is around the no lift case for the rudder, so a small alignment mistake could have a large influence on the difference between two experiments. This could also be the case for the difference in figure 5.4.

Here the modelling error is higher than the validation uncertainty, as is expected. However, the error is comparable to some validation uncertainties. As the modelling error is significant, the model could be optimised for the rudder resistance, but this is for further research. The validation was conducted for the fine grid and the finest grid.

The final graph and example to discuss is the uncertainty assessment of the lift of the rudder for $\beta = 3^\circ$ and $\delta = 0$ in figure 5.7. This figure is an example of the method of Eça and Hoekstra [11] failing. The first thing to be noticed is a strange and incorrect fit. A fit with a convergence of zero would give a better fit and leads to a smaller uncertainty. No convergence of the uncertainty bars is seen in this figure, as the fit is incorrect.

When the fit and the method are neglected, it is obvious that the results of the numerical simulations and the experiments are all similar. This makes the validation more straightforward. The validation method of Eça and Hoekstra [11] gives a small modelling error, which is smaller than the validation uncertainty. Even with a relative high validation uncertainty, the small modelling error lets us conclude the CFD model is suitable for this parameter.

Concluding, most variables showed good convergence over the grid range, others less, as for example figure 5.7. Usually the moments showed difficulty in the converge and showed similar behaviour to figure 5.7. The other variables have a convergence behaviour similar to figure 5.4 and figure 5.5. See Appendix F for the complete overview of the grid refinement study.

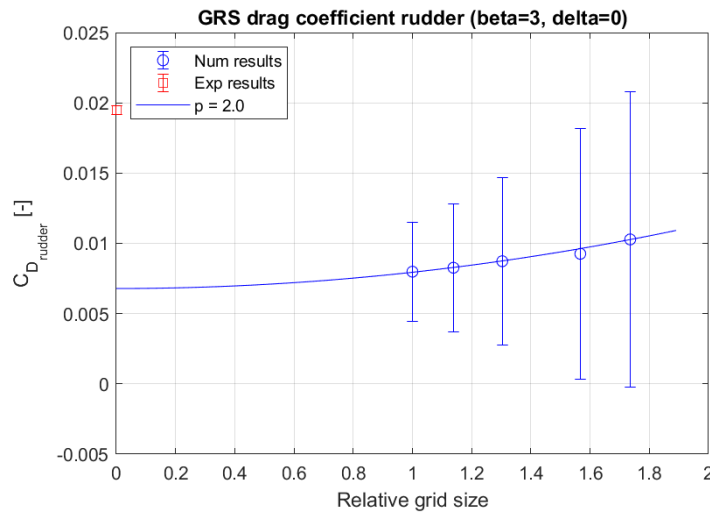


Figure 5.6: The grid convergence plot of the drag coefficient of the rudder, for the test case with $\beta = 3^\circ$ and $\delta = 0^\circ$.

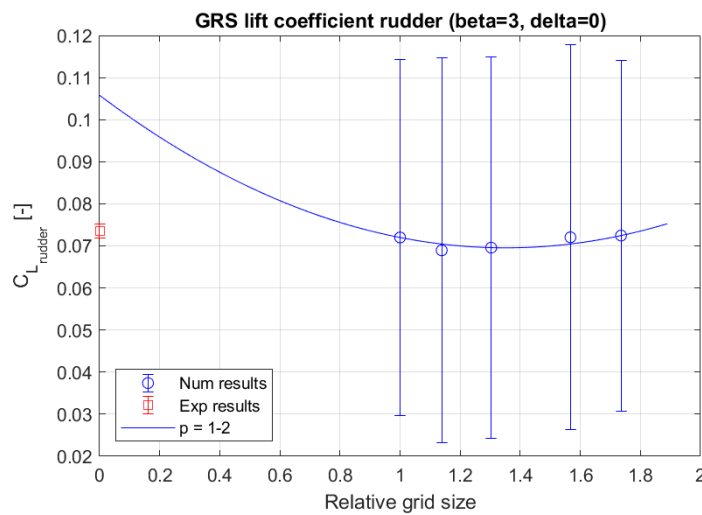


Figure 5.7: The grid convergence plot of the lift coefficient of the rudder, for the test case with $\beta = 3^\circ$ and $\delta = 0^\circ$.

As for the validation the drag forces are usually underestimated, especially for the rudder. The main reason for this is the alignment of the rudder in the experiments, as a small alignment mistake leads to large differences in drag force. Also, it is unclear whether the turbulence levels in both experiments are equal.

The other variables, even without grid convergence, showed good agreement between the numerical and the experimental results. For most variables the validation uncertainty for the fine grid is larger than the modelling error and for most cases the magnitude of the validation uncertainty is significant, however acceptable in this case. For the cases where the modelling error exceeds the validation uncertainty; the magnitude of modelling error is similar to the magnitude of the average validation uncertainty and thus also acceptable.

The designed grid gives comparable forces to the experiments and will be used in this study, figures 6.1 and 6.2 support this. Although, when time would allow, an optimisation of the CFD model would be desirable. The fine grid will be suitable for the CFD simulations and will therefore be used in further simulations.

5.5.1. Verification other variables

The grid and model are verified and validated for the forces. However, to obtain the comparable forces from the CFD is not the only purpose of the CFD simulations. An important reason for the CFD simulations is to "look in the wake of the flow", this requires a different verification criterion. Namely, the variables of interest

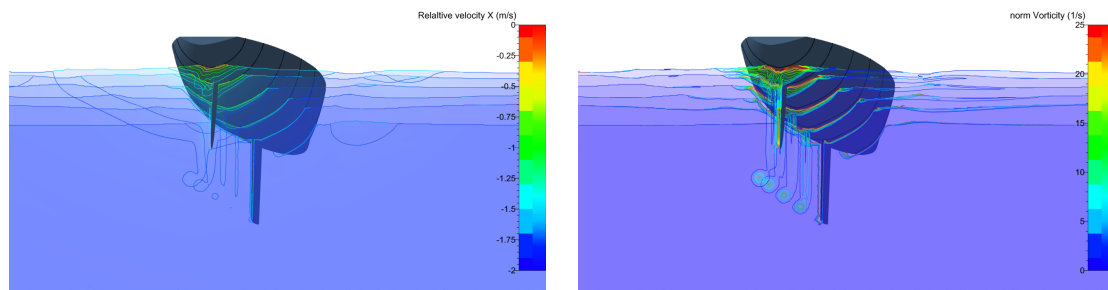
plotted over various faces should comply to the previous mentioned requirements by Eça and Hoekstra [11]. This section presents the result of four variables. For the finest, the middle and the coarsest grid, in that specific order.

In figure 5.8 (a, b, c) the relative velocity in x -direction is plotted on a number of cross sections in the flow. In these figures the influence of the keel on the velocity is visible. This case it seems that the keel decreases the flow velocity in the wake.

The results for the finest grid in figure 5.8.a show a higher precision of the flow field than the results on the other grids. This has to do with a larger numerical diffusion in coarser grids. However, all grids show the same flow structures and no particular large deviation is detected from the different figures.

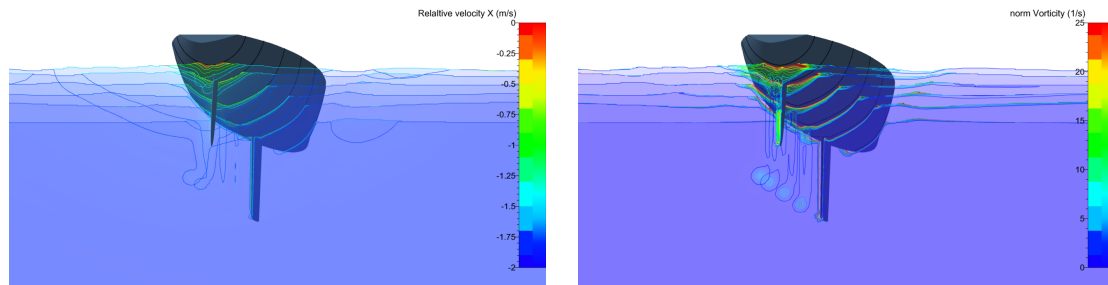
In the figures 5.9 (a, b, c) the normalised vorticity is plotted on the same cross sections as the velocity in figures 5.8. In the figures showing the normalised vorticity the same behaviour of the results can be found as in the previous discussed velocity plots.

From the results discussed above can be concluded that the middle grid is suitable for determining the flow structures in the wake.



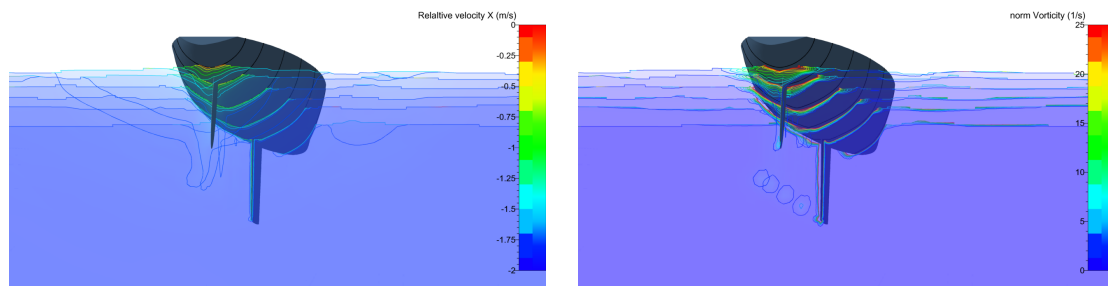
(a) Results presented for the finest grid.

(a) Results presented for the finest grid.



(b) Results presented for the middle grid.

(b) Results presented for the middle grid.



(c) Results presented for the coarsest grid.

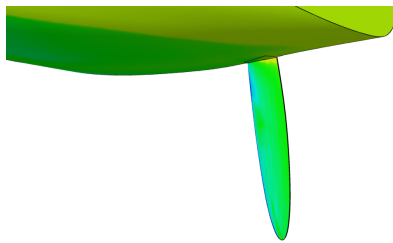
(c) Results presented for the coarsest grid.

Figure 5.8: The velocity in x -direction for the test case of 3° leeway and 0° rudder angle.

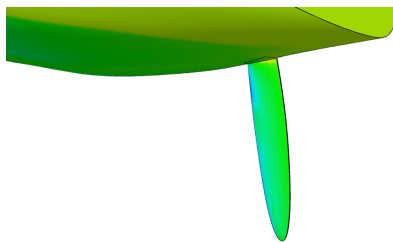
Figure 5.9: The normalised vorticity for the test case of 3° leeway and 0° rudder angle.

Figures 5.10 and 5.11 show the shear stress in x -direction on the rudder and the λ_2 -criterion near the rudder. The effects seen in the two figures are similar as mentioned in the discussion on the velocity and normalised vorticity, only the effects are smaller, because the grid refinement on the rudder is relatively smaller than in the other cases.

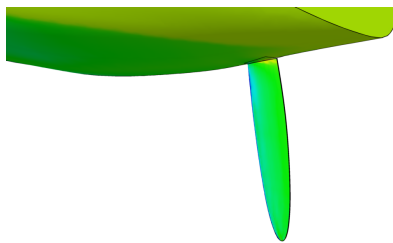
The increased precision for the shear stress shows on the port side of the rudder an increase in regions with larger negative values. For the λ_2 the indications of vortex cores are stronger for the finer grids. As with the previous cases, no other behaviour of the flow over the grid range is detected. Again the middle grid is sufficient to capture the important flow phenomena necessary in this analysis.



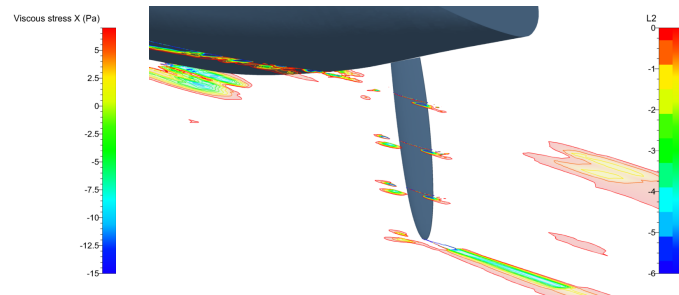
(a) Results presented for the finest grid.



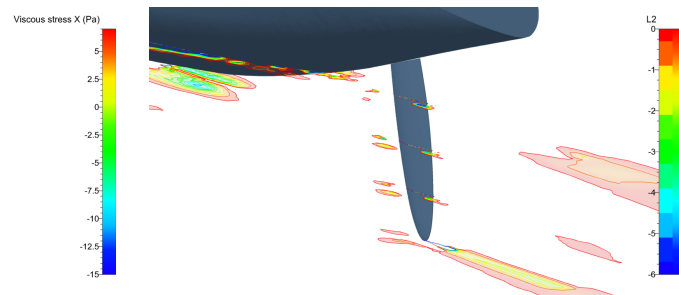
(b) Results presented for the middle grid.



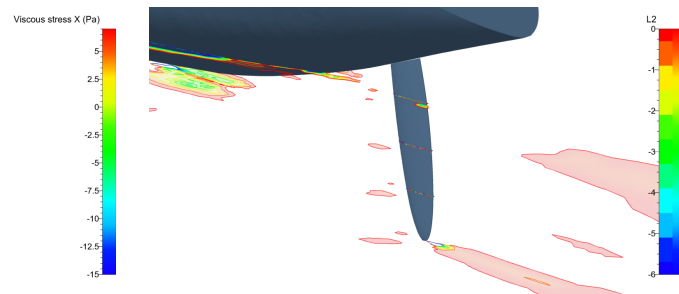
(c) Results presented for the coarsest grid.



(a) Results presented for the finest grid.



(b) Results presented for the middle grid.



(c) Results presented for the coarsest grid.

Figure 5.10: The shear stress on the rudder x -direction for the test case of 3° leeway and 0° rudder angle.

Figure 5.11: The λ_2 near the rudder for the test case of 3° leeway and 0° rudder angle.

From the above discussion we have seen that for four important variables the precision of the results increases over the increasing grid size. For the results presented in figures 5.8 and 5.9, the influence of the grid size is larger than for the other figures (figures 5.10 and 5.11), because the refinement of the grid is relatively large in the regions shown by the figures 5.8 and 5.9.

A positive influence of the grid refinement is detected: the precision of the results increases over the grid range. The design of the grid and the grid size for the middle grid are both appropriate for the simulations. We can thus conclude that the CFD model is also successfully verified for the other variables used in the analysis.

6

Analysis of results

This final chapter focuses on the comparison of the experimental and numerical results. In addition an in-depth analysis of the results is given, in which is tried to answer the questions from this study using the results. The chapter starts with the comparison of the results. The CFD results presented in this chapter will be shown enlarged in appendix G.

6.1. Comparison between experiments

This section compares the results of both the towing tank experiments and the CFD simulations. Both the model forces and the rudder forces are compared, the keel forces will not be compared, as only one leeway angle with keel is tested in the CFD simulations. It is not the aim of this section to clarify the results, this will be done in section 6.2.

6.1.1. Model forces

The model forces are presented in figure 6.1. This figure shows an overall good agreement between the CFD simulations and towing tank experiments. A few differences are found in the experiments.

The drag forces show some differences at random locations. However, the uncertainty bars are still overlapping. The uncertainty is discussed in detail in chapter 5. In short, the uncertainty is assumed acceptable in chapter 5.

The results of the side force and moment around the z -axis, for rudder angles smaller than $\delta = -10^\circ$, show a good agreement for both experiments. For rudder angles larger than $\delta = -10^\circ$, the CFD results seem to underestimate the forces and moments. It is possible that there is an underestimation because of earlier separation behaviour of the rudder, which is induced from a lower turbulence level in the flow, in comparison to the experiments.

6.1.2. Rudder forces

Figure 6.2 shows the results for the rudder forces of both the towing tank tests and the CFD simulations for a leeway angle of 3° . Figure 6.3 shows the same results for test case with only the rudder fitted and 0° leeway.

In the first figure (figure 6.2), the region between a rudder angle of -10° and 5° (the assumed stall angles from the experimental data) shows good agreement between the experiments. Outside this region both experiments start to show different results.

Let us first focus on the drag forces. From figure 6.2 the following can be noticed: the experimental drag coefficient changes sign, while the numerical drag coefficient increases. The steepness of both curves does seem to be equal. The two rudder angles of $\delta = -10^\circ$ and $\delta = 5^\circ$ do seem to indicate a change in the drag curve, as the steepness of the curve increases, which could indicate separation and stall behaviour.

As for the lift curve, again the $\delta = -10^\circ$ and $\delta = 5^\circ$ bound the region of similarity in the results and outside a discrepancy is found. As already described in chapter 4, the lift curve of the experiments indicates stall behaviour around the rudder angles of $\delta = -10^\circ$ and $\delta = 5^\circ$. The lift curve of the CFD simulations does seem to change steepness, which could indicate stall as well, as mentioned in chapter 3. The latter, would mean that the CFD simulations agree with the experimental results.

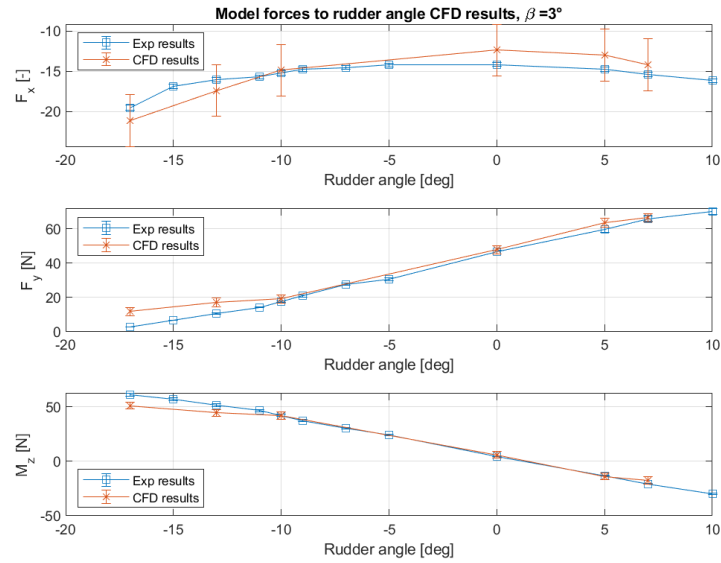


Figure 6.1: Comparison between the model forces of the results from towing tank experiments and from the CFD simulation for 3° of leeway.

The vertical position of the *CLR* has the same behaviour as the lift curve and drag curve, regarding the similarity of the both experiments. The results of the CFD simulations do not change over the rudder angles, which means that the side force (e.g. lift force) and moment around *x* both change in equal rate; this is not the case for the experimental results. An possible explanation for the experimental results is that the location of separation does not occur simultaneously over the rudder. From further analysis this is confirmed, although the stall behaviour is first seen at the tip. This would decrease the distance of the *CLR*. See for example figure 6.11. From the results it seems that the results of the vertical position of the *CLR* from the towing tank are incorrect.

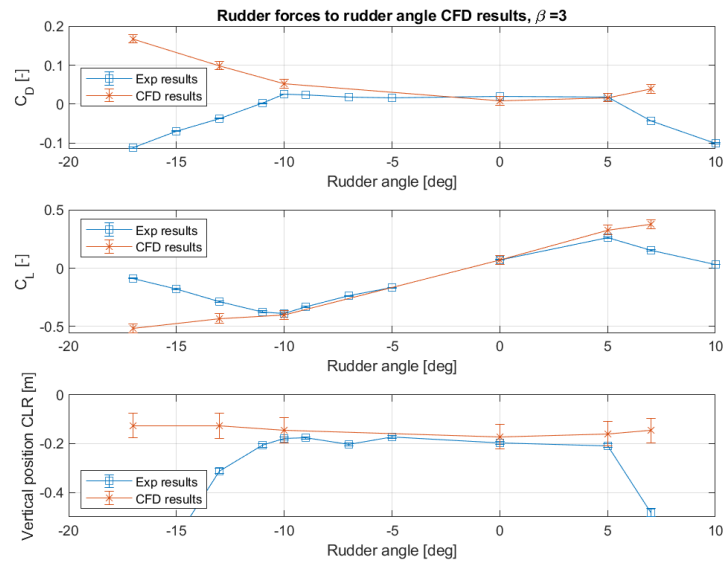


Figure 6.2: Comparison between the rudder forces of the results from towing tank experiments and from the CFD simulations for 3° of leeway.

The test with only the rudder fitted and 0° leeway only has three simulations for the CFD. This is too little to make a full analysis with, but the same behaviour of the results as in figure 6.2 can be seen. From the CFD simulations it seems that the line changes steepness around the 7° rudder angle, for both the lift and drag coefficient, this again could indicate stall behaviour. As this is the case the rudder angle at which separation seems to occur is then different for the CFD simulations and the towing tank tests.

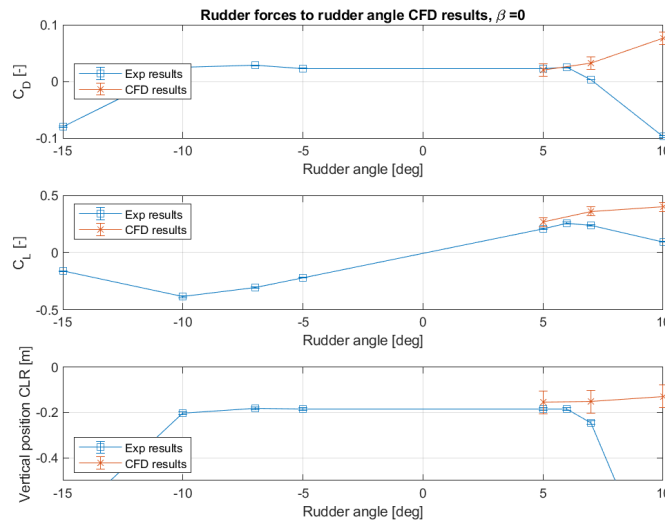


Figure 6.3: Comparison between the rudder forces of the results from towing tank experiments and from the CFD simulation for 0° of leeway and only the rudder fitted.

6.2. In-depth analysis

This section discusses the issues of the previous section in more detail, with the use of the results of the CFD simulations. The focus of this section will be on the parts marked with the red and blue circles. These two parts will be discussed in different sections, namely: the regions circled by the red circles are discussed in the section 6.2.1 and the regions circled by the blue circles are discussed in section 6.2.2.

In this analysis care should be taken with assessing the size and magnitude of the vortex structures dissipated from hull or keel. The flow structures often decrease more in CFD simulations due to the numerical diffusion. For a good analysis the first flow structure from an object should be used for the analysis of the inflow on the rudder.

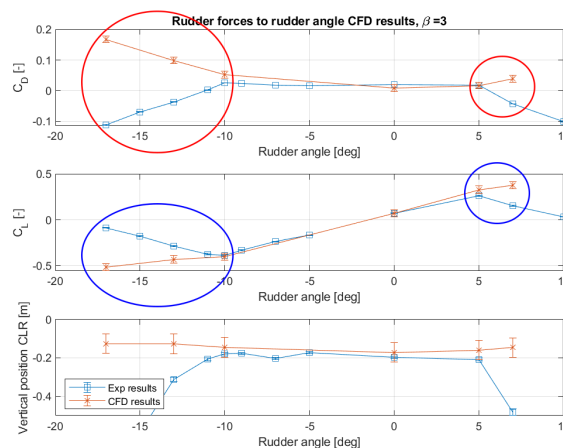


Figure 6.4: The red and blue circled regions indicate the areas of concern and will be of interest for further discussions.

6.2.1. Drag part

The regions circled with red in figure 6.4 raise the question why the experiments show a negative drag coefficient. The most probable physical explanation for this is a direction change in the flow for rudder angles larger than the stall angle. One possibility which could contribute to the change of direction of the flow is the orbital flow of the waves created by the hull.

In figure 6.5 the direction and magnitude of an estimated orbital velocity around the rudder are presented. From this figure it is clear the the orbital flow is in the positive x -direction and could very well be of influence. However, figure 6.6 shows the magnitude of the orbital velocity over the line $x = -0.1$. This figure shows that the maximum orbital velocity to affect the rudder is around 0.17 m/s . With an inflow velocity in the order of 1.8 m/s the orbital velocity is too low to cause an effect which induces a direction switch on the resistance of the rudder. It is more likely that the orbital velocity contributes in the stall behaviour, discussed in the next section.

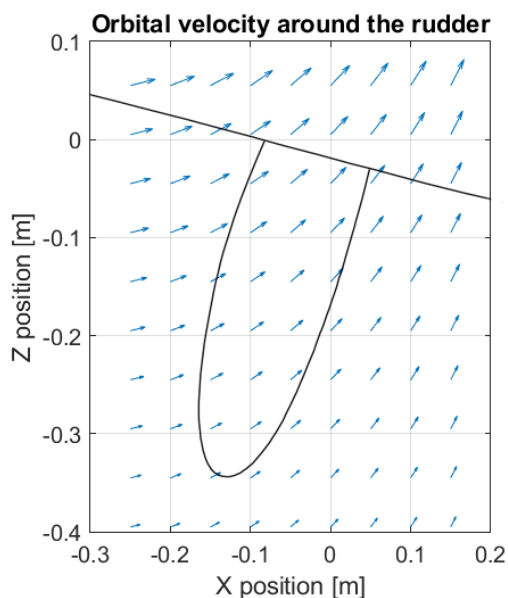


Figure 6.5: The estimated orbital velocity around the rudder.

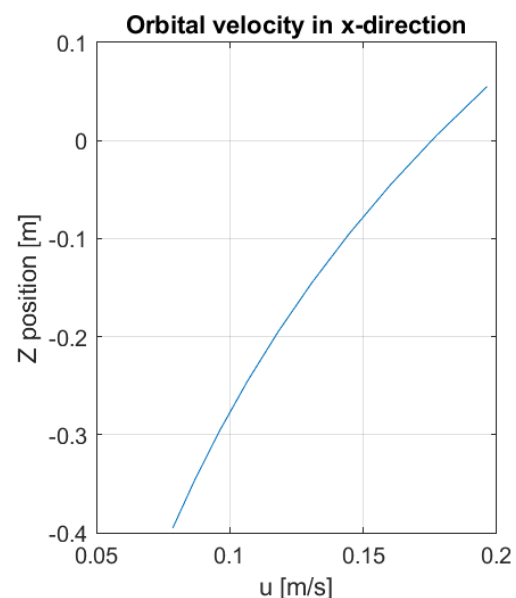


Figure 6.6: The estimated magnitude of the orbital velocity in x -direction over the height on the cross section with $x = -0.1 \text{ m}$.

Figures 6.8 and 6.7 show the CFD results of the velocity around the rudder for test case of $\beta = 3^\circ$ and $\delta = -13^\circ$. In these figures the orbital velocity is already taken into account, the figures show that the velocity vectors are in the expected flow direction. So indeed the orbital flow has little influence on the flow. Interestingly are the two blue vectors near the hull, these indicate a flow velocity of approximately 0.5 m/s .

Apart from a reversal in flow direction one of the parameters from the resistance could be responsible for the negative drag coefficient. Three of the expected resistance components are discussed here.

The first component is the pressure resistance. This resistance is due to the difference in pressure before and after an object, according to Kundu et al. [33]. In figures 6.9 and 6.10 the pressure is plotted on cross sections. From the figures it appears that the pressure is higher down flow of the rudder, than it is up flow of the rudder. This can be explained with the location of the aft stagnation point of the hull. The high pressure due to the stagnation point has only influence downstream of the rudder, but not significant around the rest of the rudder. The pressure downstream of the rudder is increased by approximately 200 Pa . The consequence of this increase in pressure could be a different direction of the resistance force. However, this would mean it is visible in the results of the CFD simulations and in the entire drag curve, which is not the case.

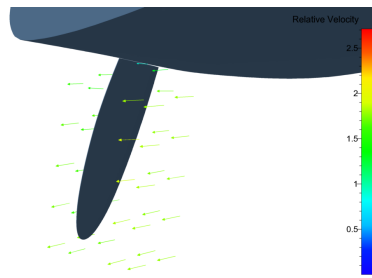


Figure 6.7: The flow direction and velocity around the rudder for test case $\beta = 3^\circ$ and $\delta = -13$, seen from starboard side.

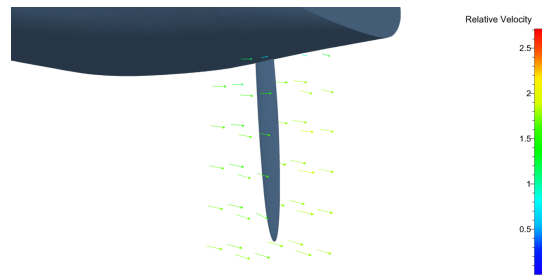


Figure 6.8: The flow direction and velocity around the rudder for test case $\beta = 3^\circ$ and $\delta = -13$, seen from port side.

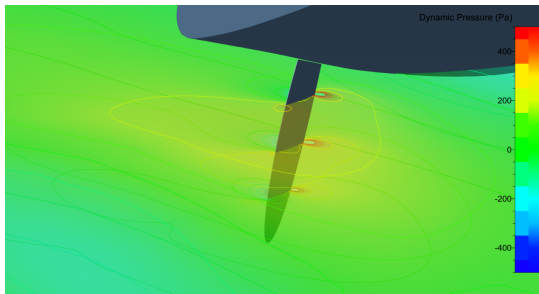


Figure 6.9: The dynamic pressure plotted on xy -planes around the rudder for test case $\beta = 3^\circ$ and $\delta = 7$.

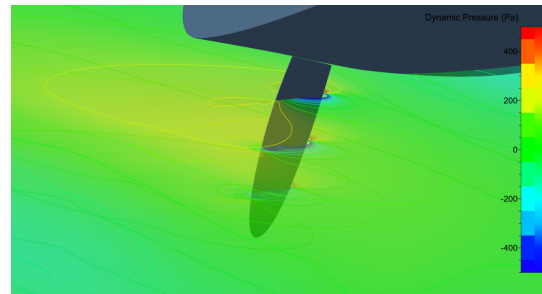


Figure 6.10: The dynamic pressure plotted on xy -planes around the rudder for test case $\beta = 3^\circ$ and $\delta = -13$.

A second component with an effect is the viscous resistance, which is the integration of the shear stress (viscous stress) over the surface. Figures 6.11 and 6.12 show the shear stress on the rudder. From first glance, it is obvious that the direction of viscous force on the rudder has not changed. The viscous resistance will probably have been decreased for the rudder angles after the stall angle.

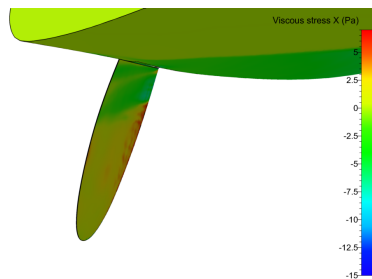


Figure 6.11: The viscous stress in x -direction over the rudder, for the test case with $\beta = 3^\circ$ and $\delta = -13^\circ$, seen from the starboard side.

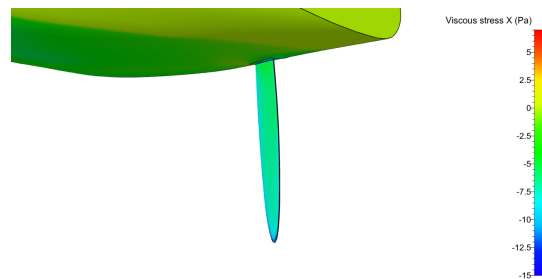


Figure 6.12: The viscous stress in x -direction over the rudder, for the test case with $\beta = 3^\circ$ and $\delta = -13^\circ$, seen from the port side.

The final component of the resistance of an appendage is the induced resistance. This component is also a pressure related force. The resistance is due to a vortex shed from the foil. As the separation of the rudder occurs at the tip the pressure gradient around the tip will decrease, which in turn decreases the induced resistance.

To conclude, the last two mentioned components could contribute to the change of direction of the drag force vector. However, because they only decrease in magnitude they are not actively contributing. The influence of pressure drag could be assumed to be more significant. Although, the CFD results show still an increase in the resistance of the rudder and the other forces between the stall angles seem unaffected. So it is unlikely that a physical phenomenon is causing the negative drag coefficient.

To support this statement, the model forces drag forces plotted against the rudder angle, see figure 4.11, show an increase in drag for higher rudder angles. The most logical explanation for the negative drag coefficient

ficients of the rudder is an error in the towing tank tests. As is discussed in chapter 4, all error sources are excluded, except of crosstalk of the rudder, the effect of the shape of the rudder on the measurement results. Additional information is necessary to clarify this effect. Ideally, a test should be conducted on land, where two forces (drag and side forces) are applied on the rudder in the correct directions, for multiple rudder angles. In principle an entire drag and lift curve should be created using this method.

6.2.2. Lift part

The question to be answered here is first posed by Keuning et al. [32] and is the basis of this research, this is discussed in more detail in the Introduction and chapter 2. The problem is summarised in blue circles of figure 6.4. This subsection first continues with the comparison of the both results, before discussing the conclusions.

In the previous section, subsection 6.1.2, is explained that the curve of the CFD results seems to veer from the linear trend found between the $\delta = -10^\circ$ and $\delta = 5^\circ$, which could mean it stalls at the same locations as the experimental results. More insight in the lift curve from the CFD will be obtained when the wake is plotted.

Figure 6.13 shows the relative velocity around the rudder plotted on a number xy -planes intersecting the rudder, for -13° of rudder angle and 3° leeway with the keel fitted. In short, from the experiments stall behaviour is expected. This figure shows clearly separation around the rudder, thus stall behaviour.

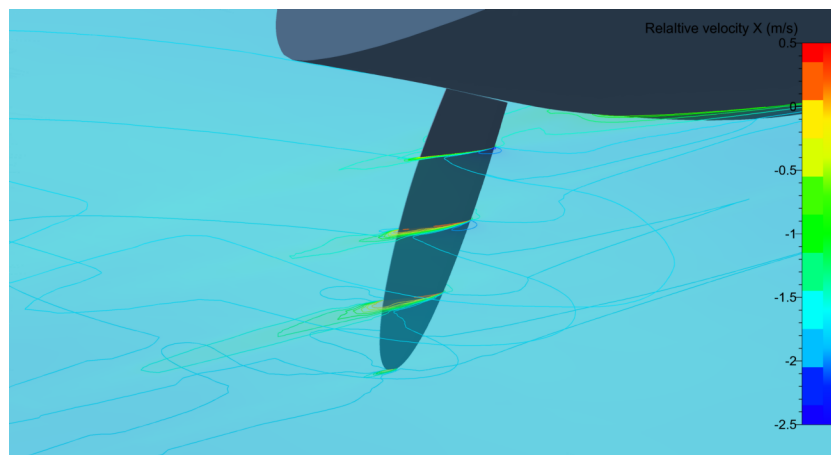


Figure 6.13: The velocity in x -direction over the rudder plotted on multiple xy -planes, for the test case with $\beta = 3^\circ$ and $\delta = -13^\circ$

The velocity around the rudder for test case of $\delta = 7^\circ$ is plotted in figure 6.14, where according to the experiments separation should also occur. This separation is identified in the third plane from the top, so stall behaviour can be assumed for these rudder angles.

Both statements are confirmed when comparing figures 6.15 and 6.16. These figures show the shear stress over the rudder, for the two cases mentioned above. For the first rudder angle the separation is confirmed, see figure 6.15. For the second rudder angle, a region of positive viscous stress is visible in figure 6.16, which indicates separation.

The rudder angles discussed here give indications for separated flow, e.g. stall. This supports the statement that both lift curves presented in figure 6.2 show similar behaviour and thus that the lift curve found in the experiments is correct.

The question arises whether there is a reason for the early stall behaviour. The expected location of stall should be in the order of 10° - 14° for a NACA 0009 airfoil, according to I. Abbott [20]. The exact angle of stall depends on the aspect ratio of the foil. I. Abbott [20] gives not the exact data of the aspect ratio of the rudder, so the stall angles only can be represented in a range. Further research is necessary to find the undisturbed stall angle of the rudder angle; ideally a towing tank test with only the rudder should be undertaken with multiple turbulence levels.

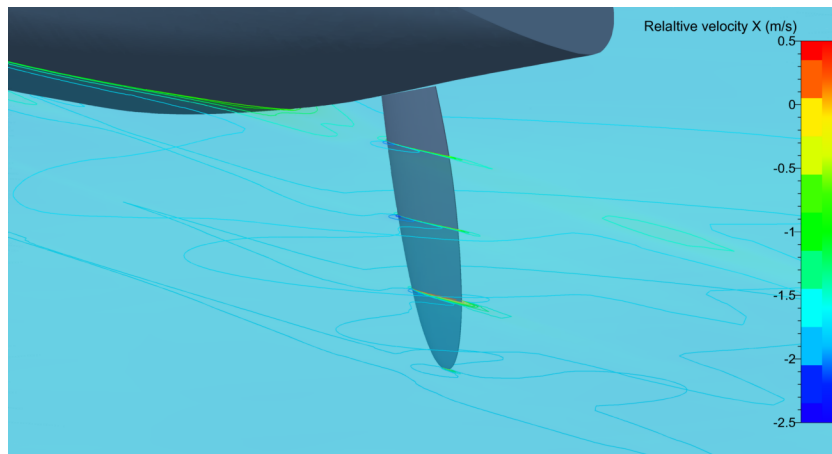


Figure 6.14: The velocity in x -direction over the rudder plotted on multiple xy -planes, for the test case with $\beta = 3^\circ$ and $\delta = 7^\circ$

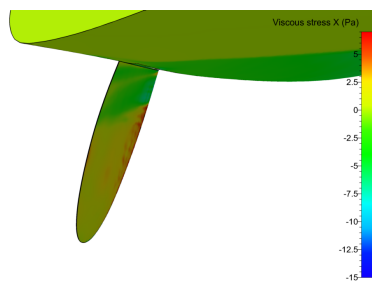


Figure 6.15: The viscous stress in x -direction over the rudder, for the test case with $\beta = 3^\circ$ and $\delta = -13^\circ$, seen from the starboard side.

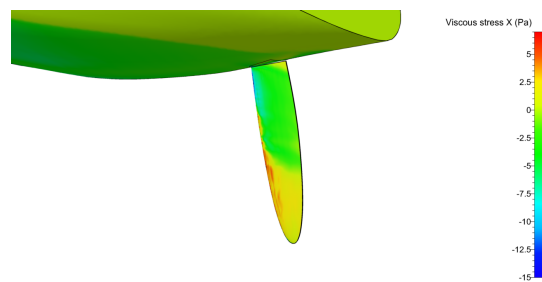


Figure 6.16: The viscous stress in x -direction over the rudder, for the test case with $\beta = 3^\circ$ and $\delta = 7^\circ$, seen from the port side.

From here on it is assumed that a stall angle of this rudder of 10° is the normal stall angle and originate from the adverse pressure gradients. This means that the stall angle for the negative rudder angles should be around normal, with only a degree of deviation (the downwash angle shifts the lift curve by 1.6°). During the rest of the section the focus will be on the positive side of the lift forces, as the stall angle here is decreased by multiple degrees.

Figures 6.17 and 6.18 show the relative velocity around the rudder for the test case of $\beta = 3^\circ$ and $\delta = -7^\circ$. In these figures the influence of the tip vortex of the can be seen, as well as the boundary layer of the hull. Both pass on the suction side of the rudder, because of the leeway angle. It seems that the vertical fluid structure above the tip vortex, seen from the forth cross-section from the front, is the upwash of the rudder, as this structure originates a little upstream of the rudder and is the strongest around the rudder. No other fluid structures, which could influence the pressure distribution around the rudder, are identified in these figures.

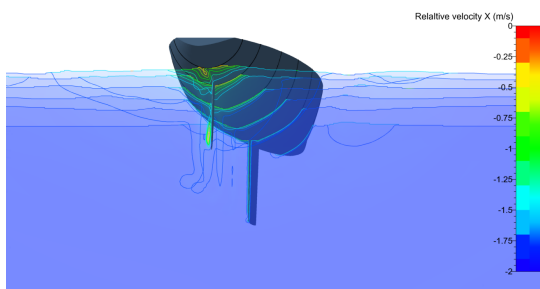


Figure 6.17: The velocity in x -direction plotted on multiple yz -planes, for the test case with $\beta = 3^\circ$ and $\delta = 7^\circ$

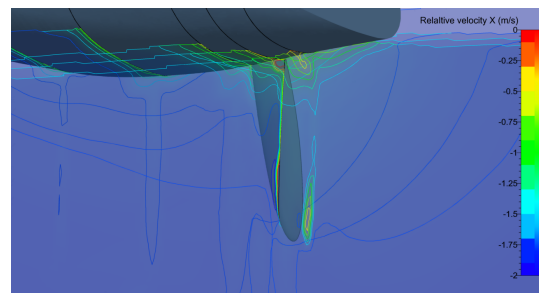


Figure 6.18: The velocity in x -direction plotted on multiple yz -planes, for the test case with $\beta = 3^\circ$ and $\delta = 7^\circ$

An interesting vortex structure is identified in figure 6.19; this figure shows the λ_2 -criterion, which locates vortex cores. Here two vertical vortex structures are seen next to the rudder. These structures are only found in the test cases with keel and only for the positive rudder angles. It is expected that these structures originate from the keel and interact with the low pressure side of the rudder.

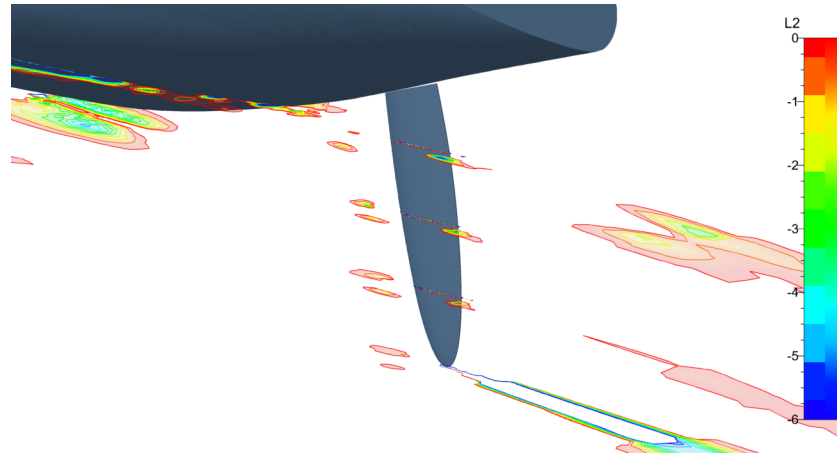


Figure 6.19: The λ_2 values to identify vortex structures plotted at a number of xy -planes. For test case $\beta = 3^\circ$ and $\delta = 5^\circ$

The low pressure could affect the pressure gradient on the rudder and induce stalling when these vertical vortex structures are strong enough. This would mean, however, that the structures should be visible for different variables.

In figure 6.20 the normalised velocity is plotted on the same xy -planes as the λ_2 of figure 6.19. In the plot of the normalised velocity two clear circles are seen in the isolines near the leading edge of the rudder, in which the flow velocity seems to increase slightly. These circles appear to be located in the same position as one of the vortex cores of 6.19.

As the assumed vortex cores seem to accelerate the flow, it should give a lower pressure. In figure 6.21 the dynamic pressure is plotted from the same point of view as the figures 6.19 and 6.20. The vortex core identified in the two previous figures is not visible in the plot of the dynamic pressure.

The vortex detected in the mentioned figures will probably have marginal influence on the pressure around the rudder. Whether it could initiate separation on the rudder is unclear.

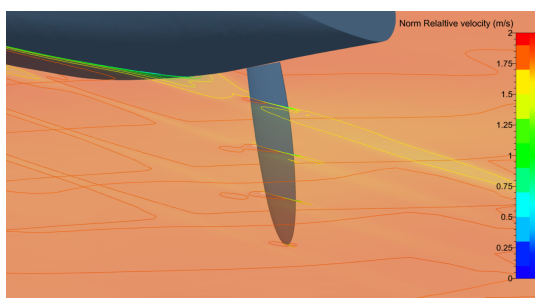


Figure 6.20: The normalised velocity plotted at a number of xy -planes. For test case $\beta = 3^\circ$ and $\delta = 5^\circ$

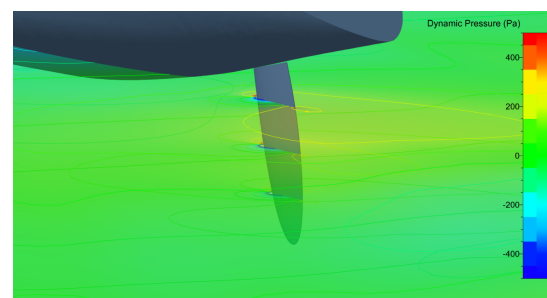


Figure 6.21: The dynamic pressure plotted at a number of xy -planes. For test case $\beta = 3^\circ$ and $\delta = 5^\circ$

An interesting addition to this analysis is to assess the stall behaviour of the rudder for the test cases without keel. In figure 6.3 the comparison between the CFD simulations and the towing tank experiments of the test case without keel is presented. In this figure, as discussed earlier, the CFD simulations seem to show stall behaviour at around 7° of rudder angle.

In figures 6.22 and 6.23 the shear stress on the rudder is presented for a rudder angle of 7° and 10° , respectively. These figures indicate that the rudder is not stalling at an angle of 7° , but is for an angle of 10° . From

this analysis it is not yet clear if the stall angle of the rudder for test case without keel is 7° , further research is necessary to clarify this. In the rest of the analysis can only be assumed that the stall angle lies between the 7° and the 10° rudder angle.

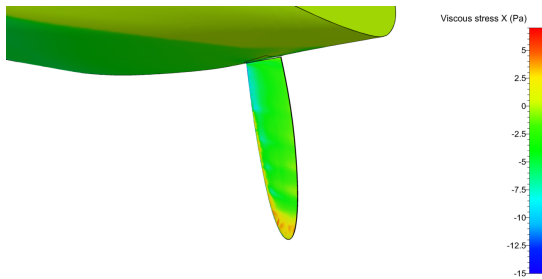


Figure 6.22: The shear stress in x -direction for test case without keel and a rudder angle 7° .

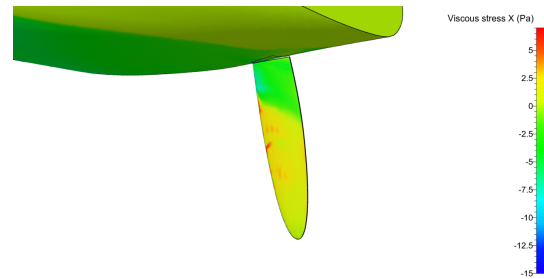


Figure 6.23: The shear stress in x -direction for test case without keel and a rudder angle 10° .

From the latter analysis it seems that the stall angle of the rudder for the test case without keel is decreased by a couple of degrees. So this leads to the possibility that the hull also contributes to a decrease in stall angle.

The normalised vorticity (figures 6.24 and 6.25) and the dynamic pressure (figure 6.26 and 6.27) are plotted in order to try to assess the difference between the test cases with and without keel. Note: the downwash angle is of importance as the angle of attack on the rudder for the case with keel is changed. About 1.6° should be added to the rudder angle of the case with keel, which means the magnitude of the parameters should be similar.

The normalised vorticity in figure 6.24 shows clearly more rotation in the wake than figure 6.25. The difference is in the amount of rotation the keel induces in the flow, a tip vortex and a kind of sheet vortex, which seems to decrease according to expectations. These do influence the low pressure side of the rudder for positive rudder angles. The boundary layer of the hull is the other rotation source in the wake.

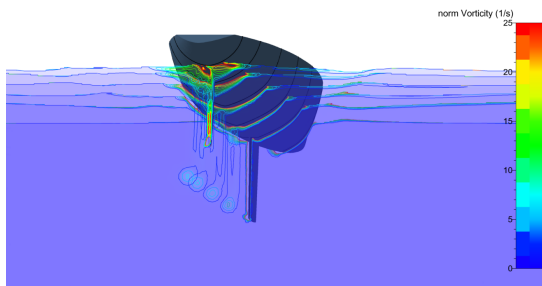


Figure 6.24: The normalised vorticity plotted on multiple yz -planes, for the test case with $\beta = 3^\circ$ and $\delta = 5^\circ$

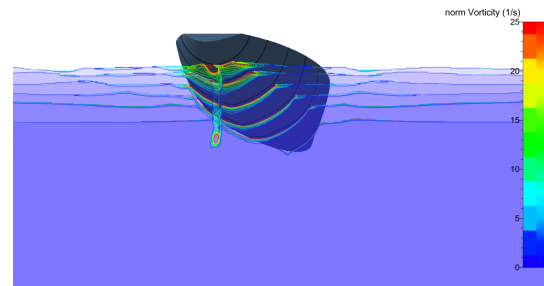


Figure 6.25: The normalised vorticity plotted on multiple yz -planes, for the test case with $\beta = 0^\circ$ and $\delta = 7^\circ$ and without keel

The effects of the hull and the keel on the pressure distribution are presented in figures 6.26 and 6.27. From the two figures can be seen that the keel seems to influence the low pressure side of the rudder. However, when the downwash angle is taken into account the difference appears small. It might be possible that the pressure is increased by a small amount for the test cases with keel. Further research is necessary to investigate the influence of the downwash angle and to assess the pressure distribution around the rudder.

To conclude the lift section:

- The lift curve found in the experiments is confirmed for a leeway angle of 3° and, for lesser extend, for the test case without keel and zero degree of leeway.
- There are indications that the hull and the keel influence the stall behaviour of the rudder, by decreasing the angle with a couple of degrees. From the CFD data in this study the rudder seems only to be affected

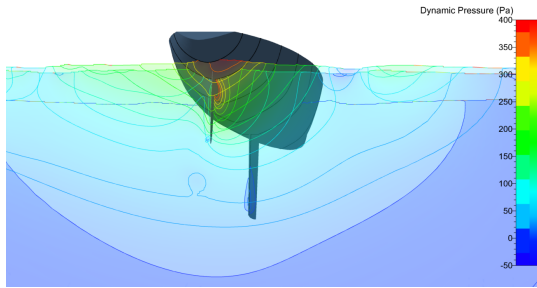


Figure 6.26: The dynamic pressure plotted on multiple yz -planes, for the test case with $\beta = 3^\circ$ and $\delta = 5^\circ$

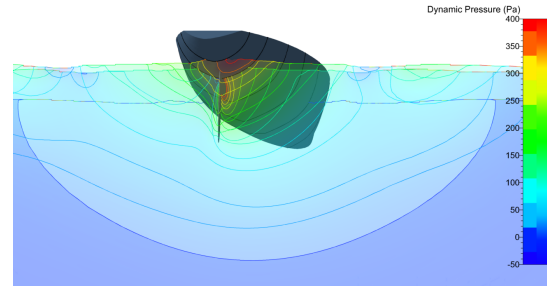


Figure 6.27: The dynamic pressure plotted on multiple yz -planes, for the test case with $\beta = 0^\circ$ and $\delta = 7^\circ$ and without keel.

when the disturbance of the keel and hull pass on the low pressure side. The magnitude of the influence of the keel and hull cannot be determined from the data available. Further research is necessary to clarify this. In particular the test on the crosstalk of the rudder, proposed in section 6.2.1, would be important. As well as a towing tank test series with only the rudder to determine the undisturbed stall angle. In addition to these experiments are more CFD simulations necessary.

- The exact physical effect which is behind the decreasing stall angle is not identified in this study. There are indications that the vorticity of the keel has some influence. Again further research is necessary. Ideally, a study where the influence of important parameters could be isolated.

Conclusions and recommendations

The goal of this study was to clarify some interesting results Keuning et al. [32] found back in 2007. Based on the outcome of this study; it can be said that this was only partially achieved.

The results of the towing tank experiments, conducted in this study, show similarities to the previous experiments of Keuning et al. [32]. The negative stall angle is repetitious; this substantiates the argument that the phenomenon is physical.

The differences found in this comparison raise the questions on the correctness of either of the experiments.

From the current CLR experiments the following is observed:

- The experiments are executed with little errors and the components were aligned to satisfaction.
- A negative drag coefficient for the rudder, for all the test cases, for rudder angles outside the stall angles.
- An asymmetric stall behaviour of the rudder for all the test cases. For the positive rudder angles the rudder stalls roughly 3° sooner than for the negative rudder angles.

Regarding the comparison of the forces between the two types of experiments for the lift, drag curves and the position of the CLR, the following is concluded:

- Comparisons between the CFD simulations and experiments are positive. The results for the model are similar and for the rudder the results are similar between the stall angles.
- The drag curve of the rudder, for rudder angles outside the stall angles, show a difference between the CFD results and the experiments.
- The lift curve the CFD confirms stall behaviour of the rudder around the stall angles found by the experiments.
- The position of the CLR of the experiments, after the stall angles, decreases quickly. Whereas the CLR of the CFD simulations does not change in magnitude. Expected is that the CLR of the experiments is incorrect.

In chapter 6 the analysis of the lift and drag are discussed separately. The conclusions are discussed in the same manner, in this paragraph.

No reasonable physical explanation for the negative drag coefficient of the rudder found in this study. The most likely explanation is an error in the set-up of the rudder. As the model forces from the experiments and the CFD simulations indicate an positive drag coefficient. The error source should be found in the shape of the rudder blade and the way the rudder is supported, as all other error sources are excluded. Further research is necessary, the proposed method is discussed in the recommendations.

The conclusions for the shape of the lift curve are as follows:

- The lift curve found in the experiments is confirmed for a leeway angle of 3° and, for lesser extend, for the test case without keel and zero degree of leeway.
- There are indications that the hull and keel influence the stall behaviour of the rudder, by decreasing the angle with a couple of degrees. From the CFD data in this study the rudder seems only be affected when the disturbance of the keel and hull pass on the low pressure side. The magnitude of the influence of the keel and hull cannot be determined from the data available. Further research is necessary to clarify this.
- The exact physical effect which is behind the decreasing stall angle is not identified in this study. There are indications that the vorticity of the keel has some influence. Again further research is necessary.

See the recommendations, section 7.1, for more information on the proposed further research.

In the introduction a main question and hypothesis are formulated.

The main question was: What physical phenomenon is at the basis of the asymmetric stalling behaviour on the rudder of a sailing yacht? The hypothesis posed to this question: "Expected is that this phenomenon is caused by a flow interaction of the keel tip vortex on the low pressure side of the rudder.". Whether this hypothesis is correct cannot be confirmed with certainty. As mentioned in this chapter and chapter 6, are there indications for the case of 3° leeway that the rudder is influence by the keel for positive rudder angles. However, there are also indications that the hull has a similar influence. The CFD results do not give a definite answer.

In short: this study, unfortunately, does not clarify the results found by Keuning et al. [32], but raises more questions.

In the sub-questions (see the Introduction) an important question is posed: Are CFD simulations an useful tool to assess the problem?

The formulated answer is: It definitely is a helpful tool, especially for difficult wake body interaction, as it gives some insight in the flow. As was showed in this study. However, it is also a difficult tool. When settings are not entirely correct; the results still can appear correct, while they probably are not, and false conclusions could be drawn from it. In addition it is questionable if RANS codes at this moment are capable of modelling a complex wake to a high enough accuracy. CFD simulations are becoming a more important tool in hydrodynamic analysis and in the future, when computer power increases and CFD codes improve, will CFD simulations be even more useful and reliable.

7.1. Recommendations

In the outcome of this study a number of uncertainties are found, as described in for example the previous section. This section proposes some recommendations based on the outcomes of this study.

The main recommendation, and the first thing to take on, is a dry test of the rudder set-up, to investigate crosstalk in the set-up: the influence of the moments of the rudder on the measurements. The set-up of the rudder needs to be recreated, ideally without hull; then forces should be applied on the centre of lateral resistance of the rudder in the correct directions. The idea is to create an entire lift and drag curve for the rudder with these tests.

Expected is that this test will clarify a lot of uncertainties in the results of the experiments. When these uncertainties are clarified a new view will be presented on conclusions. The behaviour of the lift and drag curves and will help to draw better conclusions on the results presented in this report.

A second important recommendation is a test with only the rudder fitted. This test is meant to give more insight in the undisturbed stall angle of the rudder. In addition would it be interesting to see the effect of the roughness on the rudder on the performance of the rudder.

As with the previous recommendation, the answers from the recommendation proposed here would be essential for some conclusions of this study.

One of the conclusions of the towing tank experiments was the following: "The differences found in this comparison raise the questions on the correctness of either of the experiments." See chapter 4 and chapter 7. The comparison discussed here is the comparison between the results of Keuning et al. [32] and the results of this study.

When the data of this study will be used for further research, the correctness of this study should be checked, especially at the locations which deviates from the results found by Keuning et al. [32]. The correctness can be checked by conducting towing tank experiments with the same set-up. The first recommendation is important to take into account when recreating these tests.

The remaining recommendations on the towing tank experiments are summarised in the following enumeration:

- Similar towing tank tests with a different model and appendages.
- When new tests are executed care should be taken to minimise undesirable flow in the towing tank.
- The influence of turbulence on the appendages and an assessment on the correctness of the used turbulence stimulators on the appendages.
- Test with flow visualisation methods, like PIV or dye. This would also be a important addition for the validation of the CFD results.

The final recommendations are recommendations on the CFD simulations. These are summerised in the following three statements:

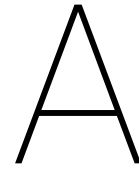
- More simulations are necessary to confirm the assumptions that were made in the CFD analysis. It is also suggested that more without keel and additional leeway angles should be performed.
- The effect of different turbulence models and boundary conditions on the wake would be interesting, especially in the verification of the CFD models.
- In the future, when computer power or facilities increase, it would be interesting to see the flow in the wake simulated by LES models.

Bibliography

- [1] Ronald L. Allen and Duncan Mills. *Signal Analysis: Time, Frequency, Scale, and Structure*. Wiley-Interscience-IEEE, 2004.
- [2] *Maxsurf Link, User Manual*. Bentley Systems, Incorporated, 2014.
- [3] International Towing Tank Conference. Ittc – recommended procedures and guidelines. In *Practical Guidelines for Ship CFD Applications*, 2014.
- [4] T.J. Craft, A.V. Gerasimov, H. Iacovides, and B.E. Launder. Progress in the generalization of wall-function treatments. Technical report, UMIST, 2002.
- [5] Barbara d'Aure, Benoit Mallol, and Charles Hirsch. Resistance and seakeeping cfd simulations for the korean container ship. Technical report, NUMECA Int., Belgium, 2015.
- [6] G. Deng, E. Guilmineau, P. Queutey, M. Visonneau, J. Wackers, and A. del Toro Llorens. Verification and validation of resistance and propulsion computation. Technical report, ECN-LHEEA, CNRS, Spanish Institution of Civil Engineers, 2015.
- [7] Gano Deng and Michel Visonneau. On the prediction of swirling induced recirculation. Technical report, Ecole Centrale de Nantes, 2003.
- [8] G.B. Deng, P. Queutey, and M. Visonneau. A code verification exercise for the unstructured finite-volume cfd solver isis-cfd. Technical report, Ecole Centrale de Nantes, 2006.
- [9] William J. Devenport, Michael C. Rife, Stergios I. Liapis, and Gordon J. Follin. The structure and development of a wing-tip vortex. Technical report, Virginia Polytechnic Institute and State University, November 1995.
- [10] L. Eça and M. Hoekstra. Verification and validation for marine applications of cfd. Technical report, Instituto Superior Técnico and Maritime Research Institute Netherlands, 2013.
- [11] L. Eça and M. Hoekstra. A procedure for the estimation of the numerical uncertainty of cfd calculations based on grid refinement studies. Technical report, Instituto Superior Técnico and Maritime Research Institute Netherlands, 2014.
- [12] J.H. Ferziger and M. Perić. *Computational Methods for Fluid Dynamics*. Springer, 2002.
- [13] P.H. Gaskell and A.K.C. Lau. Curvature-compensated convective transport: Smart, a new boundedness preserving transport algorithm. Technical report, University of Leeds, 1988.
- [14] T.B. Gatski and C.G. Speziale. On explicit algebraic stress models for complex turbulent flows. Technical report, NASA, 1993.
- [15] Marc Gerritsma. Personal Communication, November 2017.
- [16] Prof. Ir. J. Gerritsma. Vinkielen en roeren van zeiljachten. Technical report, Technische hogeschool Delft, 1971.
- [17] S.F. Hoerner. *Fluid-Dynamic Drag*. S.F. Hoerner, 1965.
- [18] S.J. Hulshoff. *CFD II Part 2: Computation and Modelling of Turbulence*. TU Delft, April 2015.
- [19] J.C.R. Hunt, A.A. Wray, and P. Moin. Eddies, streams and convergence zones in turbulent flows. Technical report, University of Cambridge and NASA, 1988.
- [20] L. Stivers I. Abbott, A. Von Doenhoff. Summary of airfoil data. Technical report, National Advisory committee for Aeronautics, 1945.

- [21] Northern Digital Inc. Optotrak certus, 2018. URL <https://www.ndigital.com/msci/products/optotrak-certus/>.
- [22] NUMECA International. Personal Communication, September 2018.
- [23] *Resistance Test*. ITTC, 7.5-02-02-01 edition, 2011.
- [24] *Example for Uncertainty Analysis in Resistance Tests*. ITTC, 7.5-02-02-02.1 edition, 2014.
- [25] *General Guideline for Uncertainty Analysis in Resistance Tests*. ITTC, 7.5-02-02-02 edition, 2014.
- [26] Hrvoje Jasak. *Error Analysis and Estimation for the Finite Volume Methode with Applications to Fluid Flows*. PhD thesis, University of London, 1996.
- [27] Jinhee Jeong and Fazle Hussain. On the identification of a vortex. Technical report, University of Houston, 1994.
- [28] T. Jongen and T.B. Gatski. General explicit algebraic stress relations and best approximation for three-dimensional flows. Technical report, Swiss Federal Institute of Technology and NASA, 1997.
- [29] J.A. Keuning and B.J. Binkhorst. Appendage resistance of a sailing yacht hull. Technical report, TU Delft, 1997.
- [30] J.A. Keuning and K.J. Vermeulen. The yaw balance of sailing yachts upright and heeled. Technical report, Delft University of Technology, 2003.
- [31] J.A. Keuning, K.J. Vermeulen, and E.J. de Ridder. A generic mathematical model for the maneuvering and tacking of a sailing yacht. Technical report, Delft University of Technology, 2005.
- [32] J.A. Keuning, M. Katgert, and K.J. Vermeulen. Further analysis of the forces on keel and rudder of a sailing yacht. Technical report, Delft University of Technology, 2007.
- [33] Pijush K. Kundu, Ira M. Cohen, and David R. Dowling. *Fluid Mechanics*. Elsevier, sixth edition, 2016.
- [34] Lars Larsson and Hoyte C. Raven. *Ship Resistance and Flow*. The Society of Naval Architects and Marine Engineers, 2010.
- [35] B. Launder and N. Sandham. *Closure Strategies for Turbulent and Transitional Flows*, chapter Linear and Nonlinear Eddy Viscosity Modelling. Cambridge University Press, 2002.
- [36] B.P. Leonard. Simple high-accuracy resilution program for convective modelling of discontinuities. Technical report, University of Akron and NASA-Lewis Research Center, 1988.
- [37] E.V. Lewis, editor. *Principles of Naval Architecture*, volume III, Motions in Waves and Controllability. The Society of Naval Architects and Marine Engineers, 1989.
- [38] D.A. Lovell. A low-speed wind-tunnel investigation of the tailplane effectiveness of a model representing the airbus type of aircraft. Technical report, Aerodynamics Dept., R.A.E., Farnborough, 1969.
- [39] *Numerical uncertainty analysis-User manual*. MARIN, August 2017.
- [40] Florian R. Menter. Improved two-equation $k-\omega$ turbulence models for aerodynamic flows. Technical report, NASA, 1992.
- [41] Peter A. Monkewitz, Kapil A. Chauhan, and Hassan M. Nagib. Comparison of mean flow similarity laws in zero pressure gradient turbulent boundary layers. *Physics of Fluids*, 20, 2008.
- [42] F. Moukalled, L. Mangani, and M. Darwish. *The Finite Volume Method in Computational Fluid Dynamics*. Springer, 2016.
- [43] Centrale Nantes and CNRS. Theoretical manual, isis-cfd v6.2. Technical report, NUMECA international, 2017.
- [44] J.N. Newman. *Marine Hydrodynamics*. The MIT Press, 1977.

-
- [45] K. Nomoto and H. Tatano. Balance of helm of sailing yachts. Technical report, University of Osaka, Department of Naval Architecture, 1979.
- [46] *NUMECA Online Documentation Platform: FINE™/Marine 7.1*. NUMECA international, 2017.
- [47] *User Guide HEXPRESS 7.2*. NUMECA International, 2018.
- [48] Stephen B. Pope. *Turbulent Flows*. Cambridge University Press, 2000.
- [49] P.J. Roach. Quantification of uncertainty in computational fluid dynamics. Technical report, Ecodynamics research associates, 1997.
- [50] *Rhinoceros 5, User's Guide*. Robert McNeel and Associates, Aug 2014.
- [51] Philippe R. Spalart. Detached-eddy simulation. Technical report, Boeing Commercial Airplanes, 2009.
- [52] D.B. Spalding. A single formula for the "law of the wall". *J. Appl. Mech.*, 28:455–457, 1961.
- [53] Ir. J.J. van den Bosch and Ir. J.A. Pinkster. Visualization of the effect of some turbulence stimulators. Technical report, TU Delft, January 1971.
- [54] Nico van der Kolk. Personal Communication, September 2018.
- [55] Gabriel D. Weymouth. Marine hydrodynamics: Viscous flow and boundary layers. Reader of University of Southampton SESS3023, Feb 2016.
- [56] Frank M. White. *Viscous Fluid Flow*. McGraw-Hill Education, 2006.



Computational Fluid Dynamics

In Computed Fluid Dynamics (CFD) there are a number of methods and variations to methods. This section gives a short description of the possible methods and then elaborates on workings of the RANS codes. This section is meant to inform readers who are not familiar with CFD and RANS codes.

There are a number of CFD methods available:

1. Direct Numerical Simulation (DNS)
2. Large Eddy Simulation (LES)
3. Reynolds Averaged Navier-Stokes Equations (RANS/RANSE)
4. Detached Eddy Simulations (DES)
5. Potential codes

The latter (potential codes) is based on an irrotational, inviscid flow and is mostly used to approximate the wave system around an object. The other methods are all viscous flow solvers. DNS (Direct Numerical Simulation) solves all the flow scales directly, with a turbulent flow, this means that the smallest vortices or flow elements need to be solved directly. This requires a fine grid and a lot of computer power. This method is still only usable for small physical problems, like an open lid flow. LES (Large Eddy Simulation); the method is in the name, this method only simulates the largest eddies (vortices) and models the smaller eddies, with the use of eddy viscosity models. In doing so the grid can be much larger than for DNS. This means that the method is more applicable to engineering problems, although it is still difficult to model a complete ship with this method. RANS (Reynolds Averaged Navier-Stokes Equations) is the most simplified method of the viscous flow solvers. In RANS the turbulence in the flow is modelled entirely, introducing possible uncertainties in the turbulent flow structures. For the RANS methods the Navier-Stokes Equations are averaged, the derivations of these equations are discussed in the next section [18], [34].

A.1. Derivation of the RANS equations

As the name suggest the governing equations for the RANS codes are averaged Navier-Stokes equations (NS equations). As said above the NS equations are only iterative solvable, in RANS there is tried to average out the turbulence and add a mathematical model for the variation in turbulence. In this section the derivation of the incompressible NS equations will be shown. The compressible NS equations will not be of importance, because the flow is assumed to be incompressible.

Started is with the incompressible Navier-Stokes equations:

$$\frac{D\vec{u}}{Dt} = \frac{1}{\rho} \frac{\partial p}{\partial x} + \nu \nabla^2 \vec{u} + \vec{F} \quad (\text{A.1})$$

Where, u is the flow velocity, p the pressure and F are external forces. This equation can also be written in Einstein notation, which leads to the following

$$\frac{\partial u_i}{\partial t} + u_j \frac{\partial u_i}{\partial x_j} = -\frac{1}{\rho} \frac{\partial p}{\partial x_j} + \nu \frac{\partial^2 u_j}{\partial x_j^2} + F_i \quad (\text{A.2})$$

In this derivation is assumed that the parameters consist of a mean and a fluctuating part, as can be seen in equation A.3. Equation A.3 also shows that only two parameters vary in the NSE and the rest is assumed to be constant.

$$u = \bar{u} + u' \quad (\text{A.3})$$

$$p = \bar{p} + p' \quad (\text{A.4})$$

In the end NSE will be averaged over time, this happens when the above assumed parameters are substituted. This means that the parameters of equation A.3 will be averaged, for this the following assumptions are made:

$$\bar{\bar{u}} = \bar{u} \quad \bar{u}' = 0 \quad (\text{A.5})$$

$$\bar{\bar{p}} = \bar{p} \quad \bar{p}' = 0 \quad (\text{A.6})$$

When the above is substituted into the NSE the following can be found:

$$\frac{\partial \bar{u}_i}{\partial t} + \frac{\partial}{\partial x_j} (\bar{u}_j \bar{u}_i) + \frac{\partial}{\partial x_j} (\bar{u}'_j \bar{u}'_i) = -\frac{1}{\rho} \frac{\partial \bar{p}}{\partial x_j} + \nu \frac{\partial^2 \bar{u}_j}{\partial x_j^2} + \bar{F}_i \quad (\text{A.7})$$

Or, when is assumed that $\nu \frac{\partial^2 \bar{u}_j}{\partial x_j^2} = 2\mu \bar{S}_{ij}$.

$$\frac{\partial \bar{u}_i}{\partial t} + \frac{\partial}{\partial x_j} (\bar{u}_j \bar{u}_i) = -\frac{1}{\rho} \frac{\partial \bar{p}}{\partial x_j} + -\frac{1}{\rho} \frac{\partial}{\partial x_j} (2\mu \bar{S}_{ij} + R s_{ij}) \quad (\text{A.8})$$

In equation A.8; \bar{S}_{ij} is the strain rate tensor and the $R s_{ij}$ is the Reynold stress tensor, these are summarised below.

$$\bar{S}_{ij} = \frac{1}{2} \left(\frac{\partial \bar{u}_i}{\partial x_j} + \frac{\partial \bar{u}_j}{\partial x_i} \right) \quad R s_{ij} = R s_{ji} = \rho \bar{u}'_j \bar{u}'_i \quad (\text{A.9})$$

Finally, the RANS equations in vector form.

$$\frac{D\bar{\mathbf{u}}}{Dt} = -\frac{1}{\rho} \nabla p + \frac{1}{\rho} \nabla (2\mu \mathbf{S} + \mathbf{R}\mathbf{s}) \quad (\text{A.10})$$

The problem with modelling these RANS equations, is the Reynold stress tensor. This tensor consists of a non-linearity and thus needs to be modelled, this modelling is often also called turbulence modelling. For this turbulence modelling a number of solutions are to be thought, which are discussed in section A.2 [33], [34].

A.2. Turbulence modelling

Turbulence modelling is an important aspect of RANS simulations. Larsson and Raven [34], give a nice overview of the possibilities in turbulence modelling for RANS. In total there are five different classes of turbulent models, all empirical.

1. Zero-equation models
2. One-equation models
3. Two-equation models
4. Algebraic Stress Models
5. Reynolds Stress Models

The first three mentioned are all based on the Boussinesq assumption, which states that the Reynolds Stress tensor (Rs_{ij}) should have the same properties as the strain rate tensor (S_{ij}), i.e. Rs_{ii} should be zero when S_{ii} is zero. In addition to this the Reynolds stress tensor could be seen as twice the turbulent kinetic energy per unit mass, i.e. $Rs = -2\rho k$. Resulting in the following equation for the Boussinesq approach of the Reynolds stress tensor:

$$Rs_{ij} = \mu_T S_{ij} - \frac{2}{3} \rho k \delta_{ij} \quad (\text{A.11})$$

With δ_{ij} being the Kronecker delta.

In contrast, stress models use non-linear models in the turbulence modelling. The Boussinesq approach assumes that the strain rate tensor and the Reynolds stress tensor are proportional. This is true for viscous stress, but questionable for turbulent stress, which does not originate from molecular activity. In the stress models this is solved by extending the Boussinesq approach [34].

The Reynolds stress model uses six transport equations for each of the six directions. These equations often require further equations in order to be able to model the first set. Algebraic stress models are based on transport equations for the individual Reynolds stresses, each PDE with respect to the stress is modelled algebraically. The complexity of the model depends on the modelling, which usually have a connection with the two-equation models.

A final turbulence model available in NUMECA [46] is DES (Detached Eddy Simulation), this is a combination of a RANS model and LES. Near the wall, where the circulations are small, the flow is modelled with a RANS method. This method is then match to a LES model which models the flow further out in the domain. This method could improve the results compared to the results of a RANS method. Although, matching the two models is often difficult and could lead to abrupt changes from RANS to LES.

A.3. Discretisation

The goal in CFD is to numerically solve the Navier-Stokes equations. In the sections above the averaging of the Navier-Stokes equations and the turbulence modelling are already discussed. Another aspect of numerically solving a fluid flow is the discretisation of the domain. This is done so the fluid around an object can be calculated using the RANS equations. The domain will be divided into a number of cells and in each of these cells the RANS equations are solved.

A number of different methods of tackling this discretisation is used. Of the most common are Finite Differences, Finite Elements methods (the model for numerical structure calculations) and Finite Volume methods. NUMECA [46] is using the finite volume method, so this method will be discussed here. It is also the most common discretisation method for CFD [34].

In the finite volume method the different cells can be seen as separate control volumes. At each of these control volumes the integral form of the conservation equations is used. As the values are presented in the cell faces an approximation is necessary to calculate the values in the cell centre, this is also true for other locations other than the cell centre.

As the control volumes are linked the determination of the values in the cell are depended on the surrounding cells. Here, the discretisation methods, like upwind differencing, come into play. These methods determine the values on a cell face, with the use of the conservation equation this value is then used to calculate a value in the cell centre or on the downwind cell face.

Examples of these methods are upwind differencing, where the value of the upwind cell is used as a value on the new cell face, this method is first order accurate. Central differencing scheme is a second order accurate, as this method uses the a linear interpolation between two cell centres to find a value for the face in between these centres [12].

The free-surface method used in NUMECA [46] is the volume of fluid (VOF) method. The VOF method locates the cell where a mixture is present between air and water. Determination of the parameters of the fluid is based on the distribution of air and water.

One of the methods to determine the pressure in a simulation is to use the continuity and momentum equations. As the momentum equations are used to determine the velocities, the continuity equation will be used for the determination of the pressure. According to Ferziger and Perić [12] this is done by combining the two

equations and to take the divergence from the combination. Resulting in the following equation for the pressure [12].

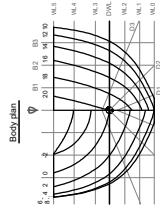
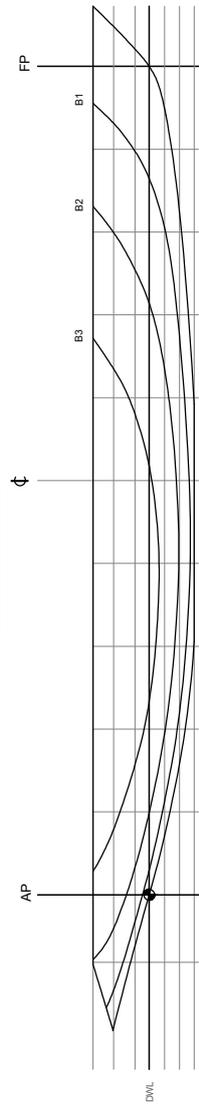
$$\frac{\partial}{\partial x_i} \left(\frac{\partial p}{\partial x_i} \right) = - \frac{\partial}{\partial x_i} \left(\frac{\partial (\rho u_i u_j)}{\partial x_j} \right) \quad (\text{A.12})$$

For further information on these subjects is referred to the following references: Ferziger and Perić [12], Pope [48], Larsson and Raven [34], Hulshoff [18] and Kundu et al. [33].

B

Lines plan

PROFILE PLAN



HYDROSTATIC DATA

Loa	3.39	m
Lwl	2.74	m
Boa	1.5	m
Bwl	0.49	m
Tc	0.15	m
Vc	0.07	m ³
Cp	0.53	

Paper size: A4 Scale: 1:20

TU Delft

Project: TUD-366 Lines plan
 Drawing No.:
 Sheet number: 1

C

Original test matrices

Carboniumstrips single

Run	Fn [-]	Vs [m/s]	Z [mm]	Trim [deg]
2	0.1	0.52	0.00	0.00
4	0.15	0.78	-1.40	0.02
6	0.2	1.04	4.28	0.00
8	0.25	1.30	-8.06	0.01
10	0.3	1.56	-13.28	0.06
12	0.35	1.81	-20.88	0.21
14	0.4	2.07	-31.23	0.77
16	0.45	2.33	-39.60	1.66
18	0.5	2.59	-41.27	2.44
20	0.55	2.85	-39.01	3.04
22	0.6	3.11	-33.40	3.41

Carboniumstrips double

Run	Fn [-]	Vs [m/s]	Z [mm]	Trim [deg]
22	0.1	0.52	0.00	0.00
24	0.15	0.78	-1.40	0.02
26	0.2	1.04	4.28	0.00
28	0.25	1.30	-8.06	0.01
30	0.3	1.56	-13.28	0.06
32	0.35	1.81	-20.88	0.21
34	0.4	2.07	-31.23	0.77
36	0.45	2.33	-39.60	1.66
38	0.5	2.59	-41.27	2.44
40	0.55	2.85	-39.01	3.04
42	0.6	3.11	-33.40	3.41

Figure C.1: The initial test matrix for the configuration with keel 1. This test matrix is expanded during the experiments, due to the findings of the experiments.

Roer+Kiel 1 tests						
Run	V [m/s]	Phi [deg]	Beta [deg]	Z [mm]	Trim [deg]	Delta [deg]
102	1.8	0	3	-20.86	0.21	-5
104	1.8	0	3	-20.86	0.21	-7
106	1.8	0	3	-20.86	0.21	-9
108	1.8	0	3	-20.86	0.21	-10
110	1.8	0	3	-20.86	0.21	-11
112	1.8	0	3	-20.86	0.21	-13
114	1.8	0	3	-20.86	0.21	-15
116	1.8	0	6	-20.86	0.21	-5
118	1.8	0	6	-20.86	0.21	-7
120	1.8	0	6	-20.86	0.21	-9
122	1.8	0	6	-20.86	0.21	-10
124	1.8	0	6	-20.86	0.21	-11
126	1.8	0	6	-20.86	0.21	-13
128	1.8	0	6	-20.86	0.21	-15
130	1.8	0	9	-20.86	0.21	-5
132	1.8	0	9	-20.86	0.21	-7
134	1.8	0	9	-20.86	0.21	-9
136	1.8	0	9	-20.86	0.21	-10
138	1.8	0	9	-20.86	0.21	-11
140	1.8	0	9	-20.86	0.21	-13
142	1.8	0	9	-20.86	0.21	-15
144	1.8	0	0	-20.86	0.21	-5
146	1.8	0	0	-20.86	0.21	-7
148	1.8	0	0	-20.86	0.21	-9
150	1.8	0	0	-20.86	0.21	-10
152	1.8	0	0	-20.86	0.21	-11
154	1.8	0	0	-20.86	0.21	-13
156	1.8	0	0	-20.86	0.21	-15
158	1.8	0	-3	-20.86	0.21	-5
160	1.8	0	-3	-20.86	0.21	-7
162	1.8	0	-3	-20.86	0.21	-9
164	1.8	0	-3	-20.86	0.21	-10
166	1.8	0	-3	-20.86	0.21	-11
168	1.8	0	-3	-20.86	0.21	-13
170	1.8	0	-3	-20.86	0.21	-15

Figure C.2: The initial test matrix for the configuration with keel 1. This test matrix is expanded during the experiments, due to the findings of the experiments.

D

Results of the experiments

D.1. Hull related plots

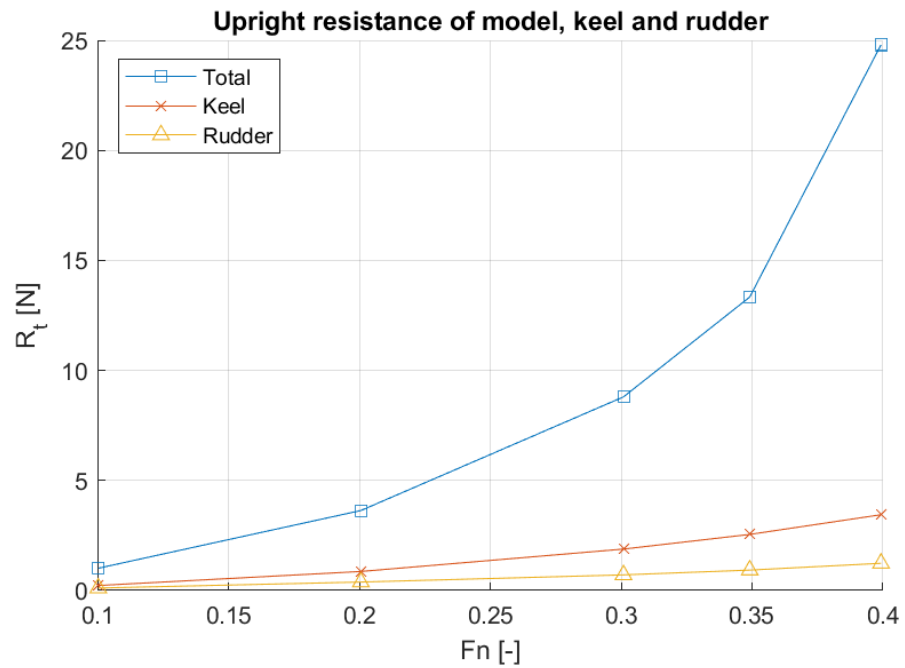


Figure D.1: The resistance curve for the model, keel and rudder measured at 5 different speeds.

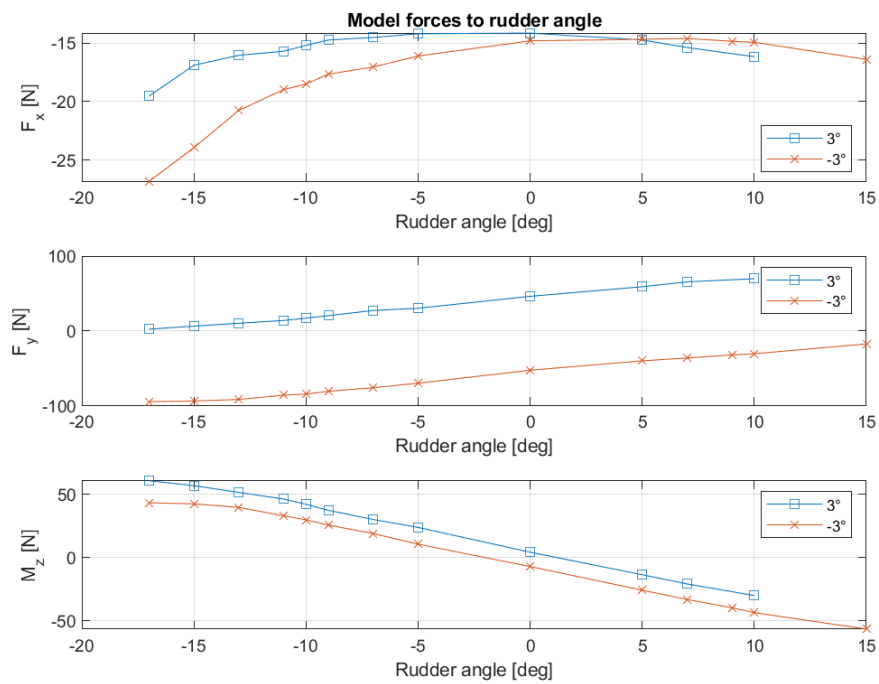


Figure D.2: The drag force, side force and yaw moment of the test case with 3° and -3° yaw angle.

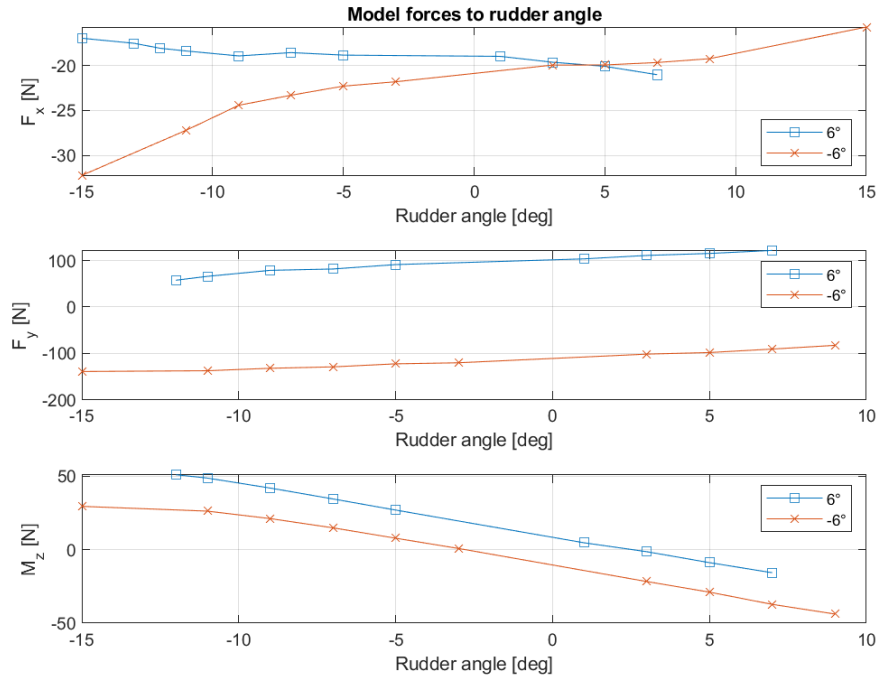


Figure D.3: The drag force, side force and yaw moment of the test case with 6° and -6° yaw angle.

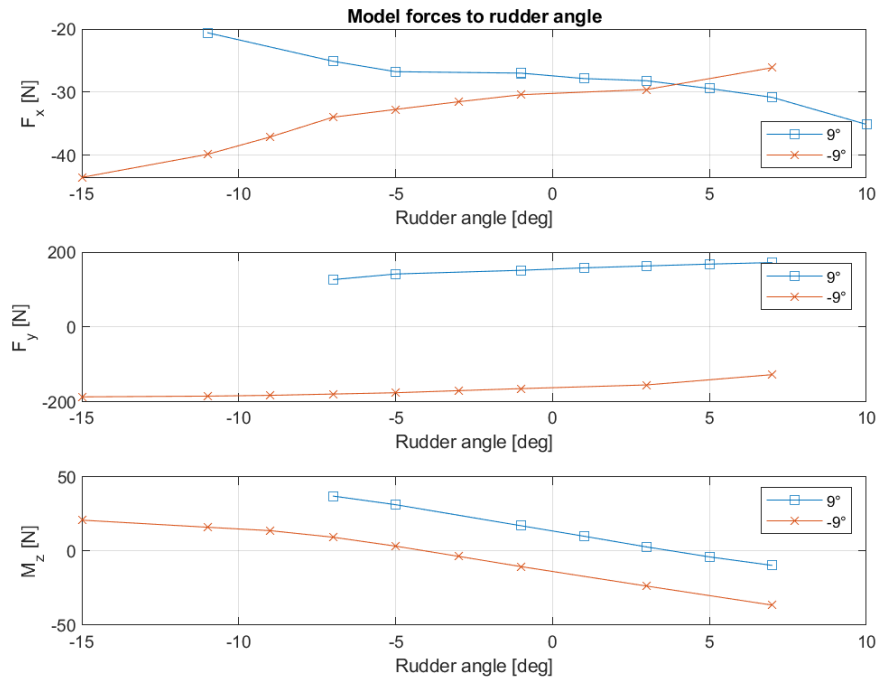


Figure D.4: The drag force, side force and yaw moment of the test case with 9° and -9° yaw angle.

D.2. Keel related plots

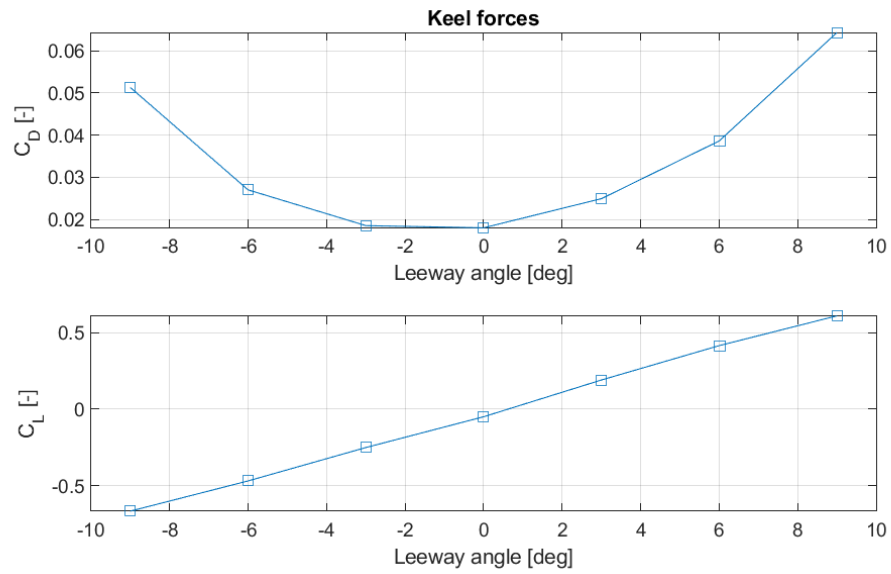


Figure D.5: The lift and drag of the keel in earth fixed coordinate system.

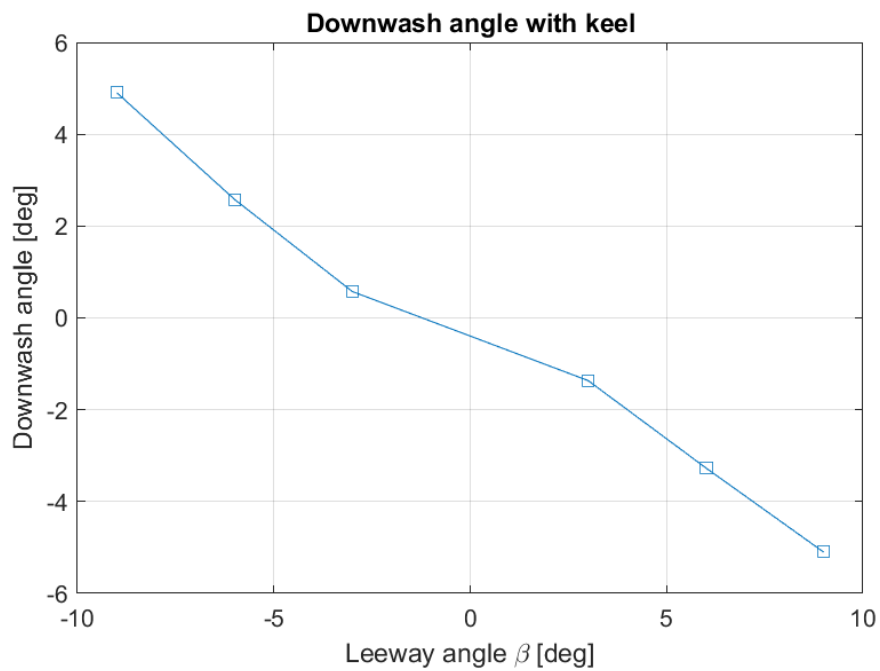


Figure D.6: The downwash of the keel on to the rudder.

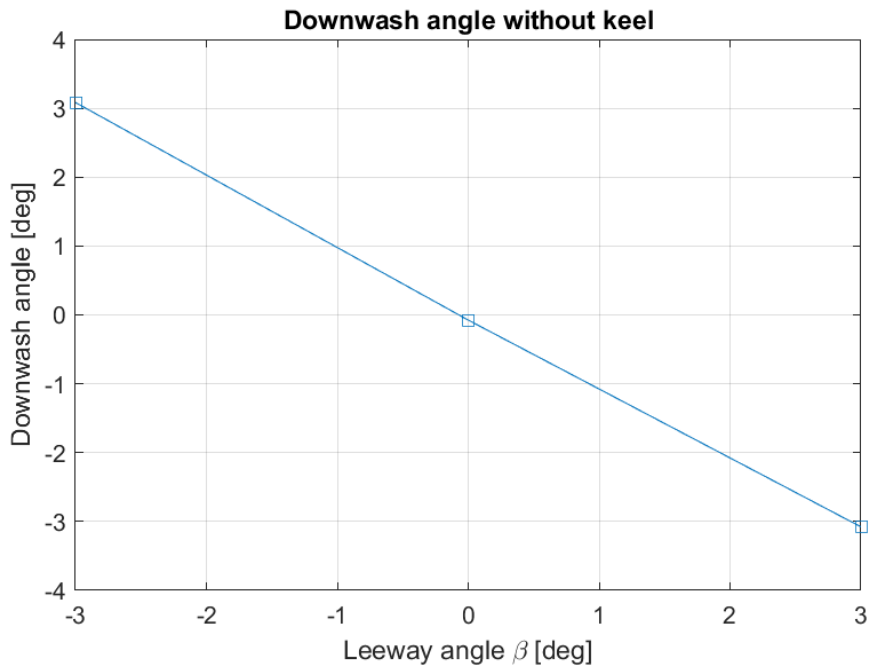


Figure D.7: The downwash angle without keel on to the rudder.

D.3. Rudder related plots

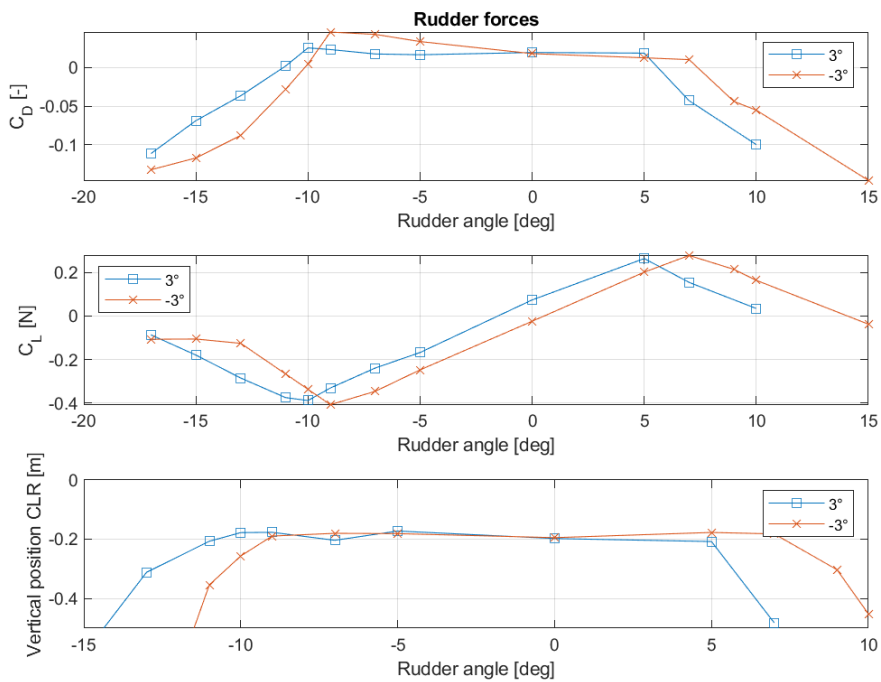


Figure D.8: The rudder lift and drag forces on the reference earth coordinate system, together with the distance from the hull to the CLR of the rudder, for a leeway angle of 3° and -3° of leeway.

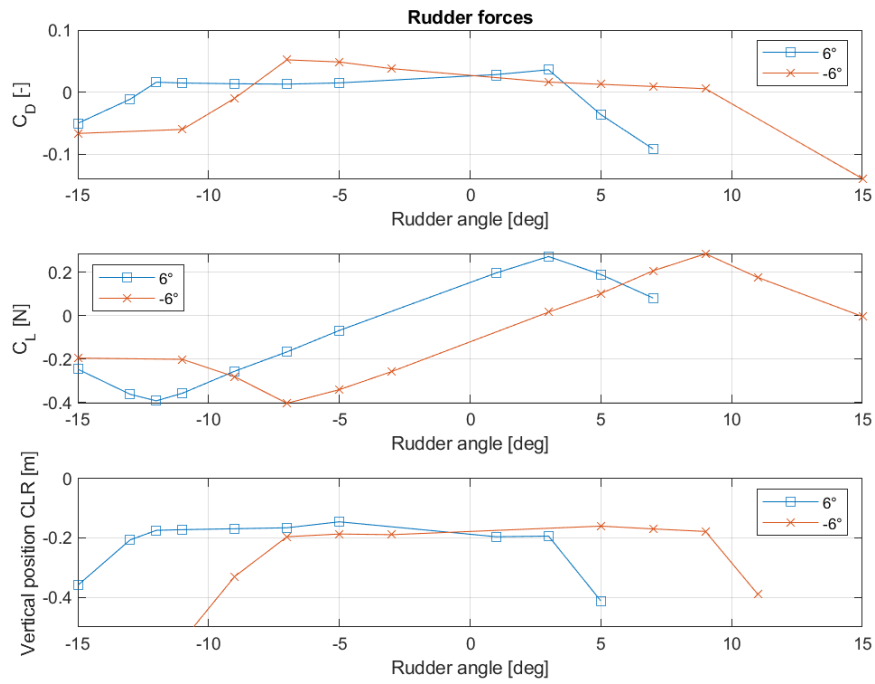


Figure D.9: The rudder lift and drag forces on the reference earth coordinate system, together with the distance from the hull to the CLR of the rudder, for a leeway angle of 6° and -6° of leeway.

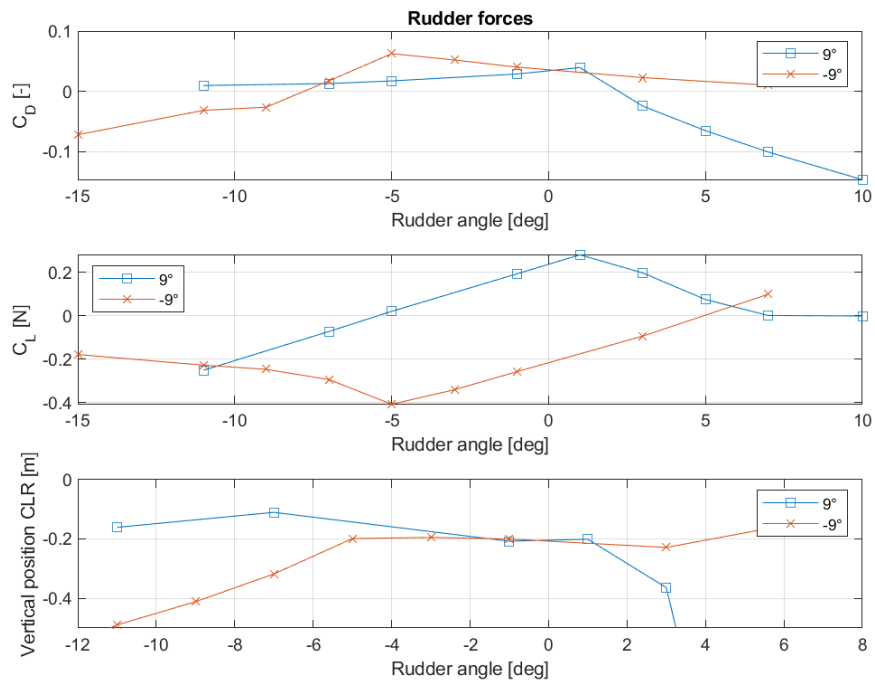


Figure D.10: The rudder lift and drag forces on the reference earth coordinate system, together with the distance from the hull to the CLR of the rudder, for a leeway angle of 9° and -9° of leeway.

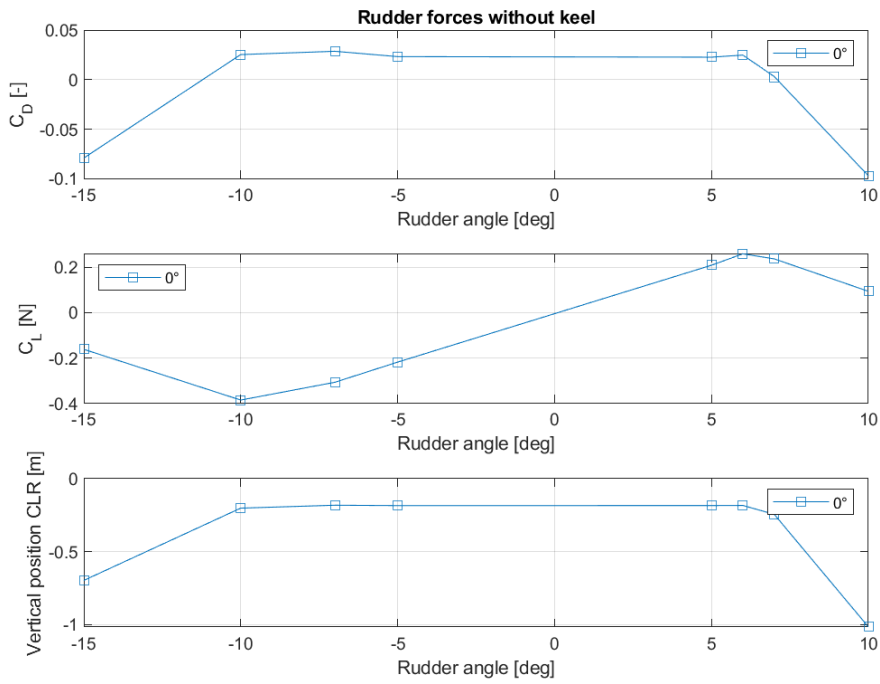


Figure D.11: The rudder lift and drag forces on the reference earth coordinate system, together with the distance from the hull to the CLR of the rudder, for a leeway angle of 9° and -9° of leeway, without keel fitted.

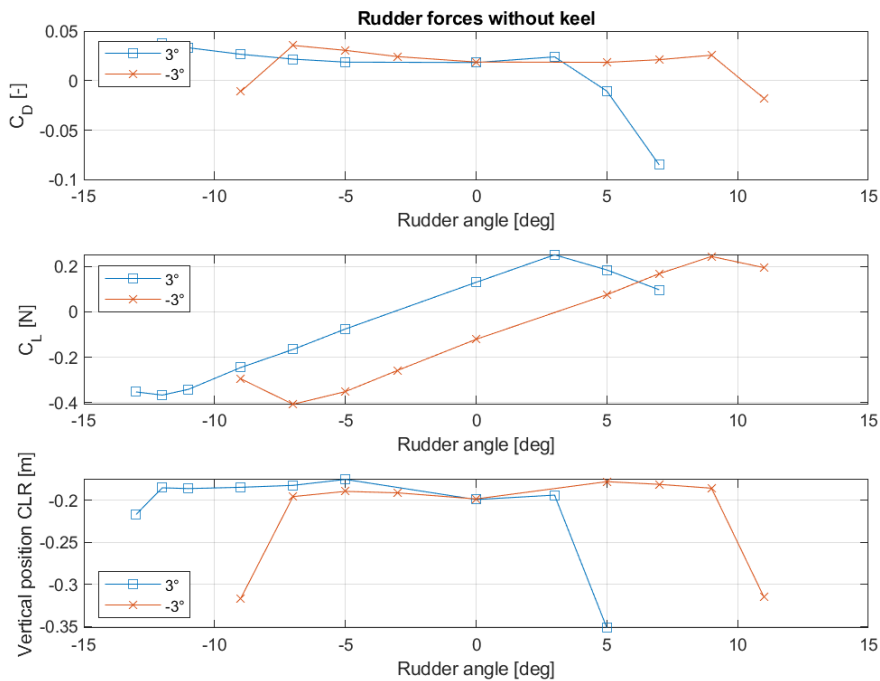


Figure D.12: The rudder lift and drag forces on the reference earth coordinate system, together with the distance from the hull to the CLR of the rudder, for a leeway angle of 9° and -9° of leeway, without keel fitted.

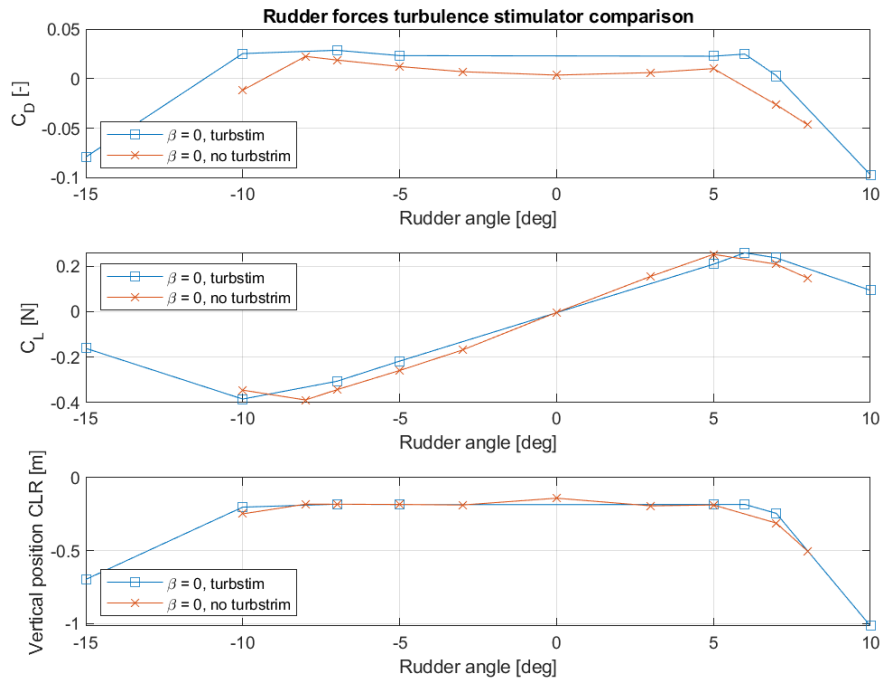


Figure D.13: A comparison of the rudders' lift and drag tested with and without carboniumstrips.

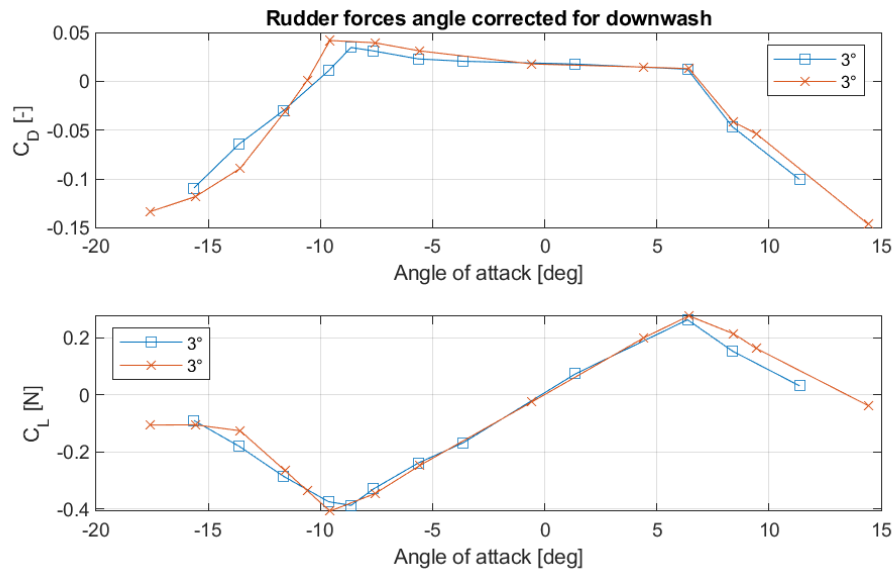


Figure D.14: The rudder forces for 3° and -3° of leeway, corrected for their downwash angle. The angle of incidence on the rudder is relative to the local flow.

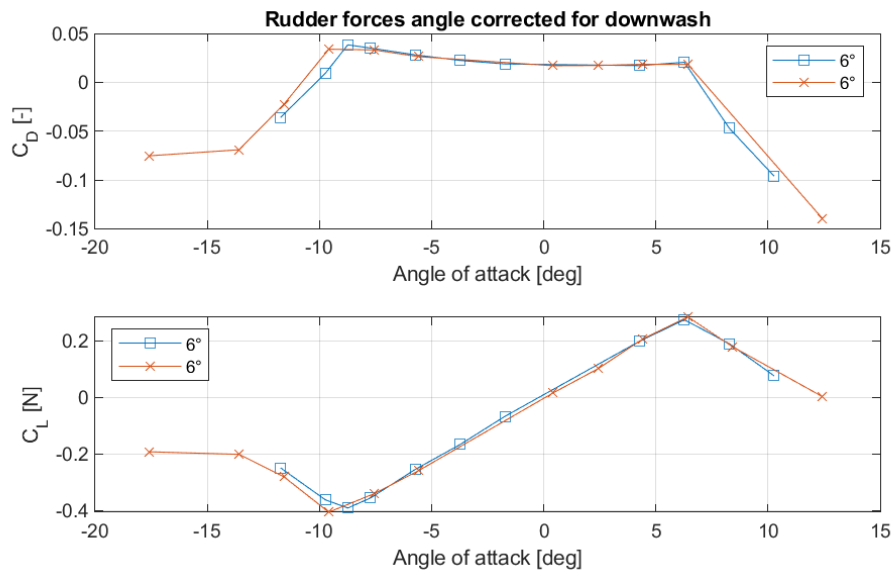


Figure D.15: The rudder forces for 6° and -6° of leeway, corrected for their downwash angle. The angle of incidence on the rudder is relative to the local flow.

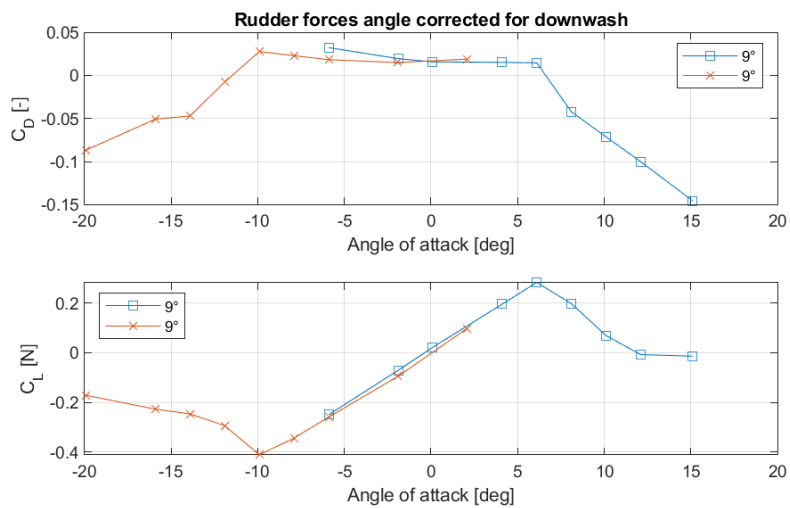
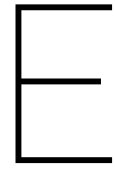


Figure D.16: The rudder forces for 9° and -9° of leeway, corrected for their downwash angle. The angle of incidence on the rudder is relative to the local flow.



Experimental uncertainty assessments

E.1. Model

Fx_model (beta=3, delta=0)	Type	Uncertainty	Remark
Wetted Area	B	0,03%	neglectable
Dynamometer	A	0,17%	minor
Speed	B	0,29%	minor
Watertemp	B	0,02%	neglectable
Repeated, single	A	1,39%	dominant
Combined, single		1,43%	
Conf interval, single		2,87%	
Repeated, mean	A	0,70%	
Combined, mean		0,84%	
Conf interval, mean		1,69%	

Figure E.1: The uncertainty table to the example ITTC [25]. The uncertainty for the model resistance for 3° leeway and 0° rudder angle.

Fx_model (beta=-3, delta=-5)	Type	Uncertainty	Remark
Wetted Area	B	0,03%	neglectable
Dynamometer	A	0,17%	minor
Speed	B	0,29%	minor
Watertemp	B	0,02%	neglectable
Repeated, single	A	1,93%	dominant
Combined, single		1,96%	
Conf interval, single		3,93%	
Repeated, mean	A	0,77%	
Combined, mean		0,78%	
Conf interval, mean		1,55%	

Figure E.2: The uncertainty table to the example ITTC [25]. The uncertainty for the model resistance for -3° leeway and -5° rudder angle.

Fy_model (beta=3, delta=0)	Type	Uncertainty	Remark
Wetted Area	B	0,03%	neglectable
Dynamometer	A	0,11%	minor
Speed	B	0,29%	minor
Watertemp	B	0,02%	neglectable
Repeated, single	A	2,83%	dominant
Combined, single		2,85%	
Conf interval, single		5,70%	
Repeated, mean	A	1,06%	
Combined, mean		1,29%	
Conf interval, mean		2,58%	

Figure E.3: The uncertainty table to the example ITTC [25]. The uncertainty for the model side force for 3° leeway and 0° rudder angle.

Fy_model (beta=-3, delta=-5)	Type	Uncertainty	Remark
Wetted Area	B	0,03%	neglectable
Dynamometer	A	0,11%	minor
Speed	B	0,29%	minor
Watertemp	B	0,02%	neglectable
Repeated, single	A	1,93%	dominant
Combined, single		1,96%	
Conf interval, single		3,92%	
Repeated, mean	A	1,25%	
Combined, mean		1,11%	
Conf interval, mean		2,22%	

Figure E.4: The uncertainty table to the example ITTC [25]. The uncertainty for the model side force for -3° leeway and -5° rudder angle.

Mz_model (beta=3, delta=0)	Type	Uncertainty	Remark
Wetted Area	B	0,03%	neglectable
Dynamometer	A	0,11%	minor
Speed	B	0,29%	minor
Watertemp	B	0,02%	neglectable
Repeated, single	A	2,83%	dominant
Combined, single		2,85%	
Conf interval, single		5,70%	
Repeated, mean	A	1,06%	
Combined, mean		1,29%	
Conf interval, mean		2,58%	

Figure E.5: The uncertainty table to the example ITTC [25]. The uncertainty for the model yaw moment for 3° leeway and 0° rudder angle.

Mz_model (beta=-3, delta=-5)	Type	Uncertainty	Remark
Wetted Area	B	0,03%	neglectable
Dynamometer	A	0,11%	minor
Speed	B	0,29%	minor
Watertemp	B	0,02%	neglectable
Repeated, single	A	2,55%	dominant
Combined, single		2,57%	
Conf interval, single		5,14%	
Repeated, mean	A	1,25%	
Combined, mean		1,11%	
Conf interval, mean		2,22%	

Figure E.6: The uncertainty table to the example ITTC [25]. The uncertainty for the model yaw moment for -3° leeway and -5° rudder angle.

E.2. Keel

Cd_keel (beta=3, delta=0)	Type	Uncertainty	Remark
Wetted area	B	0,01%	neglectable
Dynamometer	A	0,16%	minor
Speed	B	0,29%	minor
Watertemp	B	0,02%	neglectable
Repeated	A	1,39%	dominant
Combined		1,43%	
Conf interval		2,87%	
Repeated, mean	A	0,70%	
Combined, mean		0,77%	
Conf interval, mean		1,54%	

Figure E.7: The uncertainty table to the example ITTC [25]. The uncertainty for the keel drag coefficient for 3° leeway and 0° rudder angle.

Cd_keel (beta=-3, delta=-5)	Type	Uncertainty	Remark
Wetted area	B	0,01%	neglectable
Dynamometer	A	0,16%	minor
Speed	B	0,29%	minor
Watertemp	B	0,02%	neglectable
Repeated	A	1,93%	dominant
Combined		1,96%	
Conf interval		3,92%	
Repeated, mean	A	0,77%	
Combined, mean		0,84%	
Conf interval, mean		1,68%	

Figure E.8: The uncertainty table to the example ITTC [25]. The uncertainty for the keel drag coefficient for -3° leeway and -5° rudder angle.

Cl_keel (beta=3, delta=0)	Type	Uncertainty	Remark
Wetted area	B	0,01%	neglectable
Dynamometer	A	0,21%	minor
Speed	B	0,29%	minor
Watertemp	B	0,02%	neglectable
Repeated	A	2,83%	dominant
Combined		2,85%	
Conf interval		5,71%	
Repeated, mean	A	1,06%	
Combined, mean		1,12%	
Conf interval, mean		2,25%	

Figure E.9: The uncertainty table to the example ITTC [25]. The uncertainty for the keel lift coefficient for 3° leeway and 0° rudder angle.

Cl_keel (beta=-3, delta=-5)	Type	Uncertainty	Remark
Wetted area	B	0,01%	neglectable
Dynamometer	A	0,21%	minor
Speed	B	0,29%	minor
Watertemp	B	0,02%	neglectable
Repeated	A	2,55%	dominant
Combined		2,57%	
Conf interval		5,15%	
Repeated, mean	A	1,25%	
Combined, mean		1,30%	
Conf interval, mean		2,60%	

Figure E.10: The uncertainty table to the example ITTC [25]. The uncertainty for the keel lift coefficient for -3° leeway and -5° rudder angle.

E.3. Rudder

Cd_rudder (beta=3, delta=0)	Type	Uncertainty	Remark
Wetted area	B	0,03%	neglectable
Dynamometer	A	0,08%	minor
Speed	B	0,29%	minor
Watertemp	B	0,02%	neglectable
Repeated	A	1,39%	dominant
Combined		1,43%	
Conf interval		2,85%	
Repeated, mean	A	0,70%	
Combined, mean		0,76%	
Conf interval, mean		1,52%	

Figure E.11: The uncertainty table to the example ITTC [25]. The uncertainty for the rudder drag coefficient for 3° leeway and 0° rudder angle.

Cd_rudder (beta=-3, delta=-5)	Type	Uncertainty	Remark
Wetted area	B	0,03%	neglectable
Dynamometer	A	0,08%	minor
Speed	B	0,29%	minor
Watertemp	B	0,02%	neglectable
Repeated	A	1,93%	dominant
Combined		1,96%	
Conf interval		3,91%	
Repeated, mean	A	0,77%	
Combined, mean		0,83%	
Conf interval, mean		1,66%	

Figure E.12: The uncertainty table to the example ITTC [25]. The uncertainty for the rudder drag coefficient for -3° leeway and -5° rudder angle.

Cl_rudder (beta=3, delta=0)	Type	Uncertainty	Remark
Wetted area	B	0,03%	neglectable
Dynamometer	A	0,28%	minor
Speed	B	0,29%	minor
Watertemp	B	0,02%	neglectable
Repeated	A	2,83%	dominant
Combined		2,86%	
Conf interval		5,72%	
Repeated, mean	A	1,06%	
Combined, mean		1,14%	
Conf interval, mean		2,28%	

Figure E.13: The uncertainty table to the example ITTC [25]. The uncertainty for the rudder lift coefficient for 3° leeway and 0° rudder angle.

Cl_rudder (beta=-3, delta=-5)	Type	Uncertainty	Remark
Wetted area	B	0,03%	neglectable
Dynamometer	A	0,28%	minor
Speed	B	0,29%	minor
Watertemp	B	0,02%	neglectable
Repeated	A	2,55%	dominant
Combined		2,58%	
Conf interval		5,16%	
Repeated, mean	A	1,25%	
Combined, mean		1,31%	
Conf interval, mean		2,63%	

Figure E.14: The uncertainty table to the example ITTC [25]. The uncertainty for the rudder lift coefficient for -3° leeway and -5° rudder angle.

CLR_rudder (beta=3, delta=0)	Type	Uncertainty	Remark
Wetted area	B	0,03%	neglectable
Dynamometer	A	0,50%	minor
Speed	B	0,29%	minor
Watertemp	B	0,02%	neglectable
Repeated	A	2,16%	dominant
Combined		2,24%	
Conf interval		4,47%	
Repeated, mean	A	1,53%	
Combined, mean		1,63%	
Conf interval, mean		3,27%	

Figure E.15: The uncertainty table to the example ITTC [25]. The uncertainty for the CLR for the rudder for 3° leeway and 0° rudder angle.

CLR_rudder (beta=-3, delta=-5)	Type	Uncertainty	Remark
Wetted area	B	0,03%	neglectable
Dynamometer	A	0,50%	minor
Speed	B	0,29%	minor
Watertemp	B	0,02%	neglectable
Repeated	A	2,16%	dominant
Combined		2,24%	
Conf interval		4,47%	
Repeated, mean	A	1,53%	
Combined, mean		1,63%	
Conf interval, mean		3,27%	

Figure E.16: The uncertainty table to the example ITTC [25]. The uncertainty for the CLR for the rudder for -3° leeway and -5° rudder angle.

F

Uncertainty assessment

E.1. Test case $\beta = 3^\circ$ and $\delta = 0^\circ$

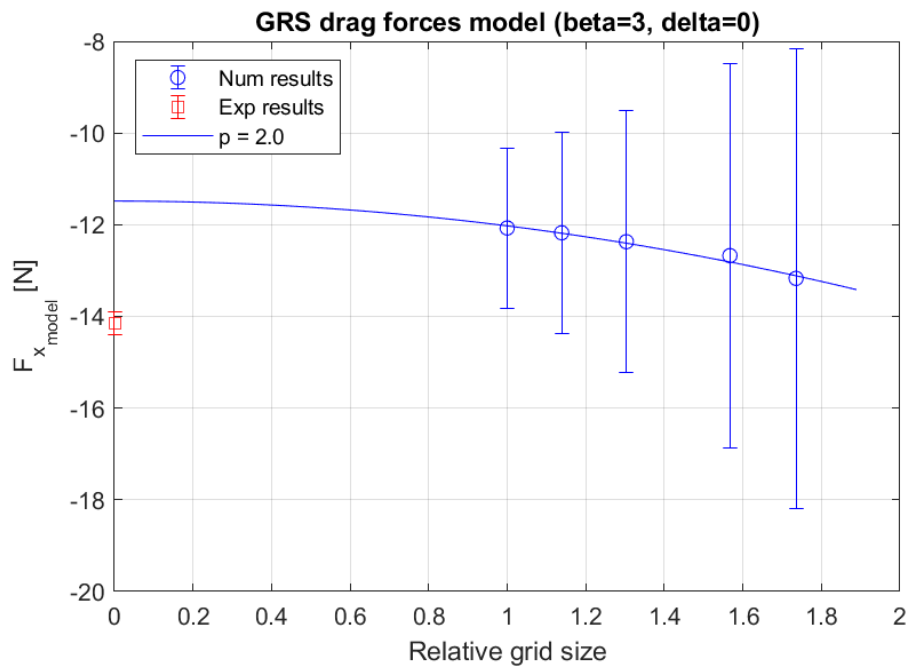


Figure E1: The grid convergence plot for the drag force for the model, for the case of $\beta = 3^\circ$ and $\delta = 0^\circ$.

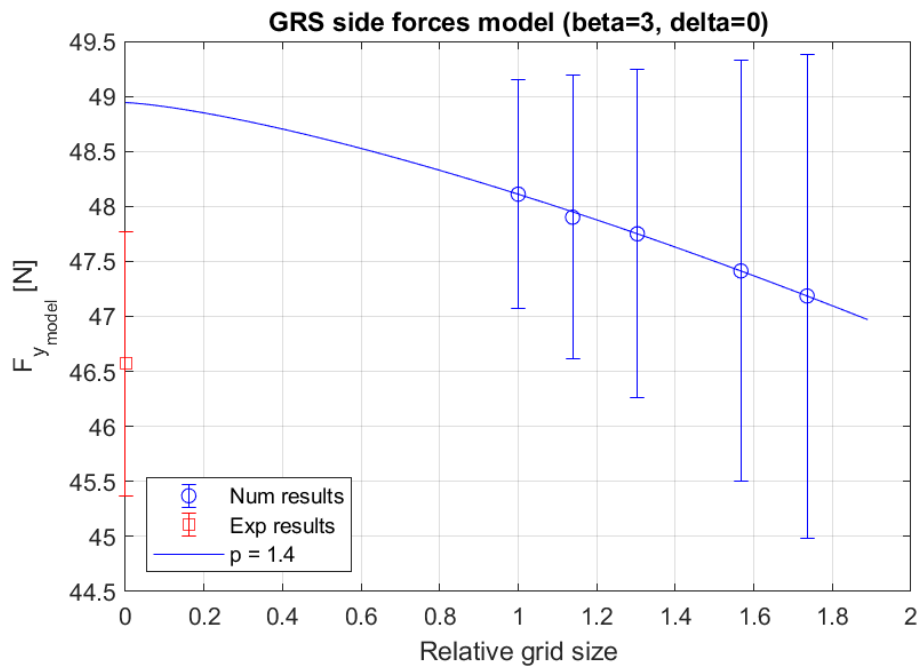
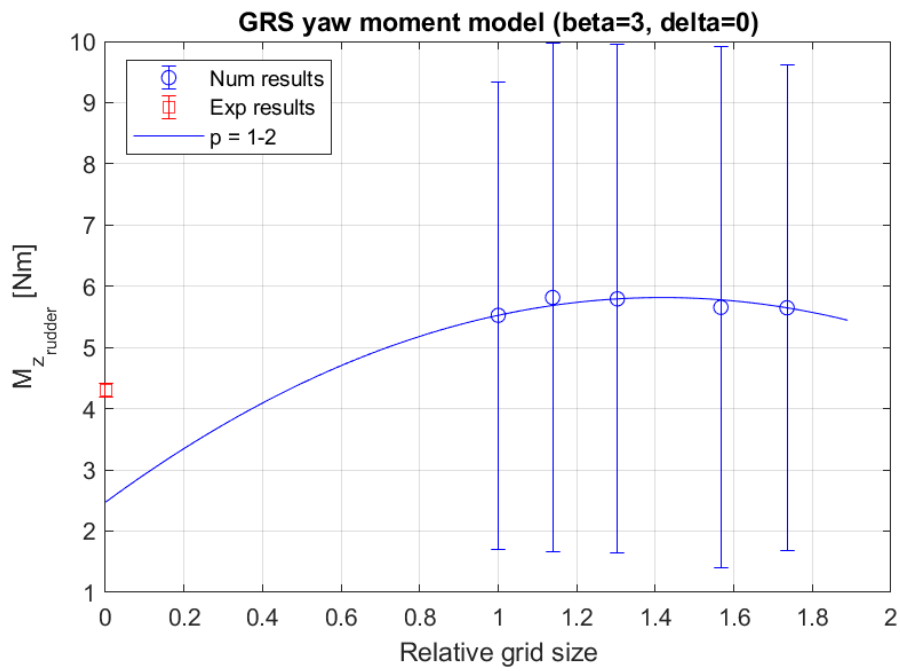
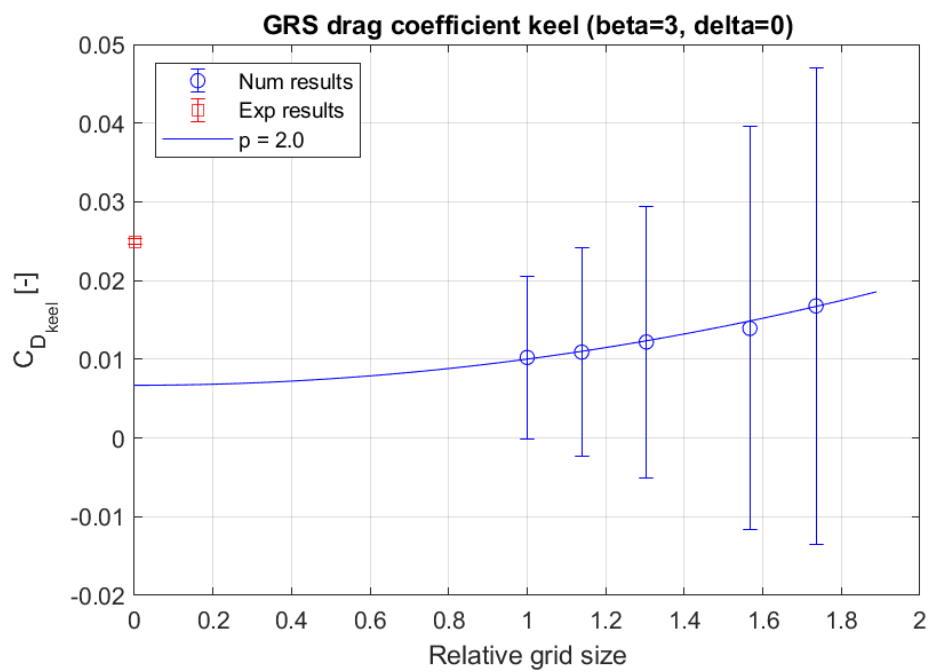


Figure E2: The grid convergence plot for the side force for the model, for the case of $\beta = 3^\circ$ and $\delta = 0^\circ$.

Figure E3: The grid convergence plot for the yaw moment for the model, for the case of $\beta = 3^\circ$ and $\delta = 0^\circ$.Figure E4: The grid convergence plot for the drag coefficient of the keel, for the case of $\beta = 3^\circ$ and $\delta = 0^\circ$.

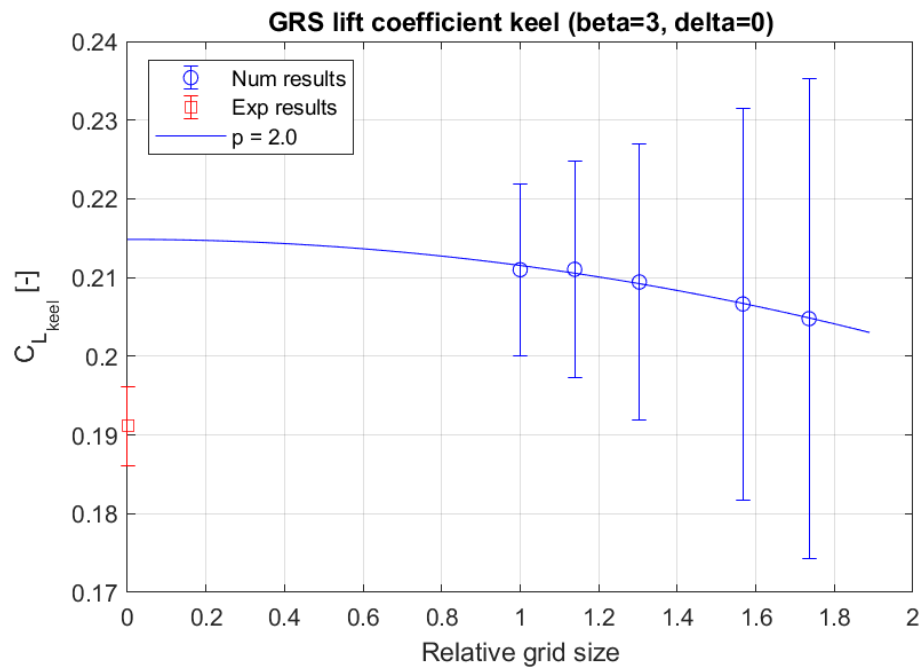


Figure E5: The grid convergence plot for the lift coefficient of the keel, for the case of $\beta = 3^\circ$ and $\delta = 0^\circ$.

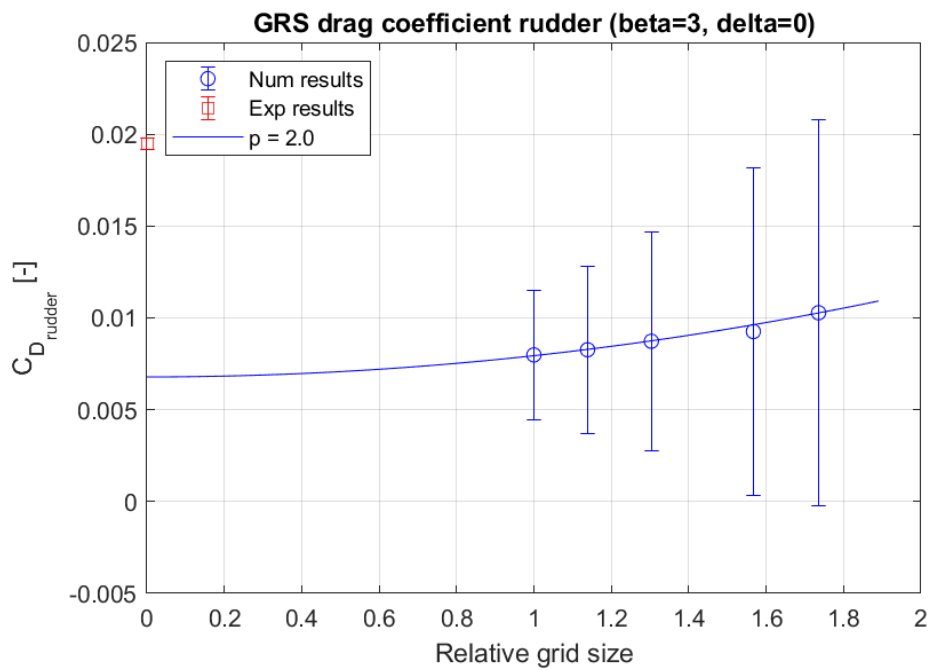


Figure E6: The grid convergence plot for the drag coefficient of the rudder, for the case of $\beta = 3^\circ$ and $\delta = 0^\circ$.

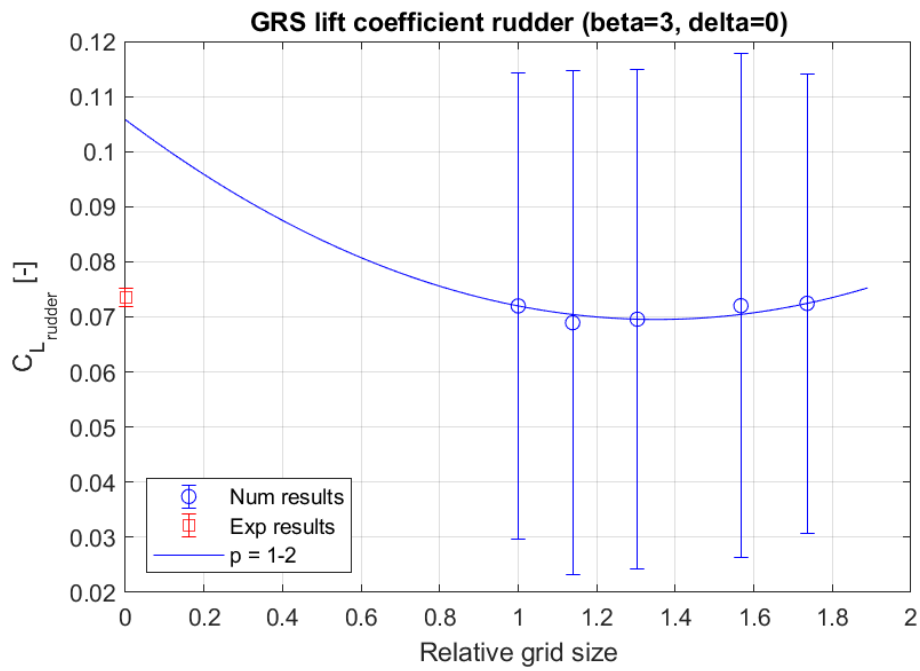


Figure E7: The grid convergence plot for the lift coefficient of the rudder, for the case of $\beta = 3^\circ$ and $\delta = 0^\circ$.

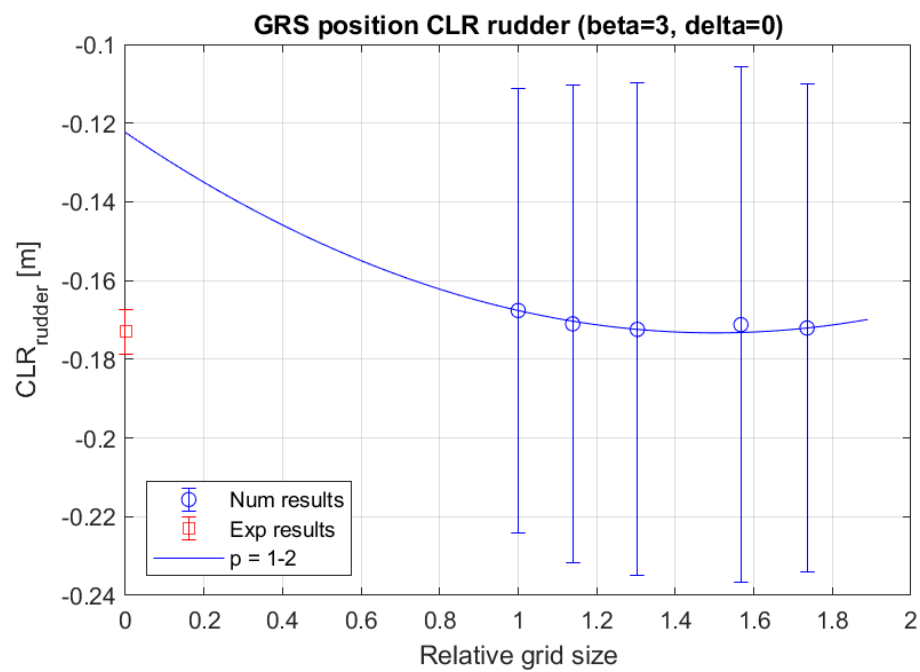


Figure E8: The grid convergence plot for the vertical location of the lateral resistance for the rudder, for the case of $\beta = 3^\circ$ and $\delta = 0^\circ$.

F.2. Test case $\beta = -3^\circ$ and $\delta = -5^\circ$

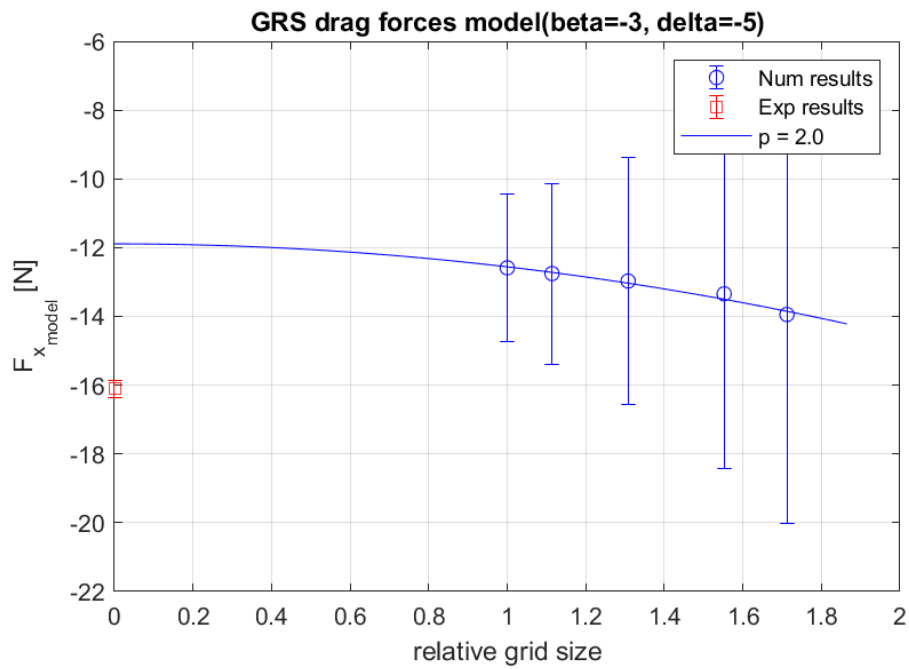


Figure E9: The grid convergence plot for the drag force for the model, for the case of $\beta = -3^\circ$ and $\delta = -5^\circ$.

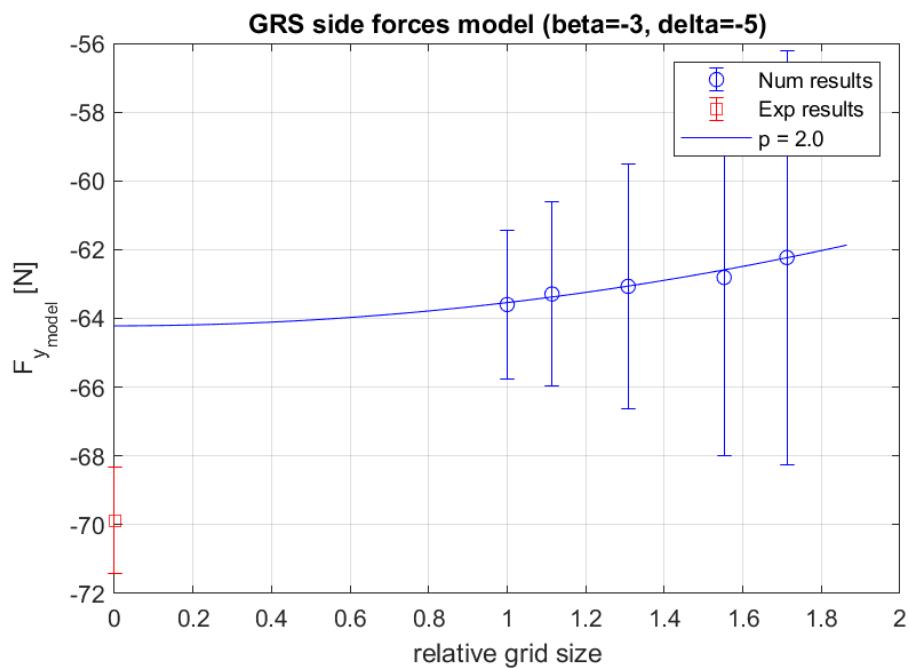


Figure E10: The grid convergence plot for the side force for the model, for the case of $\beta = -3^\circ$ and $\delta = -5^\circ$.

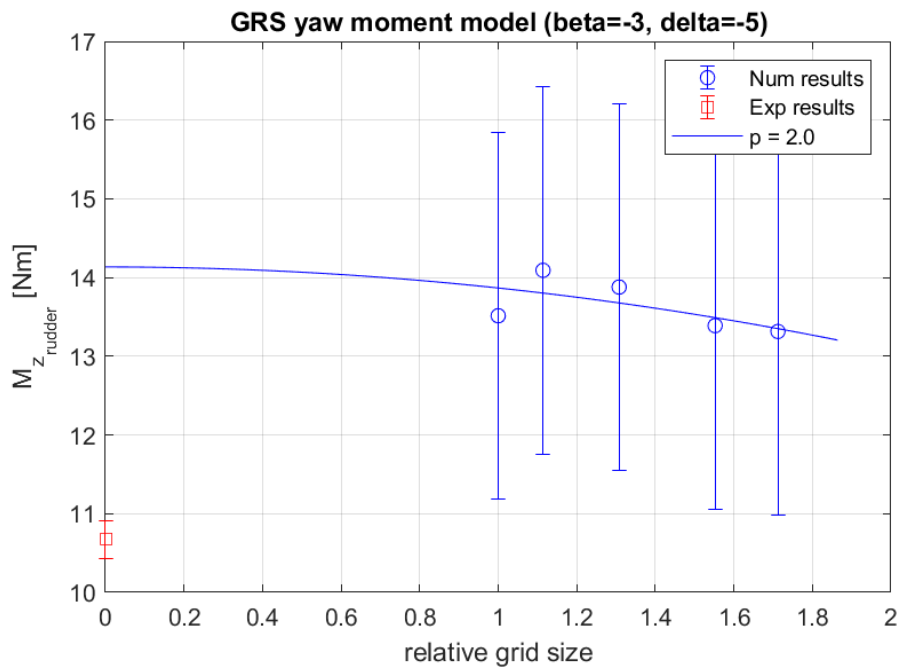


Figure F.11: The grid convergence plot for the yaw moment for the model, for the case of $\beta = -3^\circ$ and $\delta = -5^\circ$.

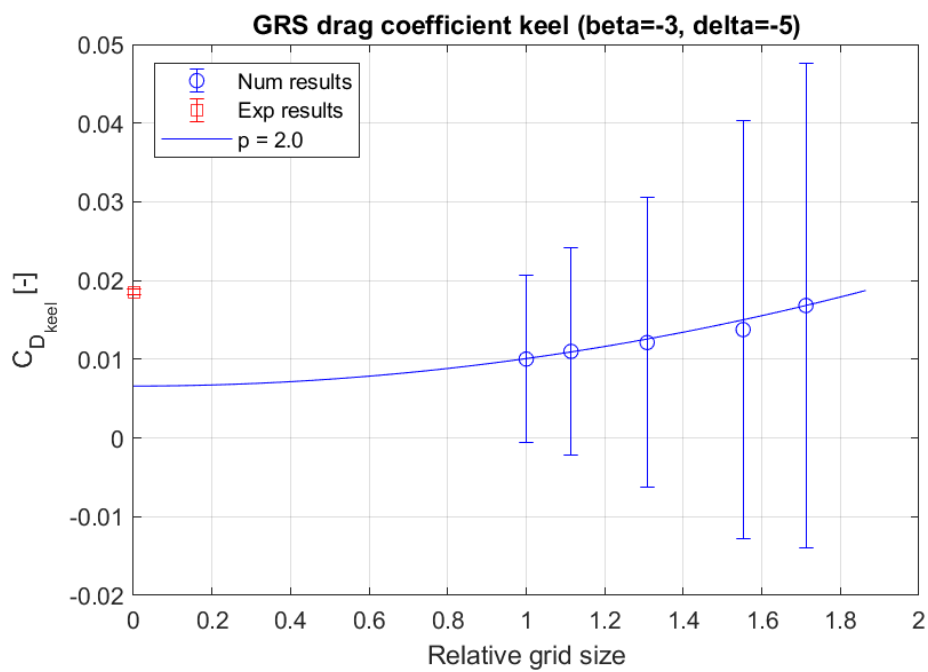


Figure F.12: The grid convergence plot for the drag coefficient of the keel, for the case of $\beta = -3^\circ$ and $\delta = -5^\circ$.

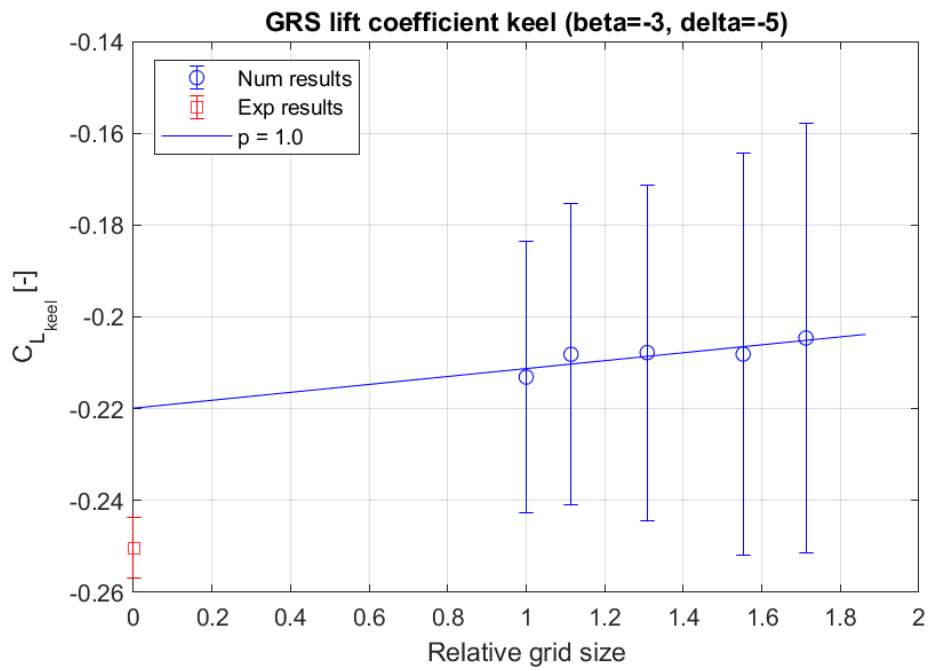


Figure E.13: The grid convergence plot for the lift coefficient of the keel, for the case of $\beta = -3^\circ$ and $\delta = -5^\circ$.

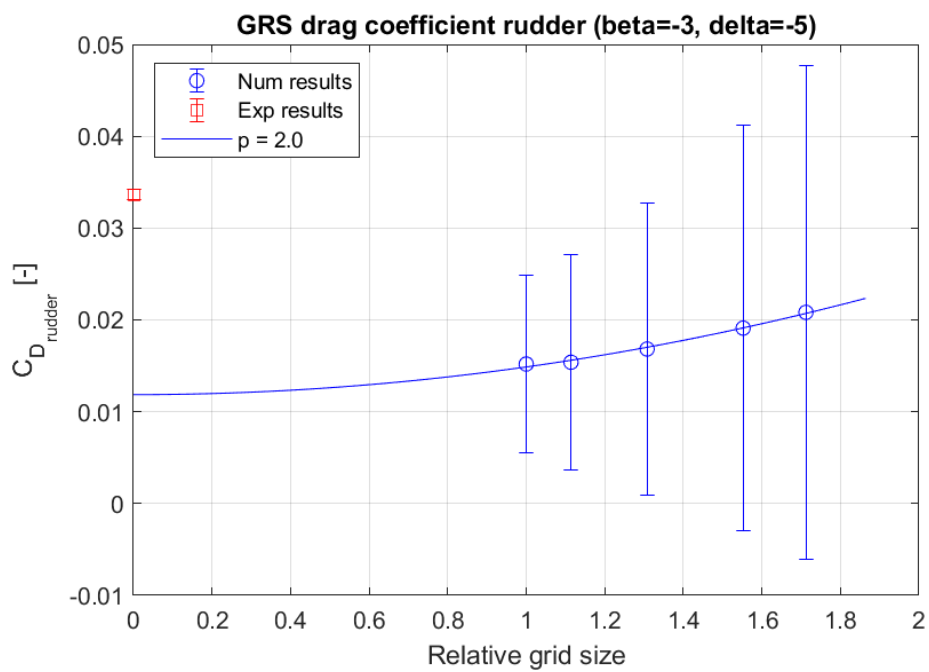


Figure E.14: The grid convergence plot for the drag coefficient of the rudder, for the case of $\beta = -3^\circ$ and $\delta = -5^\circ$.

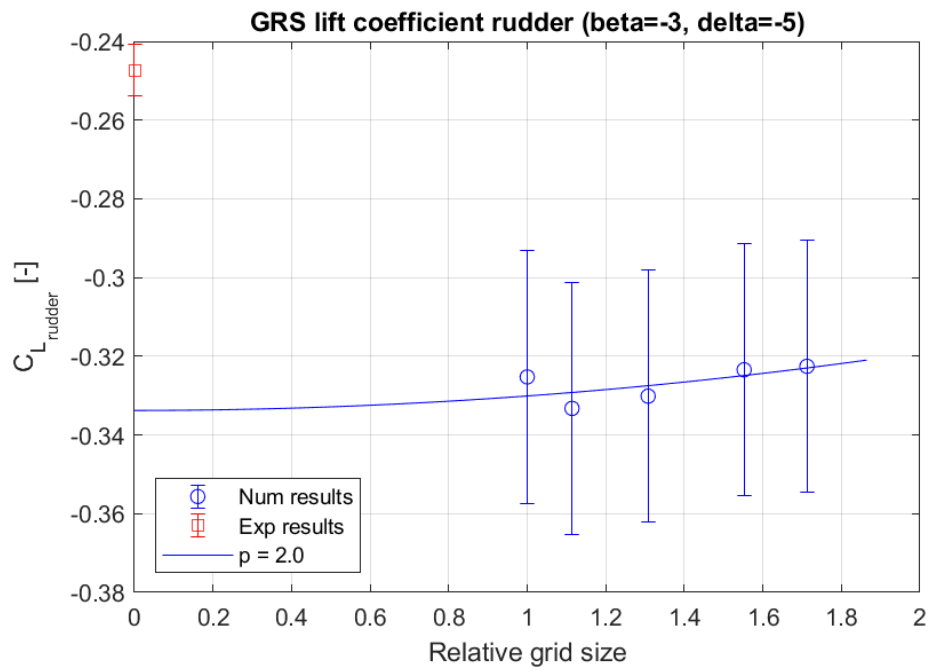


Figure E.15: The grid convergence plot for the lift coefficient of the rudder, for the case of $\beta = -3^\circ$ and $\delta = -5^\circ$.

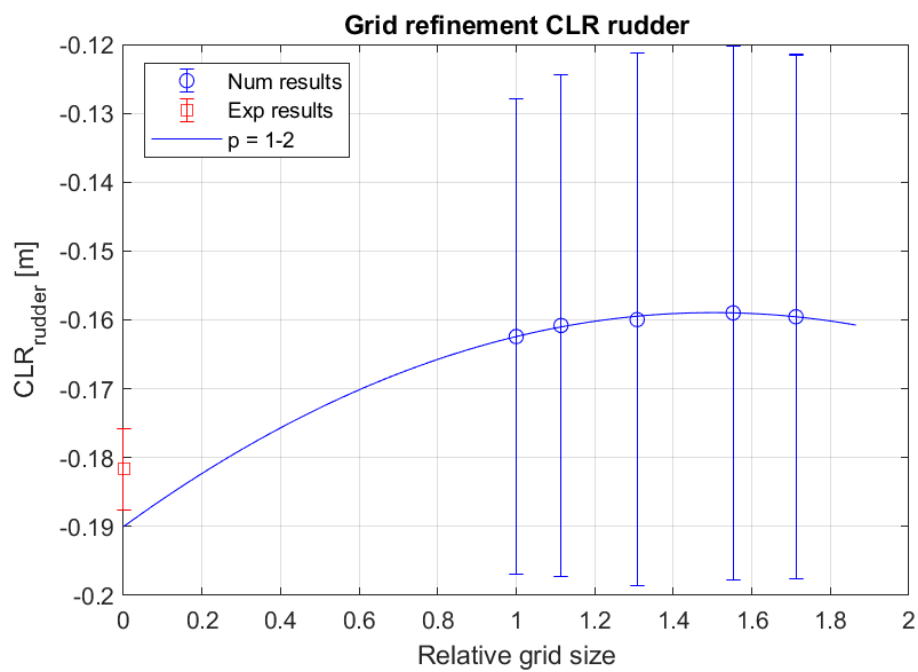


Figure E.16: The grid convergence plot for the vertical location of the lateral resistance for the rudder, for the case of $\beta = -3^\circ$ and $\delta = -5^\circ$.

G

CFD results discussed in chapter 6

G.1. Drag part

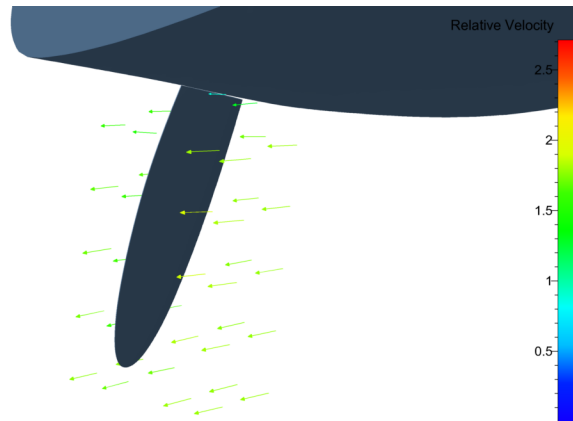


Figure G.1: The flow direction and velocity around the rudder for test case $\beta = 3^\circ$ and $\delta = -13$, seen from starboard side.

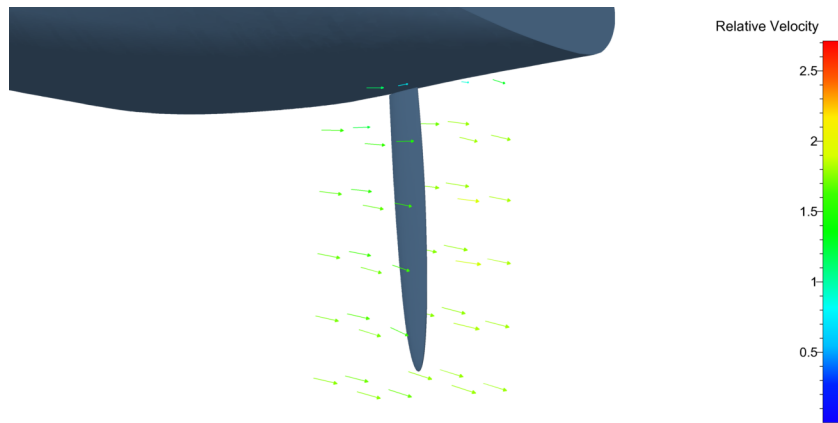


Figure G.2: The flow direction and velocity around the rudder for test case $\beta = 3^\circ$ and $\delta = -13$, seen from port side.

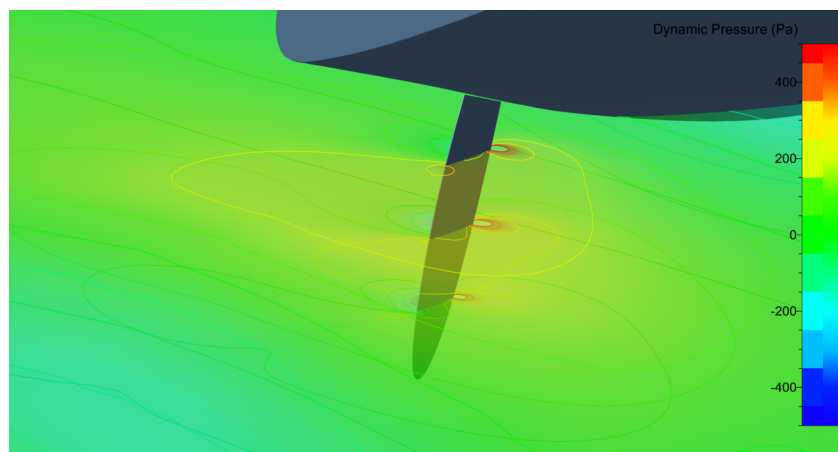


Figure G.3: The dynamic pressure plotted on x - y -planes around the rudder for test case $\beta = 3^\circ$ and $\delta = 7$.

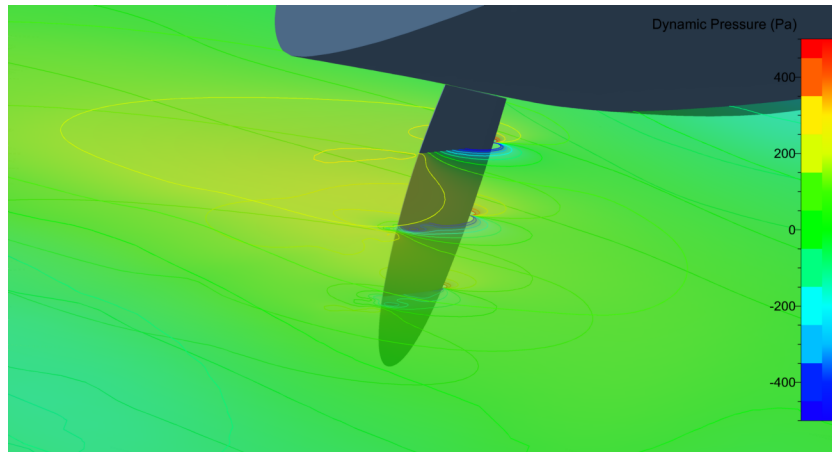


Figure G.4: The dynamic pressure plotted on xy -planes around the rudder for test case $\beta = 3^\circ$ and $\delta = -13^\circ$.

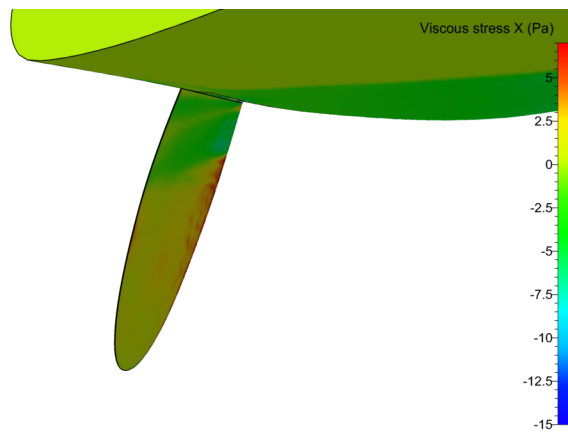


Figure G.5: The viscous stress in x -direction over the rudder, for the test case with $\beta = 3^\circ$ and $\delta = -13^\circ$. Seen from the starboard side.

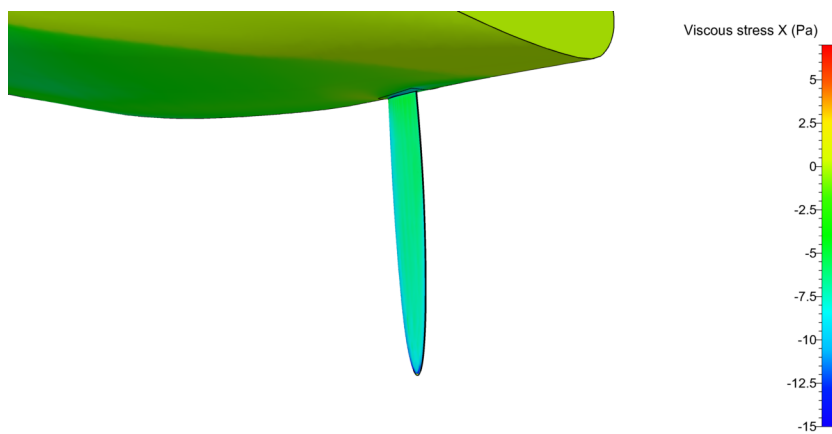


Figure G.6: The viscous stress in x -direction over the rudder, for the test case with $\beta = 3^\circ$ and $\delta = -13^\circ$. Seen from the port side.

G.2. Lift part

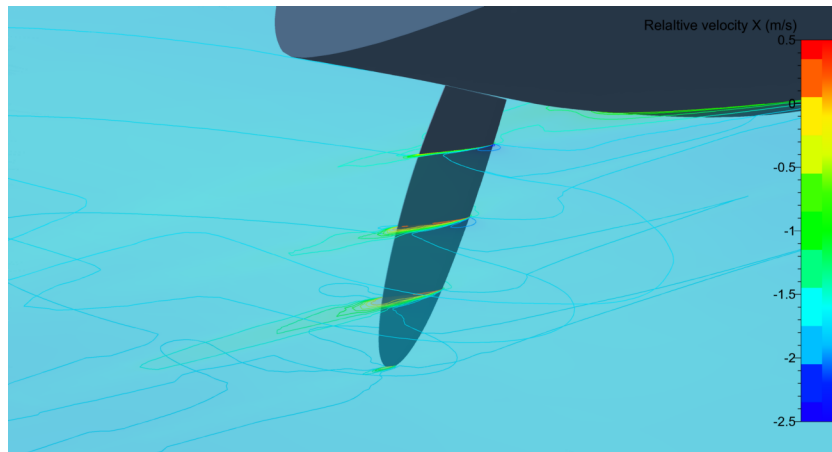


Figure G.7: The velocity in x -direction over the rudder plotted on multiple xy -planes, for the test case with $\beta = 3^\circ$ and $\delta = -13^\circ$

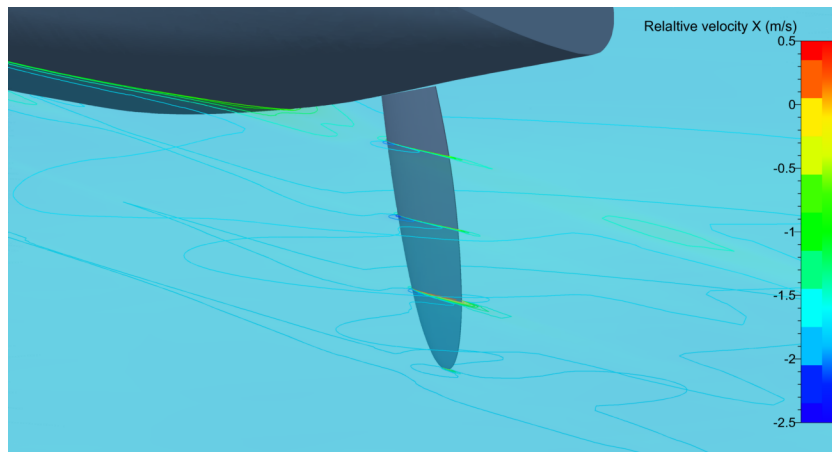


Figure G.8: The velocity in x -direction over the rudder plotted on multiple xy -planes, for the test case with $\beta = 3^\circ$ and $\delta = 7^\circ$

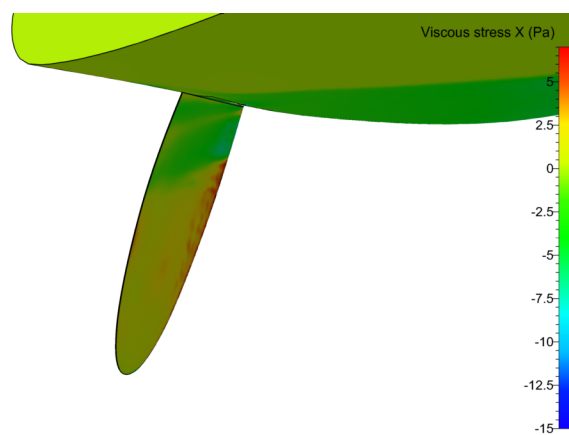


Figure G.9: The viscous stress in x -direction over the rudder, for the test case with $\beta = 3^\circ$ and $\delta = -13^\circ$. Seen from the starboard side.

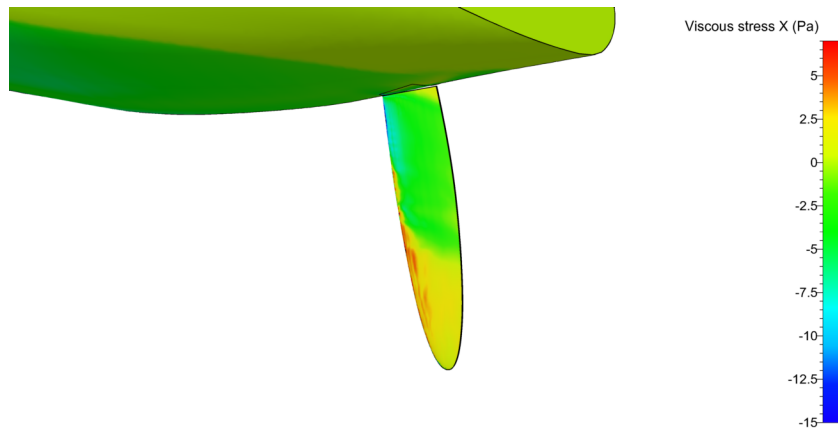


Figure G.10: The viscous stress in x -direction over the rudder, for the test case with $\beta = 3^\circ$ and $\delta = 7^\circ$. Seen from the port side.

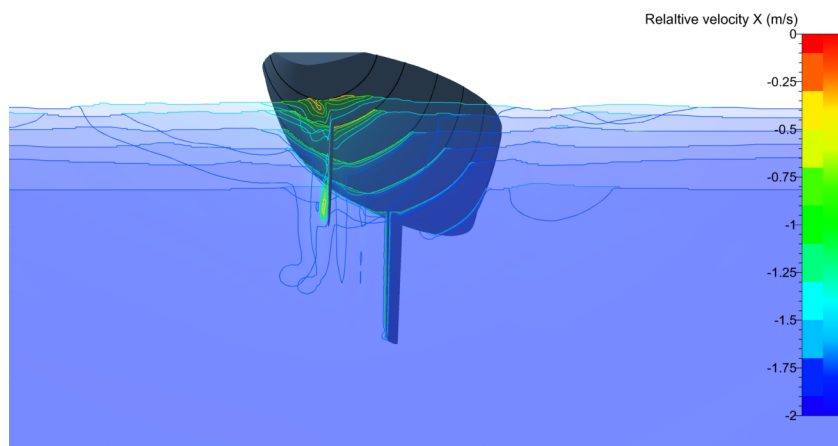


Figure G.11: The velocity in x -direction plotted on multiple yz -planes, for the test case with $\beta = 3^\circ$ and $\delta = 7^\circ$

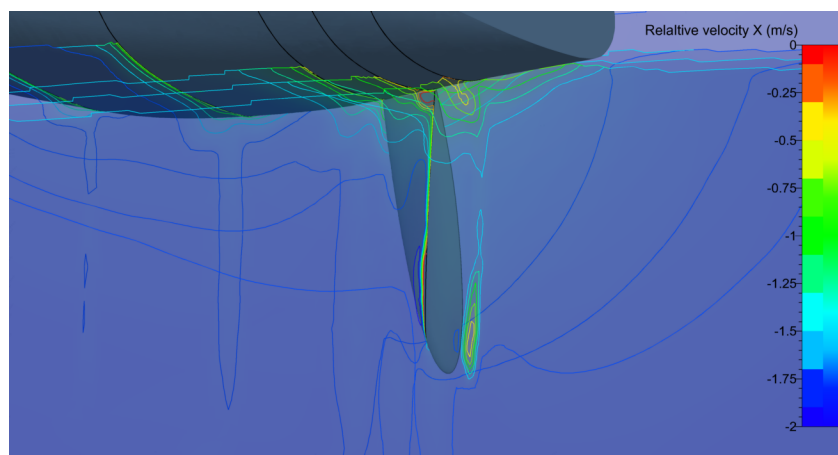


Figure G.12: The velocity in x -direction plotted on multiple yz -planes, for the test case with $\beta = 3^\circ$ and $\delta = 7^\circ$

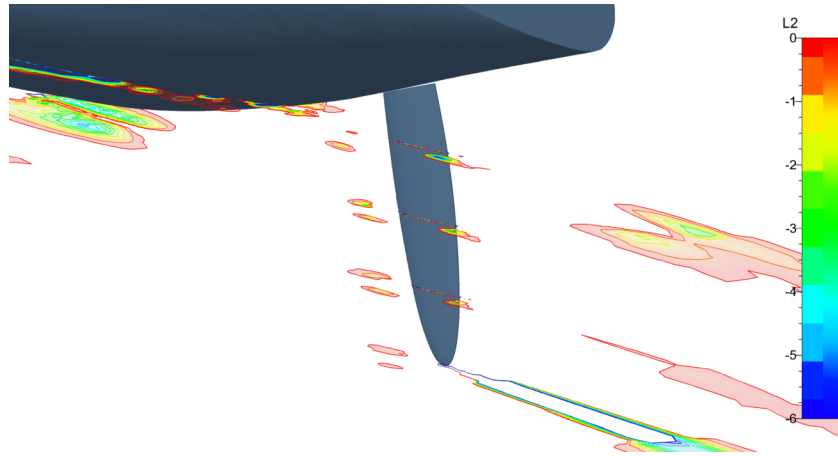


Figure G.13: The λ_2 values to identify vortex structures plotted at a number of xy -planes. For test case $\beta = 3^\circ$ and $\delta = 5^\circ$

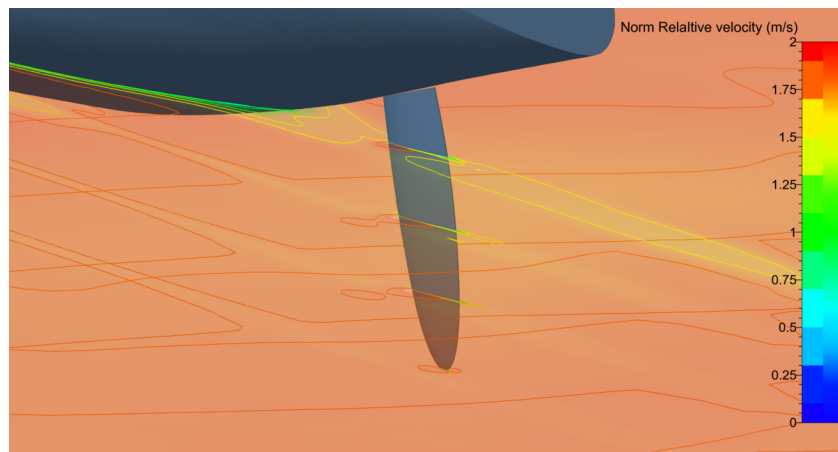


Figure G.14: The normalised velocity plotted at a number of xy -planes. For test case $\beta = 3^\circ$ and $\delta = 5^\circ$

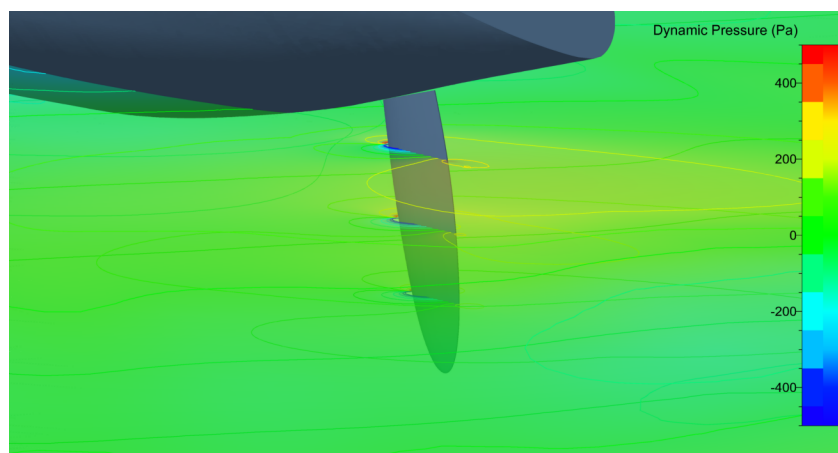


Figure G.15: The dynamic pressure plotted at a number of xy -planes. For test case $\beta = 3^\circ$ and $\delta = 5^\circ$

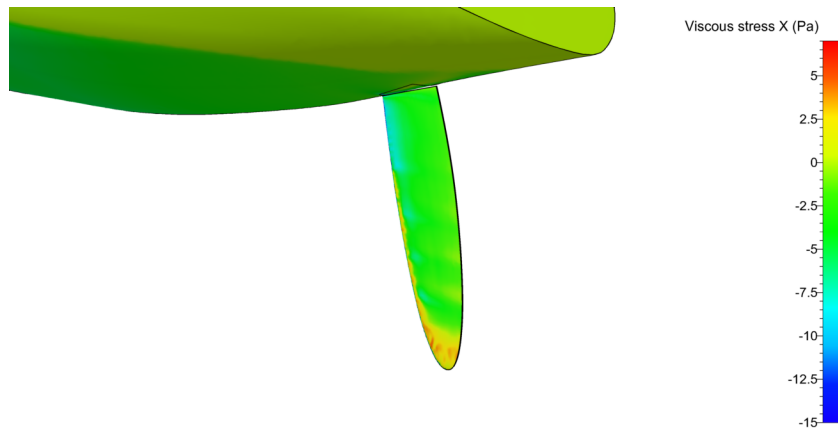


Figure G.16: The shear stress in x -direction for test case without keel and a rudder angle 7° .

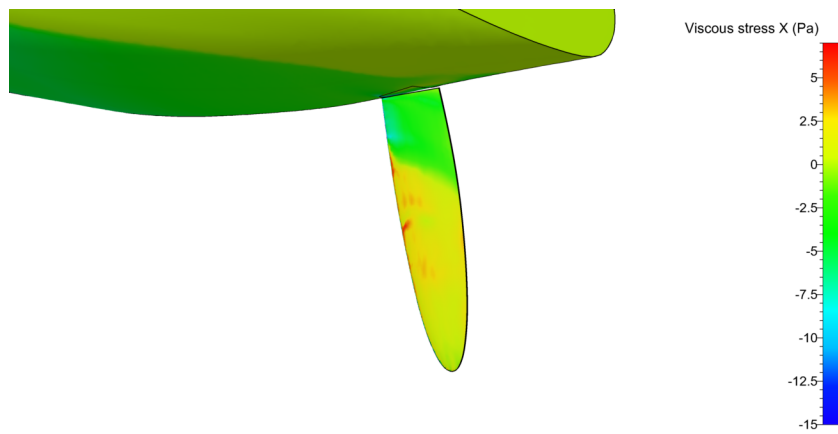


Figure G.17: The shear stress in x -direction for test case without keel and a rudder angle 10° .

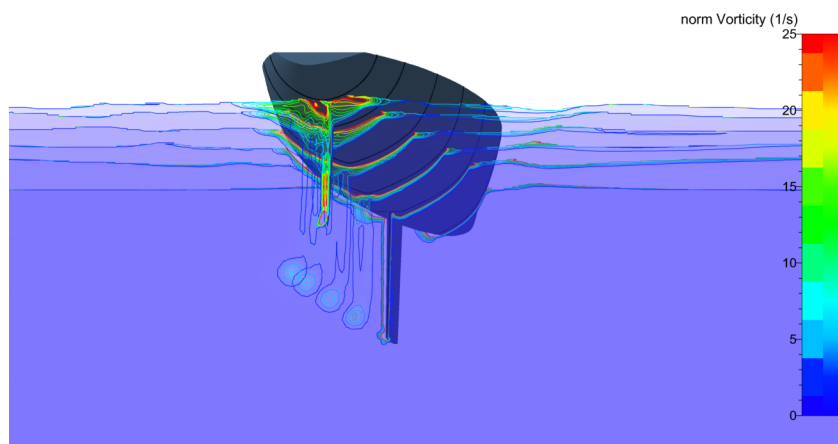


Figure G.18: The normalised vorticity plotted on multiple yz -planes, for the test case with $\beta = 3^\circ$ and $\delta = 5^\circ$

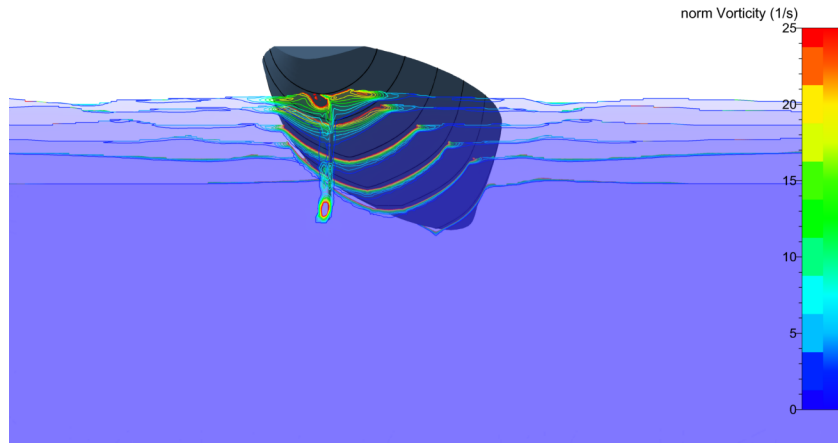


Figure G.19: The normalised vorticity plotted on multiple yz -planes, for the test case with $\beta = 0^\circ$ and $\delta = 7^\circ$ and without keel

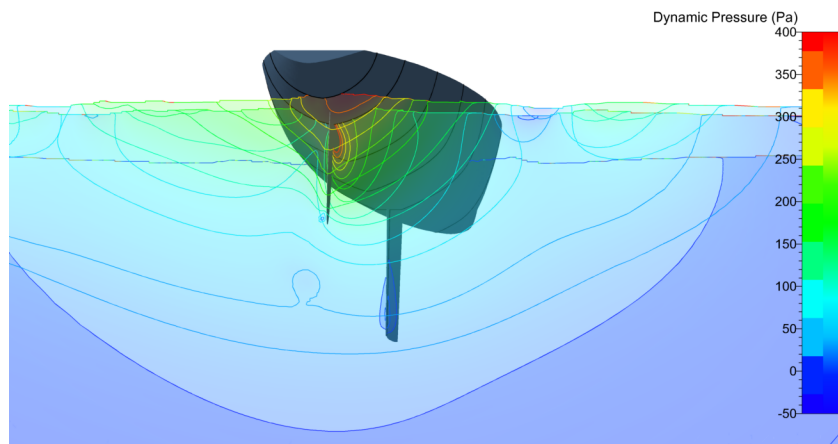


Figure G.20: The dynamic pressure plotted on multiple yz -planes, for the test case with $\beta = 3^\circ$ and $\delta = 5^\circ$

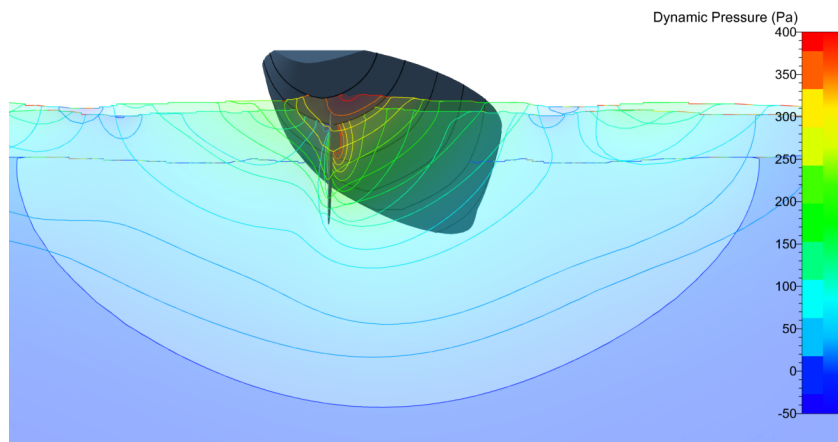


Figure G.21: The dynamic pressure plotted on multiple yz -planes, for the test case with $\beta = 0^\circ$ and $\delta = 7^\circ$ and without keel.